POLITECNICO
MILANO 1863

SCUOLA DI INGEGNERIA INDUSTRIALE
E DELL'INFORMAZIONE

Implementation and assessment of mode mixity and load ratio in the SSF algorithm to predict fatigue delamination of composites

TESI DI LAUREA MAGISTRALE IN
MECHANICAL ENGINEERING
INGEGNERIA MECCANICA

Author: **Elena Colombo**

Student ID: 10686430
Advisor: Luca Michele Martulli
Co-advisors: Sajjad Safaei, Leonardo Guido Salvi
Academic Year: 2023-24

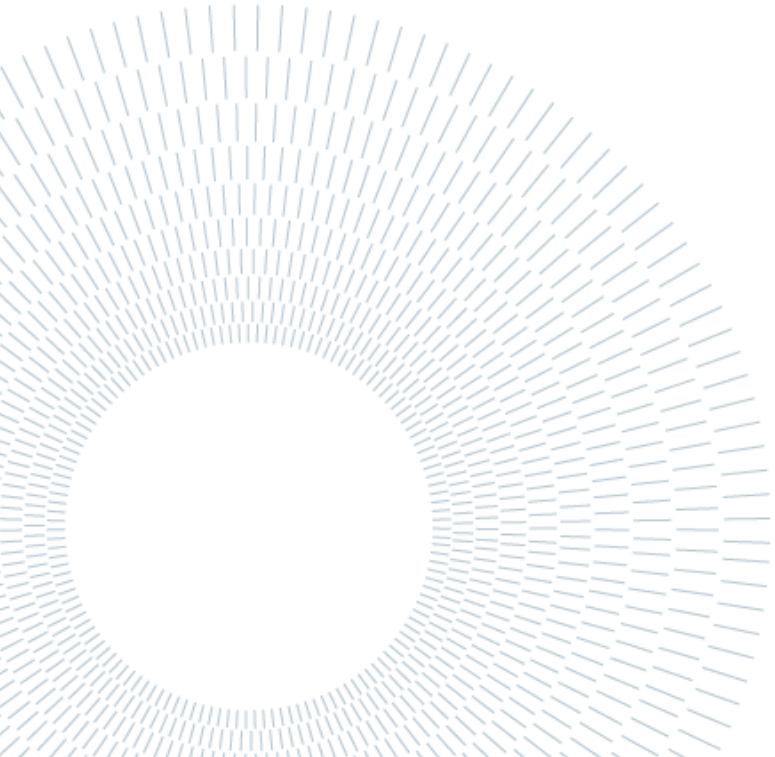

Abstract

The aim of the present work is the evaluation of the performance of the Sequential Static Fatigue (SSF) algorithm, developed by Martulli and Bernasconi [1], under different loading conditions. Therefore, two sets of simulations on Carbon Fiber Reinforced Polymer (CFRP) laminates have been carried out to study how mode mixity and load ratio affect the accuracy of the simulations.

It was observed that the dependence of the performance on the loading conditions is strictly related to the presence of numerical errors in the evaluation of the Strain Energy Release Rate (SERR). In particular, being mode I simulations highly affected by those errors, they were less accurate than the mode II ones. Besides, since the propagation rate at high load ratios is more sensitive to small variations in the SERR, the results of the simulations worsened by increasing this parameter.

Key-words: delamination; composites; fatigue; finite elements analysis.

Abstract in italiano

Lo scopo del presente lavoro è la valutazione delle prestazioni dell'algoritmo Sequential Static Fatigue (SSF), sviluppato da Martulli e Bernasconi [1], sotto diverse condizioni di carico. Pertanto, sono state eseguite due serie di simulazioni su laminati rinforzati con fibre di carbonio per studiare come i diversi modi carico e il rapporto di carico influenzano l'accuratezza delle simulazioni.

È stato osservato che la dipendenza delle prestazioni dalle condizioni di carico è strettamente legata alla presenza di errori numerici nella valutazione del tasso di rilascio dell'energia di deformazione (SERR). In particolare, essendo le simulazioni eseguite sotto sforzi di trazione (modo I) fortemente influenzate da tali errori, esse sono risultate meno accurate rispetto a quelle caratterizzate da sforzi di taglio (modo II). Inoltre, poiché la velocità di propagazione a rapporti di carico elevati è più sensibile a piccole variazioni di SERR, i risultati delle simulazioni sono peggiorati all'aumentare di questo parametro.

Parole chiave: delaminazione; materiali compositi; fatica; analisi agli elementi finiti.

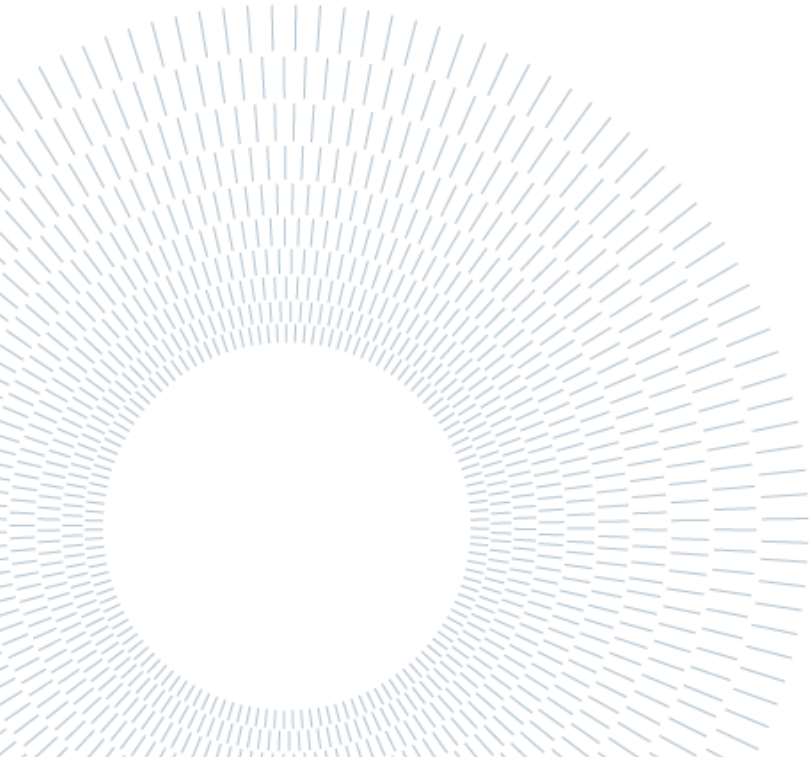

Contents

Introduction

Composite materials are usually employed in aeronautical and space applications because they guarantee high strength and stiffness while allowing for a lightweight design compared to metals.

These materials can be divided into three main categories: particle reinforced, fiber reinforced and structured composites (Fig. 1).

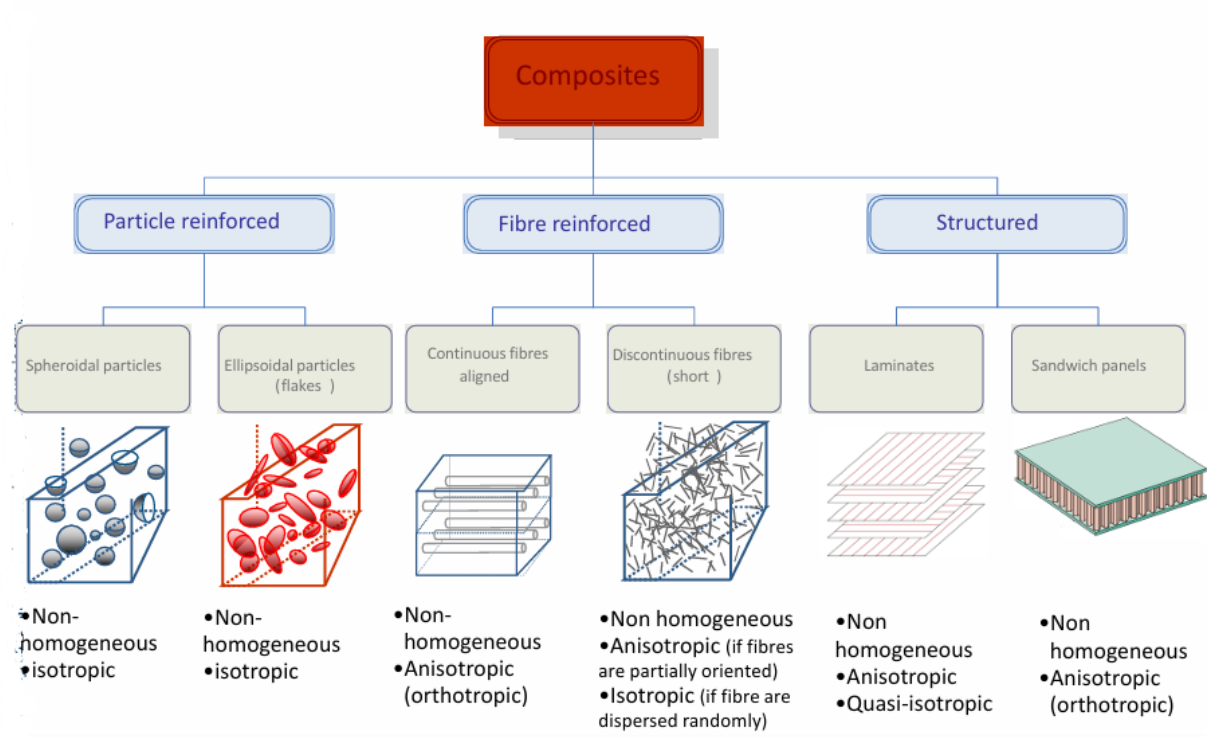

Fig. 1: Classification of composite materials [2].

In particular, the ones of interest for this work are the structured laminates, that consist in the stacking of multiple laminae, also called plies.

The main load-carrying elements of the laminae are continuous aligned fibers that are protected and kept in position by the matrix. The fibers are often made of carbon or glass, while for the matrix it is common to use epoxies, thermoset polymers employed above all in aerospace and aircraft applications [2].

Laminae exhibit a specific tensile strength along the fiber direction that is superior to the one of metals, but they are weaker in compression and in the transverse direction. For this reason, to create light but stiff materials, the laminae are usually piled into laminates by optimizing the stacking sequence in terms of fiber orientation and relative thickness of the plies [2].

The main processes that can be used to bond the laminae are hand lay-up (Fig. 2), Resin Transfer Molding (RTM), Vacuum Assisted RTM (VARTM), prepreg and autoclave processing, pultrusion and filament winding.

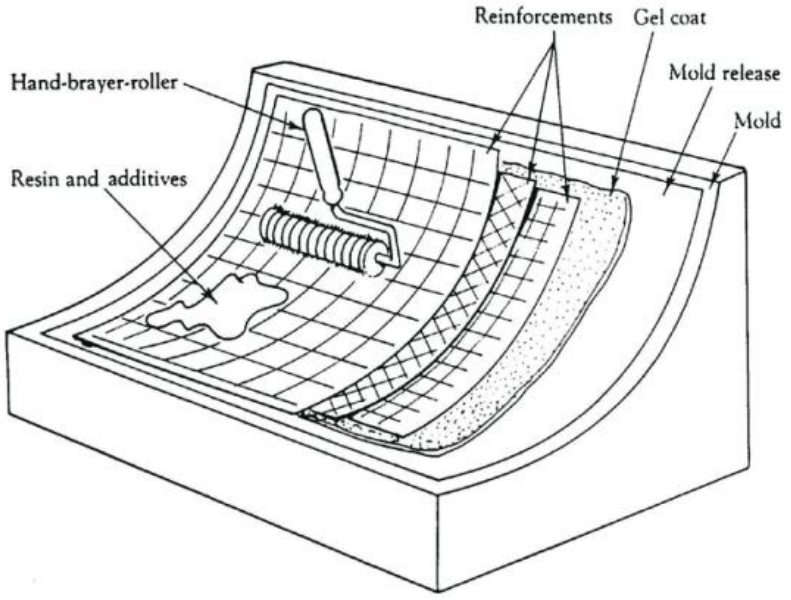

Fig. 2: Hand lay-up process to create a laminate [2].

Laminated structures can fail because of matrix cracking, fiber fracture, matrix-fiber debonding, but one of the most common failure modes is the delamination of adjacent plies [3]. As a result, to make them reliable according to the damage tolerant design approach, it is necessary to identify propagation laws able to predict the growth of delamination when subject to specific load spectra. For this reason, researchers have conducted both quasi-static and fatigue tests under different loading conditions. However, along with experimental tests, it can be advantageous to also perform numerical simulations. In particular, the integration of these two methods would result in the possibility to predict the life of laminated structures in a faster and more cost-effective way with respect to performing only tests on real specimens.

With this in mind, the present work aims to prove the capabilities of the SSF algorithm in predicting the delamination of composite laminates. In particular, the effects on the performance of mode mixity and load ratio will be analyzed in depth.

1 State of the art

In this chapter, at first an introduction to the delamination of composite laminates is provided. Along with it, the concepts at the basis of the Linear Elastic Fracture Mechanics (LEFM) theory are explained in order to have a better understanding of the propagation laws that describe the delamination phenomenon. Then, the two principal numerical methods employed in the simulation of fatigue crack propagation are presented since one of them is at the basis of the SSF algorithm. Finally, a description of the SSF algorithm is given in the last section.

1.1. Fatigue delamination of composite laminates

Delamination is the principal failure mode of composite laminates. It consists in the separation of the layers along their interface and in the consequent reduction in the strength and stiffness of the structure, making it unsafe. One of the most critical aspects of this phenomenon is the difficulty in detecting it visually; in fact, even if the structure seems to be intact, a critical damage may lie between the plies so that catastrophic failure can occur unexpectedly [4].

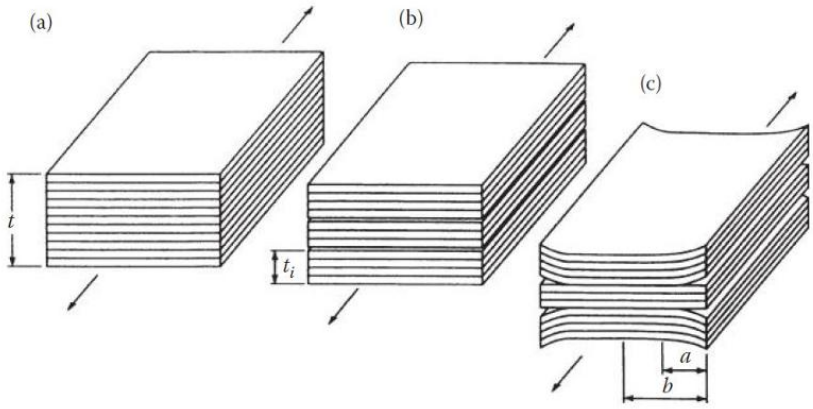

Fig. 3:(a) Laminated; (b) Totally delaminated; (c) Partially delaminated composite laminate [1].

Delamination is induced by interlaminar tensile and shear stresses that can arise in correspondence of discontinuities, such as free edges, ply drop, bond joints and

manufacturing defects. Besides, also impacts can initiate a local detachment between adjacent plies.

1.1.1. Introduction to LEFM

To describe the delamination growth of composites, it is common practice to model delamination using the LEFM approach, the origins of which date back to the 1920s of the last century, when A. Griffith, an English engineer, proposed an energy balance approach to estimate the strength of a cracked brittle material.

According to Griffith, a crack in a brittle material grows if the stress at its tip is sufficient to break the bonds in that location and if the reduction in strain energy due to the crack propagation is equal or greater than the increase in surface energy required by the new crack faces [5]. In particular, the second condition for crack growth can be expressed as:

$$-\frac{dU_s}{da} \geq \frac{dU_\gamma}{da} \qquad \text{Eq. 1}$$

where dU_s and dU_γ are the infinitesimal variations of strain energy and surface energy per unit width, respectively, and da is the infinitesimal crack length increment. The rate of reduction of the strain energy per unit increment of crack surface area is called Strain Energy Release Rate (SERR) and it is indicated with the letter G:

$$G = -\frac{dU_s}{da}$$

On the other hand, the rate of variation of the surface energy per unit increment of crack surface area is a material property [5]. This quantity is the fracture toughness of the material and, since above its value the crack propagates in an unstable way, it also known as critical SERR (G_c).

The propagation can be unstable or stable depending on the loading conditions. In case of constant applied load, the crack grows in an unstable way only once the fracture toughness, or, equivalently, the critical crack length for that load, is reached (Fig. 4a). If it is the displacement to be controlled, the propagation will be stable because, once the equilibrium point is reached, a further increment of crack length would release less strain energy than the one required by the crack surface to grow (Fig. 4b).

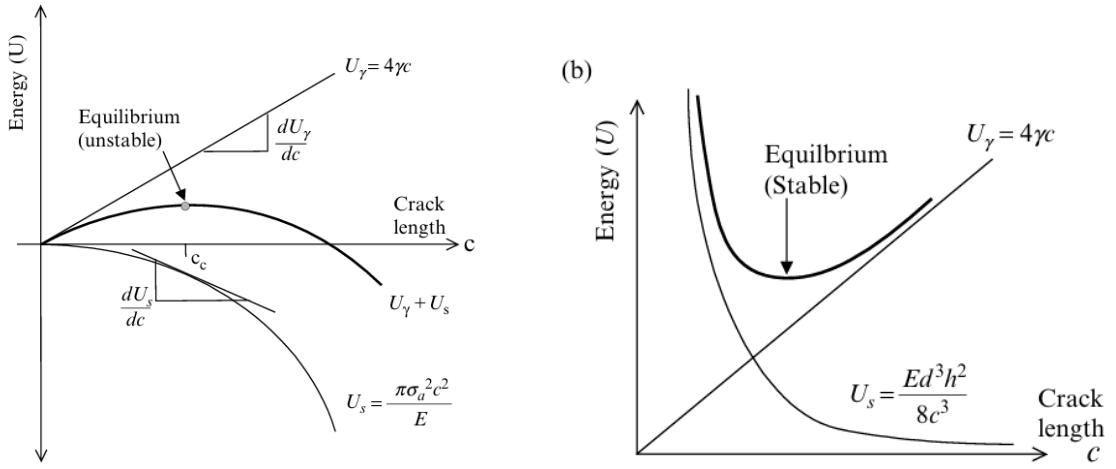

(a) Unstable equilibrium (b) Stable equilibrium

Fig. 4. (a) Unstable propagation in case of constant applied load; (b) Stable propagation in case of controlled displacement conditions [5].

In the '50s, G. R. Irwin, an American scientist, introduced two important novelties for the development of LEFM: the extension of the Griffith approach also to ductile materials and the concept of Stress Intensity Factor (SIF), indicated with the letter K.

To apply the LEFM principles to ductile materials, a term related to the dissipation of strain energy due to the creation of a plastic zone at the crack tip was added to the one related to the formation of new surfaces. In fact, by considering only the surface energy as a resistance term for crack growth, it would significantly underestimate the fracture toughness of ductile materials, while the error in the evaluation of critical SERR of brittle materials would be negligible because they aren't prone to deforming plastically.

Concerning the SIF, it is a parameter that quantifies the magnitude of the stress, σ_x, in the proximity of a crack (Fig. 5).

$$K_I = \sigma Y \sqrt{\pi a} \qquad \text{Eq. 2}$$

$$\sigma_x = \frac{K_I}{\sqrt{2\pi r}} f(\theta) \qquad \text{Eq. 3}$$

In Eq. 2, σ is the remote applied stress, Y is a geometry factor and a is the crack length; the subscript I is referred to the mode I loading condition, as will be explained in section 1.1.2. In Eq. 3, r and θ represent the polar coordinates of the point in which the local stress σ_x is evaluated and f is a function of θ. It can be noted that the local stress depends uniquely on the SIF and, therefore, on the remote applied stress and on the crack length [5], [6].

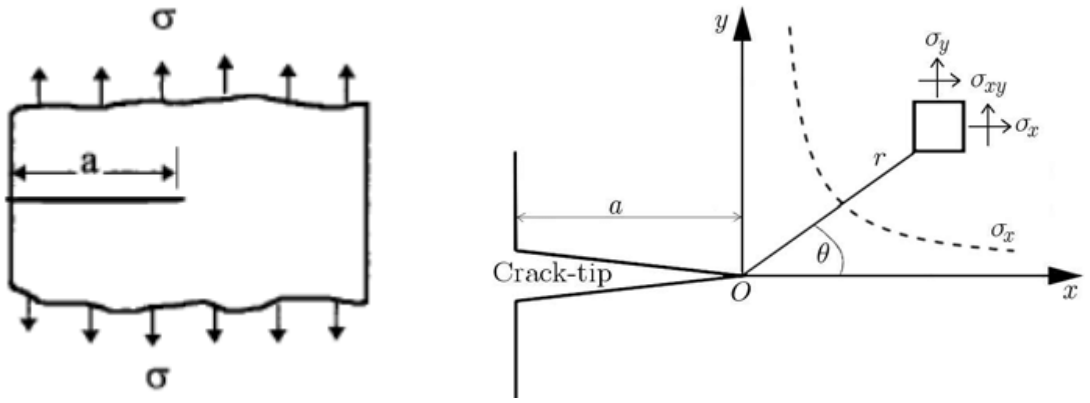

(a) Edge crack (b) Stress components

Fig. 5: (a) Edge crack in a semi-infinite body [7]; (b) Crack tip stress components [8].

A simple relationship exists between the SERR and the SIF [6]:

for plane stress $K = \sqrt{EG}$ (a)

for plane strain $K = \sqrt{\frac{EG}{(1-\upsilon^2)}}$ (b) Eq. 4

where E is the elastic modulus and υ is the Poisson ratio of the material.

1.1.2. Loading modes

A crack can be subject to different loading modes (Fig. 6), that are:

- Mode I, or opening mode.
- Mode II, or sliding mode.
- Mode III, or tearing mode.

Each mode has its own expressions for the evaluation of the SIF and of the stress field in the vicinity of the crack tip; in particular, Eq. 2 and Eq. 3 refer to mode I loading. However, in real applications, it is very common that more loading modes coexist, so that a mixed mode loading condition is present.

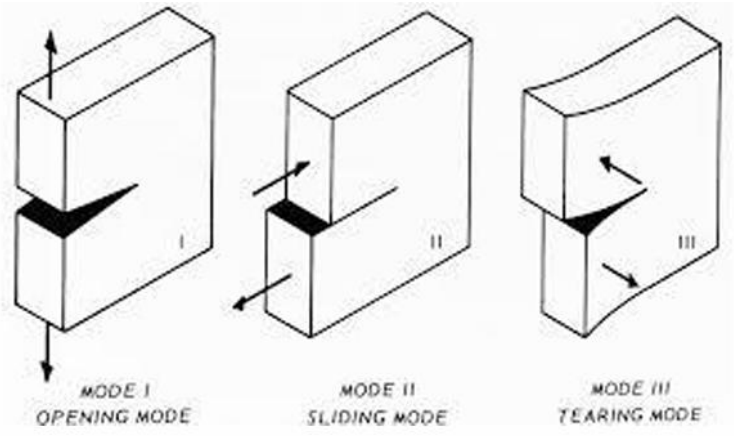

Fig. 6: Loading modes of a crack [2].

Since in case of anisotropic materials it is difficult to find an analytical expression for the function $f(\theta)$ of Eq. 3, the derivation of the SIF from the stress field is not very suitable for composite laminates. For this reason, the SERR is the preferred option to describe the delamination of these materials [2].

As for the SIF, different loading modes are characterized by specific formulations of the SERR, and, in case of mixed mode conditions, the total, or equivalent, SERR G_{eq} can be calculated as the sum of the SERRs of the single loading modes:

$$G_{eq} = G_I + G_{II} + G_{III} \qquad \text{Eq. 5}$$

where G_I, G_{II} and G_{III} are the mode I, II and III SERRs, respectively.

To quantify the contribution of each mode in case of mixed mode loading conditions, the mode mixity parameter, MM, is used. It is defined as [1]:

$$MM = \frac{G_{II} + G_{III}}{G_{eq}} \qquad \text{Eq. 6}$$

Depending on the performed experimental test, a specific mode can be prevalent on the other two. For example, to study mode I, the Double Cantilever Beam (DCB) test (Fig. 7a) can be employed, while for mode II the End Notched Flexural (ENF) test (Fig. 7b) is usually adopted. Besides, the Mixed Mode Bending (MMB) test (Fig. 7c), consisting in the superposition of modes I and II, is used to investigate the fatigue behavior of the material when both the modes are present. Consequently, the following assumptions can be made:

DCB test: $G_{eq} = G_I \quad (a)$

ENF test: $G_{eq} = G_{II} \quad (b)$ Eq. 7

MMB test: $G_{eq} = G_I + G_{II} \quad (c)$

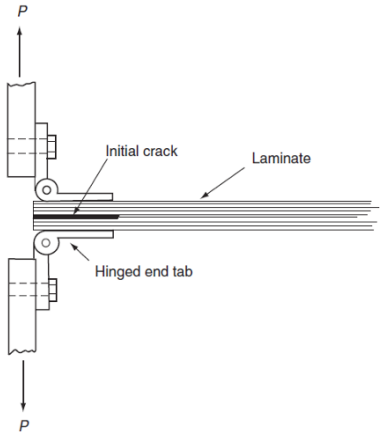

(a) DCB test [2]

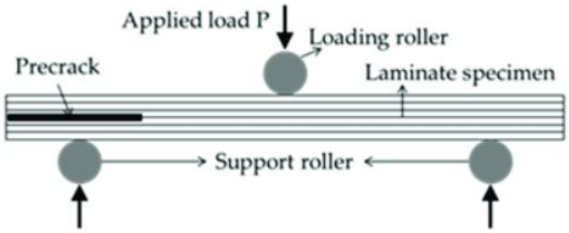

(b) ENF test [9]

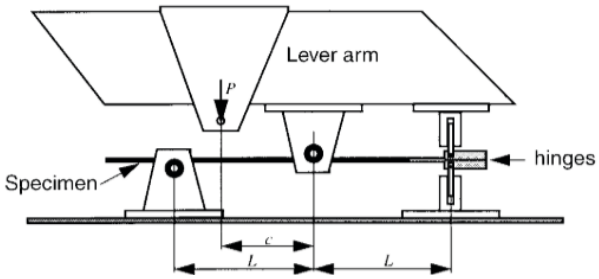

(c) MMB test [10]

Fig. 7: Mode I, mode II and mixed mode test setups.

1.1.3. Methods to evaluate the SERR

In the case studies of this work, different methods are used to extract the values of the SERR that arise in correspondence of the delamination front. In the following lines, the details of the most adopted ones are provided, while the others are only mentioned since they will be discussed more in depth in the context of their application in the Materials and methods chapter.

In order to evaluate analytically G_I and G_{II}, it is common practice to use the so-called compliance method. The resulting equation, based on geometrical linearities assumptions, holds for both modes I and II and can be written as:

$$G = \frac{P^2}{2b}\frac{\partial C}{\partial a} \qquad \text{Eq. 8}$$

where P is the applied load, b the specimen width, C the compliance and a the crack length [2], [11]. To better contextualize these quantities, it is possible to make reference to Fig. 7.

The compliance is defined as:

$$C = \frac{d}{P} \qquad \text{Eq. 9}$$

where d is the displacement in correspondence of the point of application of the load P.

In order to find the equation that relates the compliance to the crack length, it is possible to directly fit experimental data or to use analytical expressions.

As an example, the formulations adopted by Armanios et al. [10], that performed the DCB, ENF and MMB tests on which the first case study of the present work is based, are here presented.

The mode I compliance for the DCB test was calculated as:

$$C_I = \frac{8(a+\Delta)^3}{E_f b} \qquad \text{Eq. 10}$$

where Δ is a crack length correction that accounts for shear deformations and E_f is the flexural modulus of the material [11].

By combining Eq. 8, Eq. 9 and Eq. 10, G_I can be expressed by means of three equivalent equations:

$$G_I = \frac{3P_I d}{2b(a+\Delta)^2} \quad (a)$$

$$G_I = \frac{12P_I^2(a+\Delta)^2}{E_f b^2 h^3} \quad (b) \qquad \text{Eq. 11}$$

$$G_I = \frac{3E_f h^3 d^2}{16(a+\Delta)^4} \quad (c)$$

From the equations above, it can be observed that, in case of tests performed under a constant applied load, G_I increases as the crack propagates (Eq. 11b), while, in case of

constant applied displacement, G_I decreases (Eq. 11c) during propagation. Besides, as noted before, in load control conditions the propagation is unstable, while in displacement control it is stable.

Similar calculations and observations could be made also for G_{II} [11].

In the case of MMB test (Fig. 7c), the mode I and II load components, P_I and P_{II}, can be calculated, from equilibrium considerations, as:

$$P_I = \frac{1}{4}(3c - L)\frac{P}{L} \quad \text{Eq. 12}$$

$$P_{II} = (c + L)\frac{P}{L} \quad \text{Eq. 13}$$

where P is the applied load and c and L are lengths defined in Fig. 7c [10].

By substituting the formulation of P_I (Eq. 12) into Eq. 11b, it is possible to obtain G_I. To determine G_{eq} (Eq. 7c), the same should be done with the mode II component, by inserting the formulation of P_{II} (Eq. 13) into the corresponding SERR equation.

For all the tests performed, Armanios et al. [10] employed the SERR formulation that requires only the evaluation of the applied load, that, in case of the G_I, is Eq. 11b.

In order to study the behavior of a structure under mode I, mode II and mixed mode loading conditions it is also possible to apply two moments to the tips of the laminate arms, the intensity and the direction of which depend on the loading mode. Also in this case, analytical formulations have been developed to calculate the SERRs for each mode [1], [12]. On the other hand, Simon et al. [13] prefer to estimate the SERR of their experimental tests relying on the combination of experimental data and numerical simulations. More details about these two techniques will be provided in sections 2.2.1 and 2.3.1, respectively.

1.1.4. Fatigue crack growth

The SIF and the SERR are very useful parameters to describe also the propagation of a pre-existing crack in case of cyclic applied load or displacement.

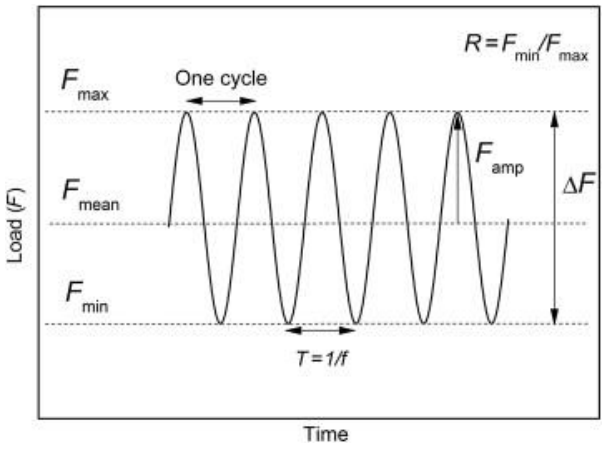

Fig. 8 Constant amplitude fatigue loading cycles.

In a fatigue loading cycle, the following quantities can be defined:

P_{min} and P_{max} $(d_{min}$ and $d_{max})$	Minimum and maximum loads (displacements)
$P_{mean} = \frac{P_{min}+P_{max}}{2}$ (d_{mean})	Mean load (displacement)
$P_{amp} = \frac{P_{max}-P_{min}}{2}$ (d_{amp})	Amplitude load (displacement)
$\Delta P = P_{max} - P_{min}$ (Δd)	Load (displacement) range
$R = \frac{P_{min}}{P_{max}}$ (R_d)	Load (displacement) ratio

From Eq. 8 it can be observed that, under the assumptions of LEFM, the SERR is proportional to the square of the load. Consequently, the maximum and minimum SERRs in a loading cycle, G_{max} and G_{min}, are, respectively, in correspondence of the maximum and minimum applied load and the following relationships can be derived:

$$\frac{G_{min}}{G_{max}} = R^2 \qquad \text{Eq. 14}$$

$$\Delta G = G_{max} - G_{min} = G_{max}(1 - R^2) \propto P_{mean}\Delta P \qquad \text{Eq. 15}$$

$$\Delta G_{eff} = \left(\Delta\sqrt{G}\right)^2 = \left(\sqrt{G_{max}} - \sqrt{G_{min}}\right)^2 = G_{max}(1 - R)^2 \propto \Delta P \qquad \text{Eq. 16}$$

where ΔG and ΔG_{eff} are, respectively the SERR range and the effective SERR range. The importance of these two parameters will be contextualized in section 1.2.

Moreover, being the SIF proportional to the square root of the SERR (Eq. 4), it varies linearly with the load, and so it is possible to write:

$$\frac{K_{min}}{K_{max}} = R \qquad \text{Eq. 17}$$

$$\Delta K = K_{max} - K_{min} \propto \Delta P \qquad \text{Eq. 18}$$

where K_{max} and K_{min} are, respectively, the maximum and minimum SIF in a loading cycle, while ΔK is the SIF range.

During fatigue loading, propagation can occur also at values of SIF or SERR lower than the critical ones. In the '60s, Paris and Erdogan noted that the propagation rate of a crack, da/dN, could be related to ΔK by means of an exponential law. The resulting equation, that took the name of the two researchers, can be expressed as follows:

$$\frac{da}{dN} = D(\Delta K)^m \qquad \text{Eq. 19}$$

where a is the crack length, N the number of cycles and D and m are empirical parameters obtained by fitting the experimental data.

If the propagation rate curve in Fig. 9 is observed, three regions can be identified. From left to right they are:

- Threshold region.
- Stable propagation region.
- Unstable propagation region.

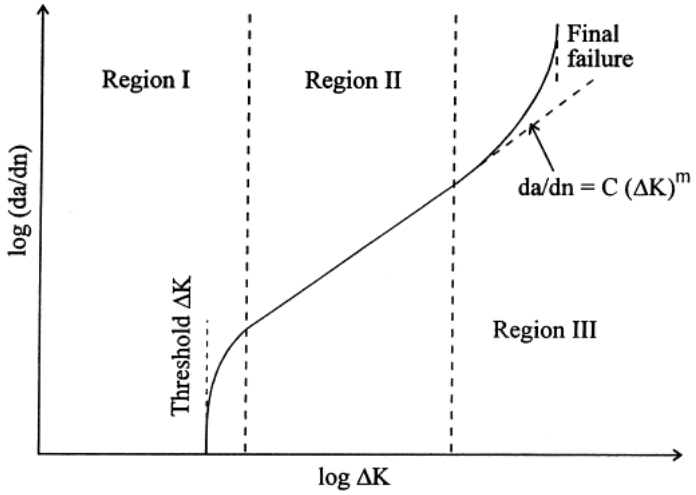

Fig. 9: Crack propagation rate as a function of the SIF range [14].

The Paris law is able to describe only the central region of the curve that, being in the log-log plane, consists of a straight line; here the crack propagation is stable.

The data in the first region are asymptotic to the so-called threshold SIF range, below which propagation doesn't occur, while the ones in the right part of the graph, asymptotic to the critical SIF range, represent an unstable crack propagation that leads to failure. To be noted that, in case of zero to tension loading (zero load ratio), the critical SIF range is equal to the critical SIF, that is a material constant; but, if the load ratio is different from zero, then the threshold SIF range changes with it [15].

As mentioned some paragraphs above, the evaluation of the SIF in case of laminates is complex due to their intrinsic anisotropy and, consequently, a modification to the traditional Paris law, at first introduced for metals, is necessary. Therefore, to describe the delamination of composites, different functions of the SERR can be used as substitutes of the SIF range [16]. This is the topic of the next section (1.2).

1.2. Correlating parameters and models

To describe the delamination of composites, propagation curves based on modified versions of the Paris law for metals are commonly adopted. In 1.2.1 the behavior of the curves obtained by using different correlating parameters is analyzed with a focus on the load ratio effect, while in 1.2.2 two models that attempt to reduce the sensibility of the propagation curves on the load ratio are presented.

1.2.1. Correlating Parameters

The term correlating parameter refers to the variable used in a Paris-like equation to evaluate the crack growth rate. This concept is strictly related to the one of Crack Driving Force (CDF), definition that can be applied to those correlating parameters able to control crack growth and that, as a consequence, can be used to describe this phenomenon. Nowadays, a lot of effort is put into finding CDFs that would allow us to plot a delamination growth rate curve that is not sensitive to the load ratio effect and to little variations in the loads [13], [17].

One of the traditionally adopted correlating parameters is G_{max}, the maximum SERR in a fatigue cycle. The corresponding Paris equation can be written as:

$$\frac{da}{dN} = D(G_{max})^m \qquad \text{Eq. 20}$$

Matsuda et al. [18] used G_{max} to plot the delamination growth rate curve of two CFRP materials with different matrix toughness tested under mode II fatigue loading at two positive load ratios. For both the materials examined, as the load ratio increases, the slope of the curve and the threshold maximum SERR $G_{max}^{(th)}$ increase, while the delamination growth rate, in correspondence of the same maximum SERR value, decreases.

Matsubara et al. [19] performed experiments on two types of Glass Fiber Reinforced Polymers (GFRP) laminates, a UD one and a laminate made of alternating UD and satin-woven fabric plies (Fig. 10). The tests were conducted in mode II fatigue loading at both positive and negative load ratios. For both the laminates, the considerations regarding the effects of the load ratio on slope, propagation rate and threshold maximum SERR are the same as the ones of the previous authors [18]. Besides, they noted that the critical maximum SERR G_c is not affected by the load ratio.

Simon et al. [13] adopted the maximum SERR normalized with respect to the fracture toughness to plot the results that they extracted from mode I tests on CFRP laminates. The corresponding propagation law is:

$$\frac{da}{dN} = D\left(\frac{G_{max}}{G_c}\right)^m = D(\hat{G}_{max})^m \qquad \text{Eq. 21}$$

They noted that the effect of the load ratio on the delamination rate curves is the same as the one obtained by the previous authors [18], [19] for mode II loading conditions.

Finally, Androuin et al. [17] used the same correlating parameter of [13]. They performed tests on CFRP laminates cyclically loaded at both mode I and II to study the load ratio effect. As expected, the trend is similar to the ones discussed before, but it is worth highlighting two differences: in this case, the slopes of the curves seem to be not significantly affected by the load ratio and the mode I curves for the highest tested load ratios converge into a single curve, suggesting that the load ratio effect is driven by a phenomenon that tends to disappear when this parameter exceeds a certain value.

To summarize the role of G_{max}, or of its normalized version $\hat{G}_{max}$, as a correlating parameter to describe the fatigue delamination growth rate, the following considerations can be made:

- It is not able to take into account the effect of the mean load (load ratio) on the propagation rate because of its intrinsic definition. As a result, the slope of the propagation rate curve and the threshold maximum SERR $G_{max}^{(th)}$ change depending on the load ratio, so that multiple curves are obtained. In particular, in most studies, both the slope and $G_{max}^{(th)}$ increase with the load ratio.
- The effect of the load ratio on the propagation curves is qualitatively the same for both mode I and mode II and also for both CFRPs and GFRPs.
- The critical maximum SERR G_c, that can be referred to as the fracture toughness, seems to be independent from the load ratio. Consequently, G_{max} can be considered as a good CDF for high propagation rates.

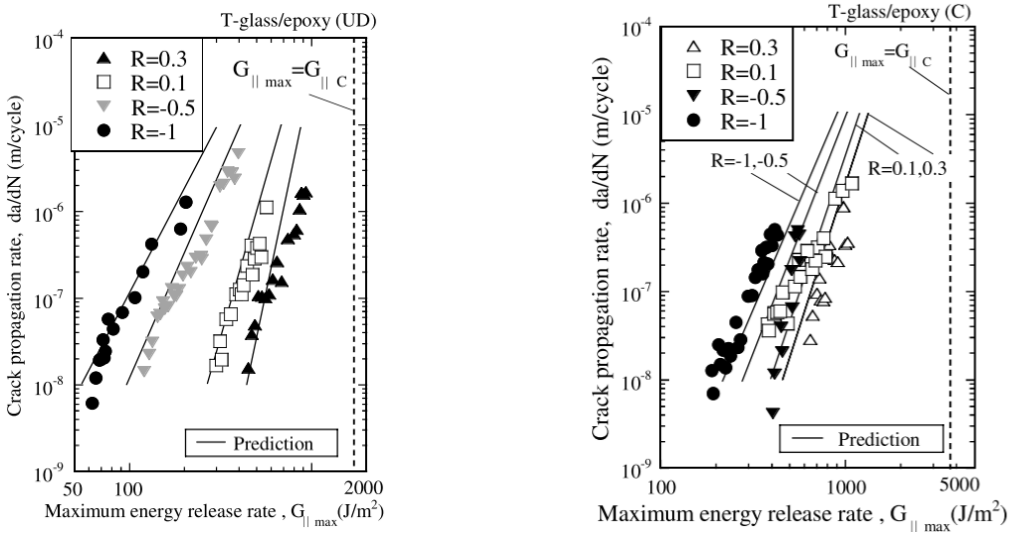

(a) UD laminate (b) UD/satin-woven laminate

Fig. 10: $da/dN - G_{max}$ curves for mode II fatigue delamination of GFRP laminates at different load ratios [19].

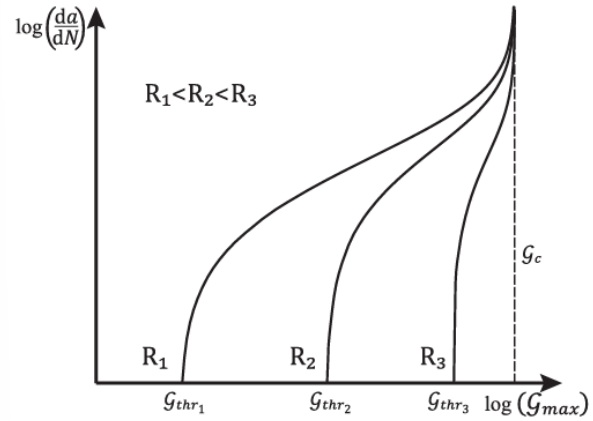

Fig. 11. Schematic representation of the load ratio effect on the delamination growth rate curves when G_{max} is used as fatigue correlating parameter [13].

Another commonly adopted correlating parameter is the SERR range ΔG, the definition of which is reported in Eq. 14. The corresponding Paris equation can be written as:

$$\frac{da}{dN} = D(\Delta G)^m \qquad \text{Eq. 22}$$

Bathias et al. [21] made use of this correlating parameter to study the delamination of GFRP laminates tested under mode I fatigue loading at different load ratios (Fig. 12a).

They observed that, when the load ratio increases, the propagation rate, for the same value of ΔG, increases, while the threshold SERR range $\Delta G^{(th)}$ decreases.

Khan et al. [22] tested CFRP laminates under mode I fatigue loading at different load ratios and at different initial delamination lengths in displacement control conditions (Fig. 12b). They noted that the experimental points plotted in the $\Delta G - da/dN$ plane are quite close to each other independently from the load ratio; however, a high degree of scatter is observed for the points referring to the same load ratio but obtained by different combinations of initial delamination lengths and opening displacements. This is explained by the authors as a direct consequence of the violation of the similitude principle, as explained in the papers published by Rans et al. [23], [24].

The effect of load ratio on mode II fatigue loading was investigated by Russel et al. [25], who tested CFRP laminates of different toughness at -1 and 0 load ratios. They observed that, for the tougher materials, a threshold SERR range $\Delta G^{(th)}$ is present, while for all of them the propagation rate is higher at $R = -1$ and the slope of the curve is higher at $R = 0$.

To summarize the role of ΔG as a fatigue correlating parameter to describe the delamination growth rate, the following considerations can be made:

- Not a unanimous consensus is reached in the effectiveness of the use of ΔG as correlating parameter. In some cases, it seems that the slope and the propagation rate increase with the load ratio and that a threshold SERR range $\Delta G^{(th)}$ can be identified independently from it. However, the publication of [25] suggests an opposite trend in terms of effect of the load ratio on the propagation rate and [22] noticed a large amount of scatter in the results, fact that has been explained as the consequence of the non-preservation of the similitude principle when adopting ΔG as a fracture mechanics correlating parameter.
- It has been used to analyze experimental results of mode I and II fatigue tests on both CFRPs and GFRPs.
- The presence of a threshold SERR range $\Delta G^{(th)}$ independent from the load ratio is highlighted in some studies [21], [25]; it suggests that ΔG is able to control the delamination in correspondence of low values of propagation rate and that, consequently, it can be considered a good CDF for these values of delamination rate.

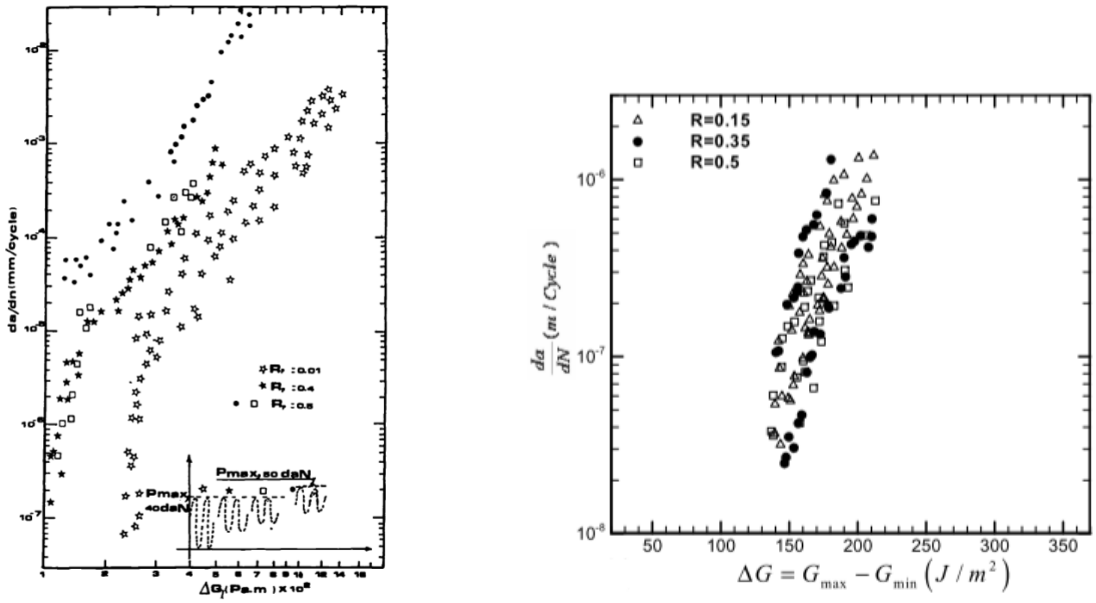

(a) mode I, GFRP laminate [21] (b) mode II, CFRP laminate [22]

Fig. 12. $da/dN - \Delta G$ curves for fatigue delamination of composite laminates at different load ratios.

As seen in the previous section, being ΔG not compliant with the similitude principle [22], some difficulties in the interpretation of the load ratio effect in the delamination phenomenon arise when that correlating parameter is employed. For this reason, an alternative definition of the SERR range has been introduced and it will be referred to as the effective SERR range, ΔG_{eff}, the definition of which is reported in Eq. 16. The corresponding Paris equation can be written as:

$$\frac{da}{dN} = D(\Delta G_{eff})^m \qquad \text{Eq. 23}$$

The modified SERR range has been adopted by Matsubara et al. [19] that, besides using G_{max} as described before, analyzed the results of their mode II fatigue tests also with this correlating parameter (Fig. 13). They found that, for both the GFRP UD and UD/satin-woven fabric laminates, the slope of the propagation rate curves increases with load ratio. Moreover, the threshold effective SERR range value is independent from it in the case of the UD laminate, while for the other type of laminate the threshold value for negative load ratios is about four times higher than the one for positive load ratios.

Results similar to the ones of the GFRP UD laminates [19] are obtained by Tanaka et al. [26] also for CFRPs, even if, in this latter case, the identified threshold effective SERR range $\Delta G_{eff}^{(th)}$ is about one third of the one of GFRPs.

Khan et al. [22] have performed a comparison between the traditional SERR range and its modified version when used as correlating parameters in the propagation law (Fig. 14). They noted that the results plotted by employing the effective SERR range have less scatter and that the specimens loaded at higher load ratios show a higher delamination rate for the same value of the correlating parameter. Besides, since this modified formulation of the SERR range is in accordance with the similitude principle, the experimental points collapse into a single line, for the same load ratio, even if the imposed opening displacement is different.

Donough et al. [16] performed experiments on CFRP laminates under mode I and II fatigue loading to explore the fiber bridging phenomenon and the load ratio effect on the delamination. They found that a significant load ratio effect is present for mode I, but not for mode II. In particular, the slope of the propagation curve and the propagation rate increase with the load ratio; besides, they noted that the slope of the curves of mode I are about twice the slope identified for mode II.

Finally, Simon et al. [13] have adopted as correlating parameter, in addition to $\hat{G}_{max}$, also ΔG_{eff} normalized with respect to G_c. Since the fracture toughness has been demonstrated to be load ratio independent, it is expected to find the same trends of the propagation curves as observed by the previous authors, and, actually, this is the case. Besides, a threshold effective SERR range $\Delta G_{eff}^{(th)}$ has been identified, and it seems to be independent from the load ratio.

To summarize the role of ΔG_{eff}, or of its normalized version, as a correlating parameter to describe the delamination rate, the following considerations can be made:

- It is a better alternative to the use of the classical SERR range ΔG because ΔG_{eff} is compliant with the similitude principle [22].
- Since the similitude principle is respected, the effect of the load ratio on the propagation is clearer [22]; in particular, for mode I, the higher is the load ratio, the higher are the slopes of the propagation curves and the propagation rates for the same value of ΔG_{eff}, while a threshold effective SERR range $\Delta G_{eff}^{(th)}$, independent from the load ratio, is usually identified. In case of mode II, it seems that the load ratio has a less significant effect on the delamination rate [16].
- The slopes of the mode I propagation curves are about twice the ones for mode II [16].
- Ss observed forΔG, this modified formulation has proven to be an effectiveCDF able to control propagation at rates close to the threshold point.

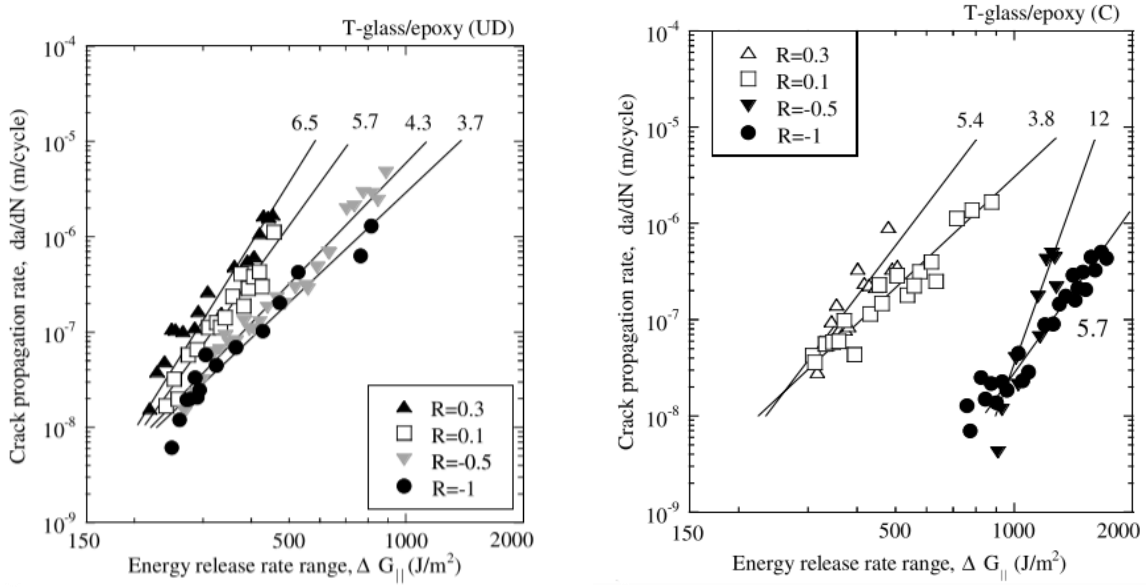

(a) UD laminate (b) UD/satin-woven laminate

Fig. 13: $da/dN - \Delta G_{eff}$ curves for mode II fatigue delamination of T-glass/#3651-epoxy laminates at different load ratios [19].

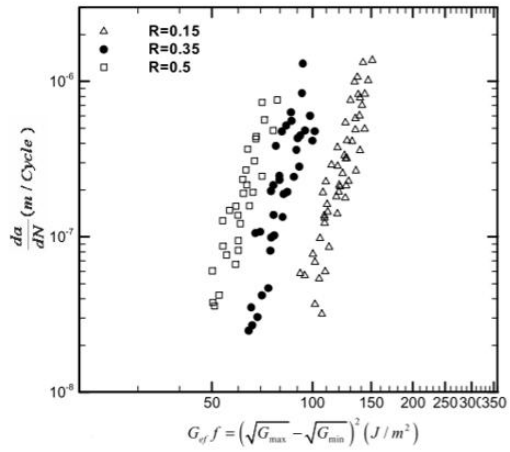

Fig. 14: $da/dN - \Delta G_{eff}$ curves for mode II fatigue delamination of M30SC/DT120 CFRP laminates at different load ratios [22].

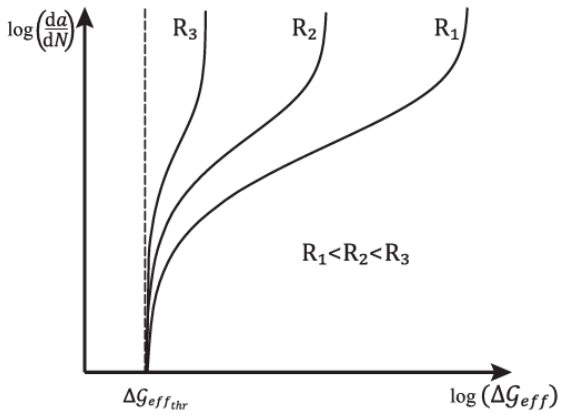

Fig. 15. Schematic representation of the load ratio effect on the delamination growth rate curves when the ΔG_{eff} is used as fatigue correlating parameter [13].

1.2.2. Models

In order to take into account the load ratio effect on the propagation curves, different models have been developed. Some of them just try to predict the position of the

delamination curves by identifying a dependence on the load ratio [20], [27], while others aim at generating a master propagation curve that is valid for all the load ratios [13], [17], [28], [29], [30], [31].

Allegri et al. [20] performed mode II fatigue tests on three CFRP laminates at different load ratios. They, by plotting the results as a function of the normalized maximum SERR $\hat{G}_{max}$, found a relationship between the slope of the curves and load ratio, so that the exponent m of Eq. 21 was expressed as:

$$m = \frac{b}{(1-R)^2} \qquad \text{Eq. 24}$$

In Fig. 16 it is possible to observe how the curves of the model are in agreement with the experimental data for one of the tested materials. Besides, also a comparison with the curves predicted by using the Anderson model [27] is shown.

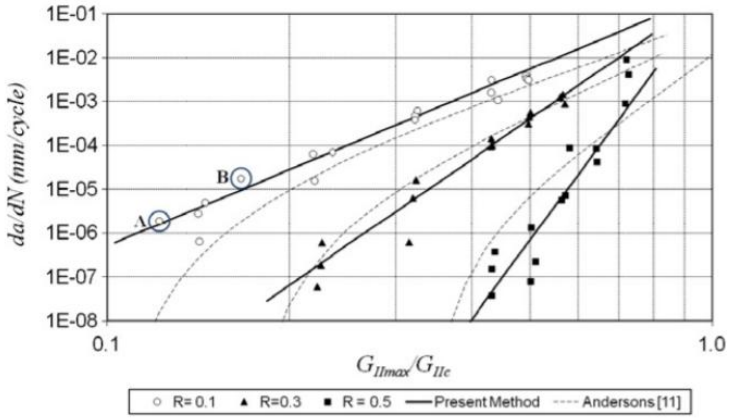

Fig. 16: $da/dN - \hat{G}_{max}$ curves for mode II fatigue delamination of IM7/8552 CFRP laminates at different load ratios [20].

Androuin et al. [17], as reported also in 1.2.1, have performed mode I and II experiments on CFRP laminates. They noted that, for both the modes, the propagation curves plotted as functions of $\hat{G}_{max}$ for different load ratios are significantly shifted but nearly parallel. Consequently, they concluded that the exponents m of the Paris laws are similar but the coefficients D vary with the load ratio (Fig. 17a). Therefore, a new method to generate master curve independent from the load ratio was proposed. It is based on the introduction of a new correlating parameter, ΔG_{eq}:

$$\Delta G_{eq} = G_{max}(1-R)^{2(1-\gamma)} \qquad \text{Eq. 25}$$

where γ is a shifiting parameter.

In order to find the value of γ, the first step consists in equalizing the slopes so that, for each mode, the curves corresponding to different correlating parameters have the same exponent m (Fig. 17b). Then, by the least square method applied to the

coefficients D of the new curves, it is possible to determine the proper shifting parameter and plot the propagation master curve (Fig. 17c), described by Eq. 26:

$$\frac{da}{dN} = D\left(\frac{\Delta G_{eq}}{G_c}\right)^m \qquad \text{Eq. 26}$$

where ΔG_{eq} is defined in Eq. 25.

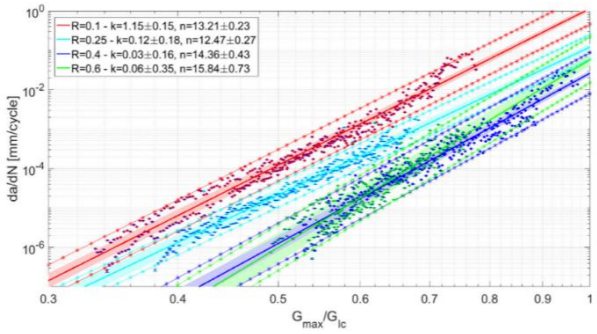

(a) Initial propagation curves

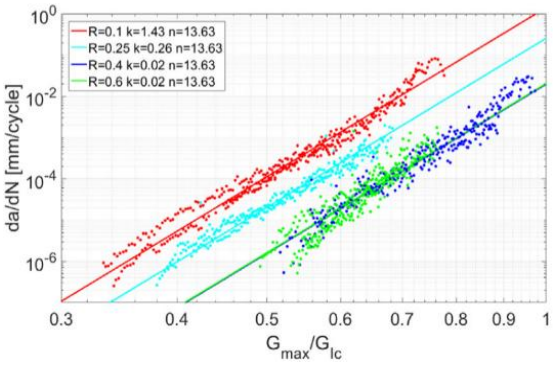

(b) Equalized-slope propagation curves

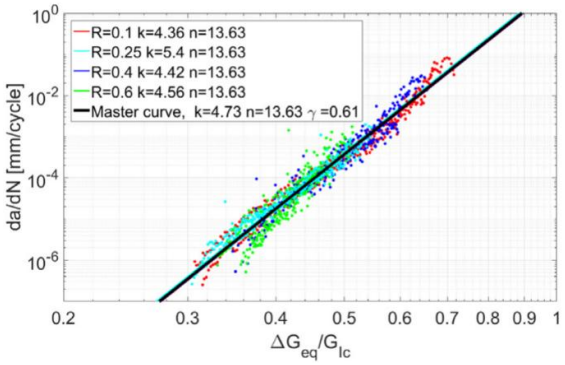

(c) Master propagation curve

Fig. 17. Identification of the mode I master propagation curve [17].

Further experiments performed by the same authors [17] have shown that the load history has a significant effect on the delamination rate. Therefore, the master curve cannot be used to simulate crack propagation for variable amplitude loading.

The following considerations will summarize the possible applications and limitations of the model presented by Androuin et al. [17]:

- It allows to generate master curves independent from the load ratio for both mode I and II, so that it can be considered as a good tool to predict delamination growth in composites.
- To create the master curve, the initial propagation curves corresponding to different load ratios need to be nearly parallel.
- The master curve can't be used to predict delamination in case of variable amplitude loading.

Another commonly adopted model is the one based on the Hartman-Schijve equation, introduced by the homonymous authors in the '70s to study the fatigue crack growth in aluminum alloys [32]. Not only this model allows to create a master propagation curve able to describe the delamination growth of composites independently from the load ratio, as the one of [17], but also to lower its slope. In this way, small uncertainties in the correlating parameter don't affect in a significant way the prediction of the delamination rate.

Different formulations, although similar, have been proposed. In the following, the most relevant ones are presented.

The propagation law suggested by [28], [29], [30] is:

$$\frac{da}{dN} = D\left(\frac{\Delta\sqrt{G} - \Delta\sqrt{G}^{(th)}}{\sqrt{1-\sqrt{\frac{G_{max}}{G_c}}}}\right)^m \qquad \text{Eq. 27}$$

where $\Delta\sqrt{G}$ is the square root of the effective SERR range ΔG_{eff}, defined in Eq. 16 and $\Delta\sqrt{G}^{(th)}$ is .its threshold value.

A representation of the propagation master curve generated by [28] is given in Fig. 18a.

The propagation law adopted by [31] is:

$$\frac{da}{dN} = D\left(\frac{\sqrt{G_{max}} - \sqrt{G_{max}^{(th)}}}{\sqrt{1-\sqrt{\frac{G_{max}}{G_c}}}}\right)^m \qquad \text{Eq. 28}$$

where $G_{max}^{(th)}$ is the threshold maximum SERR G_{max}.

Finally, the propagation law introduced by [13] is:

$$\frac{da}{dN} = D\left(\frac{\sqrt{\hat{G}_{max}} - \sqrt{\hat{G}_{\max}^{(th)}}}{\sqrt{1-\sqrt{\hat{G}_{max}}}}\right)^{m} \quad \text{Eq. 29}$$

where $\hat{G}_{\max}^{(th)}$ is the threshold of the normalized maximum SERR $\hat{G}_{max}$

A representation of the propagation master curve generated by [13] is given in Fig. 18b.

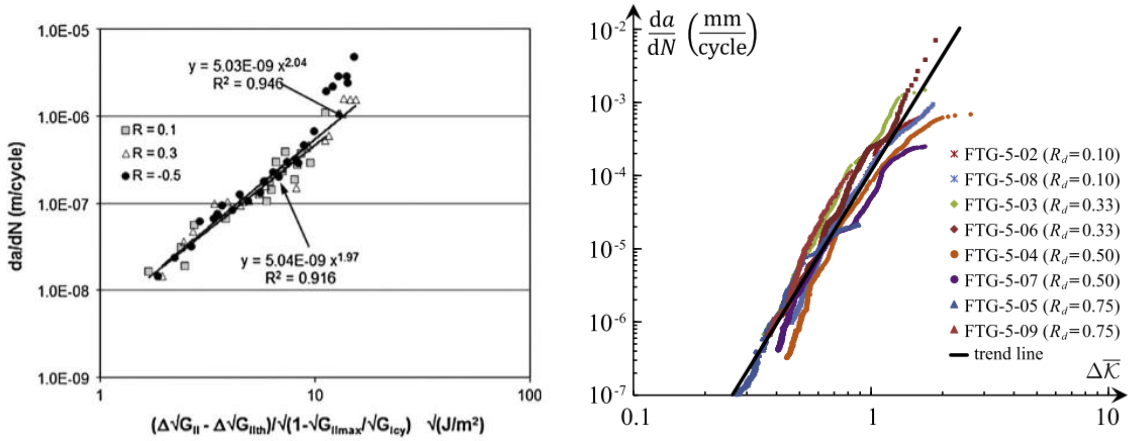

(a) Master propagation curve obtained by using Eq. 27 [28]

(b) Master propagation curve obtained by using Eq. 29 [13]

Fig. 18 Master propagation curves based on the modified Hartman-Schijve equation.

In order to apply the previous equations to predict the delamination growth rate, it is necessary to determine experimentally the values of G_c, $\Delta\sqrt{G}^{(th)}$ and $G_{max}^{(th)}$.

As discussed in the section dedicated to the use of G_{max} as correlating parameter (1.2.1), it can be assumed that the critical maximum SERR, G_c, is constant for all the load ratios and equal to the fracture toughness of the material. Even if [33], [34] have proven that quasi-static fracture toughness and the maximum SERR value for which the delamination propagates in a critical way descibe two different phenomena, the value of G_c is usually acquired from quasi-static tests.

On the contrary, the parameter $G_{max}^{(th)}$ depends strongly on the load ratio (Fig. 11). To overcome this issue, [13] have made use of the following relationship, derived from Eq. 16:

$$G_{max}^{(th)} = \frac{\Delta G_{eff}^{(th)}}{(1-R)^2} \quad \text{Eq. 30}$$

Alternatively, other authors [31] considered $G_{max}^{(th)}$ as a fitting parameter for each of the experimental data set so that all of them collapsed into a single curve with a slope ranging from 2 to 3.

Concerning the dependence of $\Delta\sqrt{G}^{(th)}$ on the load ratio, there is no aggrement among the researchers. In fact, as presented in the section regarding the use of the effective SERR range as fatigue correlating parameter (1.2.1), it seems that a unique threshold effective SERR range $\Delta G_{eff}^{(th)}$ can be defined independently from the load ratio [13], [19], [26]. However, [28], [29], [30] arrived at opposite conclusions.

It is possible to note that Eq. 27 requires the knowledge of the minimum SERR in a loading cycle, G_{min}. Since the evaluation of G_{min} is less accurate than the one of G_{max}, especially at low load ratios [29], the last two propagation laws (Eq. 28, Eq. 29) seem to be more advantageous [13].

The exponent of the master curves ranges between 2-3 [28], [29], [30], [31] and 5.2 [13] depending on the material, equation, methods and assumptions followed in the determination of the material constants and fitting parameters. However, all the analyzed master curves have a slope lower than the ones characterizing the propagation curves of composites when the traditional correlating parameters, namely G_{max}, ΔG and ΔG_{eff}, are used. For example, in the experimental campaign carried out by Simon et al. [13], the values of the exponents of the Paris-like equations range from 6.6 to 30.9 in case the propagation rate is expressed as a function of G_{max} or ΔG_{eff}. These steep slopes cause a high sensitivity of the delamination rate to small changes in the loads and, as a result, it makes the damage tolerance design approach impractical for this kind of materials. Moreover, since the correlating parameter in the model based on the Hartman-Shijve equation is proportional to the square root of the SERR, the comparison with the exponents of the other propagation laws can be performed by dividing by two the exponent of the model, so that the actual difference between the exponents is even higher. However, [13] demonstrated that the reduction of the slope reachable by adopting the Hartman-Shijve model has not a real effect on the reduction of the sensitivity issue, causing an apparent beneficial effect.

To summarize the possible applications and limitations of the model based on the Hartman-Shijve equation, the following considerations can be made:

- It allows us to create a master curve able to describe the propagation growth rate independently from the load ratio and with a lower slope than the previously considered laws.
- Several formulations are available, but the more advantageous are the ones that don't require the evaluation of the minimum SERR G_{min}.

- In all the formulations it is required to determine the fracture toughness G_c, that is independent form the load ratio, while the threshold values for propagation to be used and their dependence on the load ratio are debated issues.
- The reduction of the delamination rate curve slope has not a real beneficial effect on the reduction of the sensitivity of the predicted propagation rate to small changes in the load.

1.3. The load ratio effect

The load ratio has different effects on fatigue damage growth depending on the type of material and on the loading mode, but their origin is the same: non-linear mechanisms in the proximity of the crack. In fact, if the LEFM concepts hold, there should be no load ratio effect on the propagation curves since, as stated by the similitude principle, for a given material, same stress state at the crack tip implies same propagation rate [23], [24]. This is the reason why the maximum SIF K_{max} and the SIF range ΔK in case of metals and the maximum SERR G_{max} and the effective SERR range ΔG_{eff} in case of composites are considered good CDFs. Since K_{max} and G_{max} are proportional to the maximum applied load P_{max} (Eq. 4a, Eq. 11b) and that ΔK and ΔG_{eff} are proportional to the applied load range ΔP (Eq. 16b, Eq. 18c), the same value of correlating parameter should define in a univocal way the stress state at the crack tip. On the other hand, being the ΔG proportional to the product between the mean load P_{mean} and the load range ΔP (Eq. 15), a same value of this correlating parameter can be obtained by more than one combination of P_{max} and ΔP and so it doesn't guarantee the same state of stress. However, these observations are valid only under the assumptions of the LEFM because, actually, nonlinearities may arise during loading. For example, even if the load range is the same, different mean loads, and so different load ratios, can cause a different amount of nonlinear mechanisms.

In the next sections, the possible causes of the nonlinearities that are at the basis of the load ratio effect on the crack propagation curves are analyzed for both metals and composite laminates.

1.3.1. Load ratio effect in metals

In mode I fatigue loading of metals, crack closure seems to be the main responsible for the load ratio effect on the propagation rate curves. In fact, it modifies the minimum SIF K_{min} of the fatigue cycle, which becomes higher than the one calculated with the LEFM approach. This phenomenon is related to the plastic zone, the amount of which depends also on the load ratio, that can arise along the crack flanks when the structure is loaded. If the aforementioned plastic zone is present, during the unloading part of the fatigue cycle, the flanks tend to become closer until they enter in contact due to the presence of stretched material: the stress at which this happens is called opening stress. The more the load decreases, the more the plastically deformed zones are compressed,

causing the generation of reaction forces and the consequent development of a SIF. By applying the superposition principle, an increase of the effective minimum SIF is observed, and this effect is more evident as the minimum load of the fatigue cycle, and so the load ratio in case of constant maximum load, decreases. This is the reason that explains the anomalies observed in the fatigue crack growth rate plot when, for example, the SIF range ΔK is used as correlating parameter in the Paris equation: the crack growth rate curves related to different stress ratios don't overlap as expected from the similitude principle of LEFM, but they move upward as the load ratio increases. In fact, the more the load ratio decreases, the more the difference between the effective SIF range ΔK_{eff} and the classical one ΔK increases. Consequently, to obtain a unique propagation curve for all the stress ratios, the so-called master propagation curve, ΔK_{eff} should be used (Fig. 19) [15]. This quantity can be defined as:

$$\Delta K_{eff} = K_{max} - K_{close} \qquad \text{Eq. 31}$$

where K_{max} is the maximum SIF in a loading cycle and K_{close} is the SIF in correspondence of the closing stress; both the terms can be calculated by using the elastic formulation for the SIF (Eq. 2, Eq. 3), based on the LEFM assumptions.

Since it is difficult to evaluate the crack opening stress, in the '70s an empirical relationship useful to take into account the crack closure effect has been introduced by Elber [35] for the aluminum alloy 2024-T3:

$$\frac{\Delta K_{eff}}{\Delta K} = 0.5 + 0.4R \qquad \text{Eq. 32}$$

Some years later Schijve modified the Elber equation in the following way:

$$\frac{\Delta K_{eff}}{\Delta K} = 0.55 + 0.35R + 0.1R^2 \qquad \text{Eq. 33}$$

Even if the load ratio effect has been proved to be strongly material dependent, the above equations are often used also for other metal alloys [36].

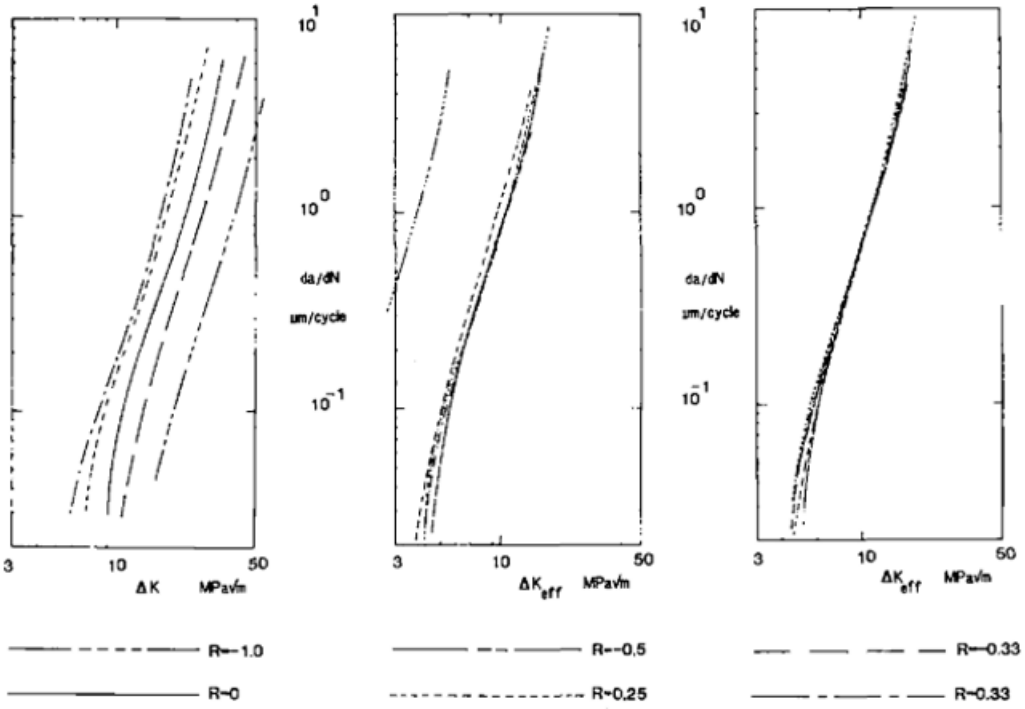

(a) Nominal SIF range (b) Effective SIF range according to Elber (c) Effective SIF range according to Schijve

Fig. 19: Crack propagation rate curves for the aluminum alloy 2024-T3 [15].

1.3.2. Load ratio effect in composites

Ideally, according to LEFM theory, there should be no load ratio effect on crack growth. In the case of metals, its effect has been related to the crack tip plasticity, that is a kind of nonlinear mechanism. As a result, also for composite materials the influence of the load ratio on the propagation rate has been associated with non-linearities in correspondence of the delamination front, such as crack closure due to asperities (roughness induced crack closure) and presence of broken fibers [22].

In order to investigate the load ratio effect on the delamination growth rate, Khan et al. [22] carried out mode I fatigue experiments on CFRP laminates under 0.15, 0.35 and 0.5 stress ratios values. To have a better understanding of such phenomenon, Scanning Electron Microscope (SEM) images of the fracture surfaces were analyzed: they highlighted that the surface roughness increases with the load ratio (Fig. 20). These examinations have found an explanation in the fact that at lower load ratios the surface has become smoother thanks to the repeated compressions at the low end of the fatigue cycle. This phenomenon is similar to the crack closure observed in metals and it explains the load ratio translational effect on the propagation curves.

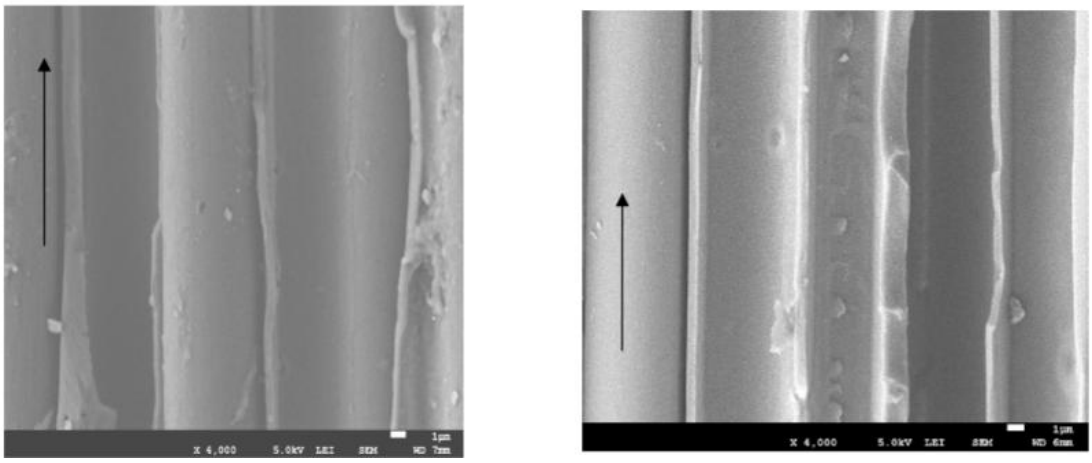

(a) $R = 0.15$ (b) $R = 0.5$

Fig. 20: SEM images of fracture surfaces at magnification 4K under different load ratios [22].

Some years later, the same authors [37] went deeper into the analysis of the stress ratio effect by considering also the contribution of fiber bridging (Fig. 21), phenomenon in which inclined fibers connect, like bridges, the detached interfaces and increase the resistance to further delamination growth. After having performed mode I fatigue tests on carbon/epoxy laminates, they noted that both crack closure and fiber bridging decrease the delamination growth rate. In particular, crack closure reduces the effective cyclic load amplitude by increasing the effective minimum load at the crack tip, inducing the same apparent load ratio effect of metals. As they have shown in the study published in 2009 [22], crack closure is typical of low load ratios, so that it can't provide an explanation for the load ratio effect observed also at load ratios higher than 0.3. On the other hand, it seems that fiber bridging and stress ratio effect are not correlated phenomena. Consequently, the researchers concluded that the effect of the load ratio on the delamination growth can't be fully explained by considering crack closure and fiber bridging alone.

Also Donough et al. [16] tried to explain the effect of the load ratio, but, in contrast to what has been concluded by Khan et al. [22], [37], they found that fiber bridging can be considered as the only mechanistic explanation to its effect on composite laminates. They have performed quasi-static and fatigue tests on CFRP laminates, under both mode I and II loading conditions. Concerning the quasi-static test, in case of mode I, they obtained a resistance curve that increases as the delamination front advances, as observed also by [13]. This behavior has been attributed by the authors to the bridging of cross-over fibers behind the crack tip. In case of mode II, no R-curve has been identified but, since the delamination crack growth is unstable when mode II ENF tests are performed, the results may be inaccurate [38]. By looking at the fatigue propagation curves, they noted a significant load ratio effect in mode I, but not in mode

II. Besides, when they applied a constant maximum SERR to the specimen, a decrease in the propagation rate was registered, since at the early stage of delamination the fiber bridging zone was not yet formed, while, as the crack grew, also the bridging of the fibers was able to fully develop and reduce the delamination rate, until a stabilized value was reached. In the researcher's opinion, fiber bridging causes an apparent load ratio effect because it induces traction forces at the crack tip (Fig. 21) that, in a way similar to the crack closure of metals, change the effective stress in that zone. However, while the tensile reaction forces related to the crack closure occur during the unloading phase of the fatigue cycle, the fiber bridging phenomenon has an influence during the opposite phase. Besides, by observing the morphology of the resin in the delaminated region, they noted traits typical of brittle fracture mechanisms, so that the presence of plastic deformation of the epoxy matrix and, consequently, of the crack closure effect, was excluded.

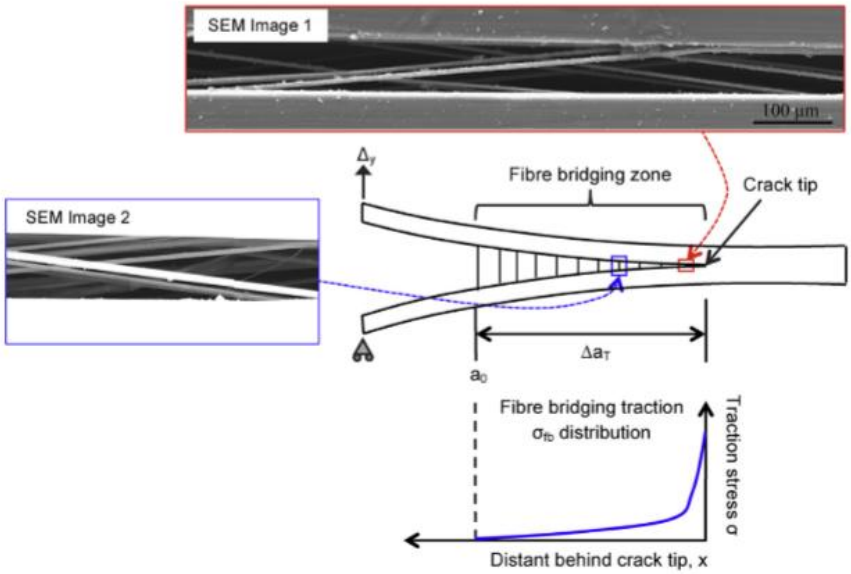

Fig. 21. Schematic of crack bridging by cross-over fibers in the wake of a fatigue delamination crack [16].

1.4. Numerical methods to simulate delamination

The two most adopted numerical methods to study not only the delamination of laminates, but also the debonding of adhesively bonded joints are the Cohesive Zone Models (CZMs) and the Virtual Crack Closure Technique (VCCT).

Many researchers focused their attention on developing CZMs rather than the alternative option. These models are based on the discretization of the interface between adjacent layers and require the development and implementation of a

degradation law to describe the bonding in terms of fracture toughness, initial stiffness and damage evolution. Usually, the choice of the law is a compromise between accuracy and computational efficiency. Moreover, with respect to VCCT, they don't need the introduction of a pre-crack, are less mesh sensitive and some of them allow to consider the effects on crack propagation of the local mode mixities that arise during the propagation itself [1].

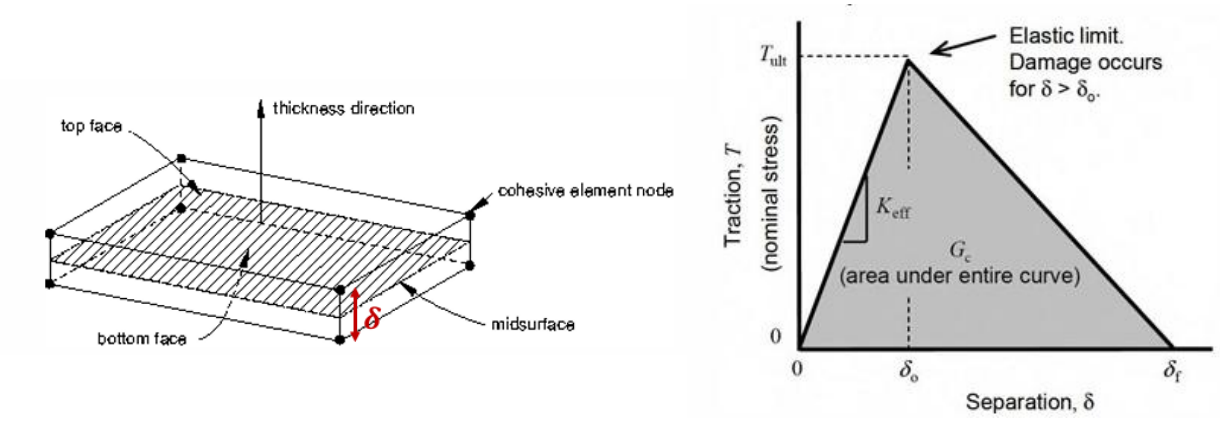

Fig. 22. Schematic of the CZM technique [2].

On the other hand, VCCT is based on the principles of fracture mechanics. It is used to predict maximum loads in quasi-static simulations and the SERR distribution at the crack tip. Since VCCT can be used in combination with Paris-like fatigue crack growth models, its implementation to predict fatigue propagation is simpler than the one required by CZMs [1]. For this reason, some years ago, VCCT was the only available option integrated in Finite Element (FE) software to compute crack propagation. Despite this, there is a lack of studies related to VCCT compared to the ones devoted to CZMs. Pirondi et al. [39] tried to explain this unexpected gap by comparing the predicting capabilities and the time required for the completion of the simulations of the two methods. They noticed that, while the accuracy is similar, VCCT requires up to 1380% more time to perform the same simulation.

In order to evaluate the SERR in correspondence of a node of a FE model, the VCCT relies on the assumption that the strain energy released when a crack of length a increases of an infinitesimal quantity da is equal to the work done by the internal forces to close it by the same amount. As a result, the components I and II of the SERR, G_I and G_{II}, can be calculated as:

$$G_I = \frac{F_{y,2}(v_1 - v_{1^*})}{2bda} \qquad \text{Eq. 34}$$

$$G_{II} = \frac{F_{x,2}(u_1 - u_{1^*})}{2bda} \qquad \text{Eq. 35}$$

where b is the width of the element, $F_{x,2}$ and $F_{y,2}$ are the horizontal and vertical internal forces at node 2, respectively, u_1 and u_{1^*}, are the horizontal displacements of nodes 1

and 1*, respectively, and v_1 and v_{1^*} are the corresponding vertical displacements (Fig. 23).

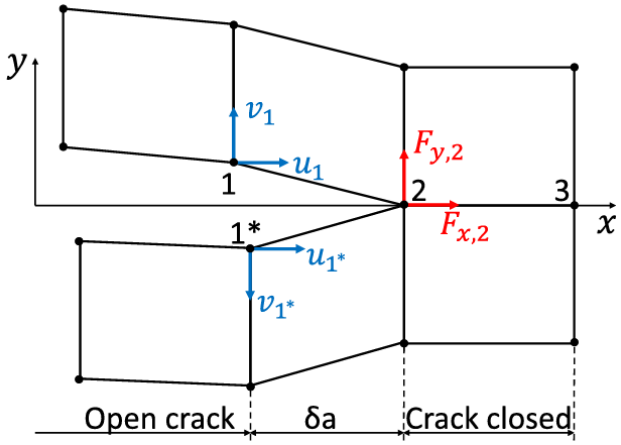

Fig. 23. Schematic representation of the VCCT [1].

For example, in Abaqus, a popular FE software, the criterion for the static release of a node is:

$$\frac{G_{eq}}{G_c} > 0.9 \qquad \text{Eq. 36}$$

where, according to the Benzeggagh-Kenane (BK) law, G_{eq} is the equivalent SERR, as defined in Eq. 5, while G_c is the critical SERR, defined as:

$$G_c = G_{Ic} + (G_{IIc} - G_{Ic})MM^{\eta} \qquad \text{Eq. 37}$$

where $G_{I,c}$ and $G_{II,c}$ are the critical SERR values for mode I and II, respectively, η is a material fitting parameter and MM is the mode mixity, as defined in Eq. 6.

As can be derived from Eq. 36, it is assumed that, at very high propagation rates, the fracture toughness reduces of 10% with respect to its initial value.

Since most of the available works based on VCCT to perform fatigue simulations make use of Abaqus, its implementation of this technique can be considered as a benchmark for VCCT-based simulations [1].

The Abaqus tool to simulate fatigue crack growth operates with the Direct Cycle (DC) algorithm, that is subject to some limitations, such as the long computational time. Another issue is related to the impossibility of updating the Paris law coefficients during the simulation to take into account the possible variations in the propagation law related to the presence of local mode mixities. Besides, as discussed in section 1.2,

a debated topic concerns the choice of the most suitable fatigue correlating parameter: Abaqus adopts the SERR range ΔG as CDF with no possibility to modify it [1].

To overcome the previous problems related to the implementation of the VCCT through the DC algorithm, Martulli and Bernasconi [1] have developed the SSF algorithm. It relies on a series of quasi-static simulations, performed by Abaqus, followed by fatigue calculations executed by an external Python master code (Fig. 24). More details regarding the functioning and potentialities of this algorithm will be given in the next section (1.5).

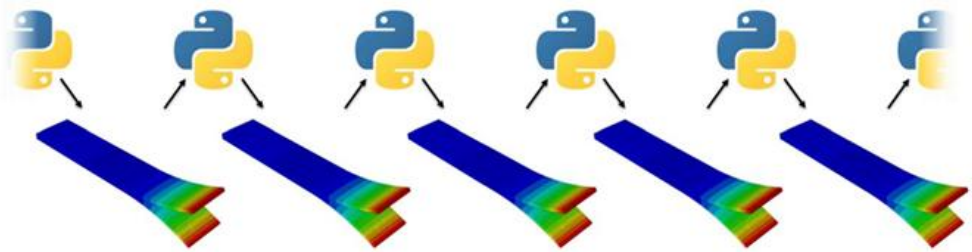

Fig. 24: Representation of the series of quasi-static simulations performed through the integration of Python and Abaqus in the SSF algorithm.

1.5. The SSF algorithm

The main advantages of the SSF algorithm on the Abaqus fatigue propagation tool are the lower computational time and the higher flexibility in the choice of the propagation law, that can be updated also during the simulation by taking into account the local mode mixities, leading to higher accuracy of the results. A comparison of the performance of these two alternatives has been reported in [1] by the authors of the SSF algorithm.

1.5.1. Outline of the SSF algorithm

This algorithm consists in a Pyhton master code that is able to launch Abaqus static simulations and to extract from them the quantities necessary to perform fatigue calculations. In the following lines, the logic behind the functioning of the algorithm is provided.

At first, it is necessary to create in Abaqus a model of the cracked component. The required input information are the geometrical features, the material properties, the applied loads or displacements and the identification of two adjacent surfaces that will be subject to delamination. These surfaces are called slave and master and they contain the set of the bonded nodes that will be released during the fatigue propagation. In particular, all the relevant quantities will be calculated by Abaqus in correspondence of the nodes that lie on the slave surface. It is also important to note that the VCCT

requires a pre-crack to allow the initial evaluation of the local SERRs. For this reason, at least a row of nodes belonging to slave and master surfaces should be excluded from the bonded nodes set so that it can act as a pre-crack.

On the other hand, the Python master code is able to launch sequentially the Abaqus static simulations by giving to it updated input files in which the bonded nodes remaining from the previous iteration are listed. For the first iteration, the bonded nodes contained in the input file created by Abaqus are copied in the corresponding first input file. Once a numerical simulation is done, the following quantities can be extracted in correspondence of each node belonging to the bonded nodes that lie on the slave surface:

$G_{I,\min}$, $G_{II,\min}$, $G_{III,\min}$	minimum SERR values for modes I, II and III
$G_{I,\max}$, $G_{II,\max}$, $G_{III,\max}$	maximum SERR values for modes I, II and III

At this point, Python elaborates these values to establish if a static debonding occurs; if not, fatigue calculations are performed so that at least one node is released. At the end of the computations, the total number of cycles and the bonded region are updated and a new static simulation can start.

The entire fatigue simulation ends once the delamination length or the number of cycles has reached a predefined maximum value.

1.5.2. Criteria for static and fatigue release of a node

A node is released statically if:

$$G_{x,max} > 0.9 G_{x,c} \qquad \text{Eq. 38}$$

where x stands for I or II or III or eq, depending on the critical SERR value that has been used in or that can be extracted from the experimental tests used as reference. To be noted that also the DC algorithm of Abaqus releases a node statically if it exceeds 90% of its fracture toughness (Eq. 36 in section 1.4). If at least a node satisfies the criterion for static release, the total number of cycles is increased by 1.

On the other hand, if no node satisfies the criterion for static release, fatigue calculations are performed. The criterion for the fatigue release of a node is:

$$dmg_{cum} > 0.9 \qquad \text{Eq. 39}$$

where dmg_{cum} it the cumulative damage of a node, that takes into account the consumption of its life due to the previous loading cycles.

More details about the fatigue propagation and cumulative damage calculations are provided in A.1.

1.5.3. Schematic representation of the SSF algorithm

A flow chart of the SSF algorithm is provided in Fig. 25. However, for the complete understanding of the quantities introduced in the diagram, it is necessary to refer to sections 1.5.1 and 1.5.2 and to appendix A.1.

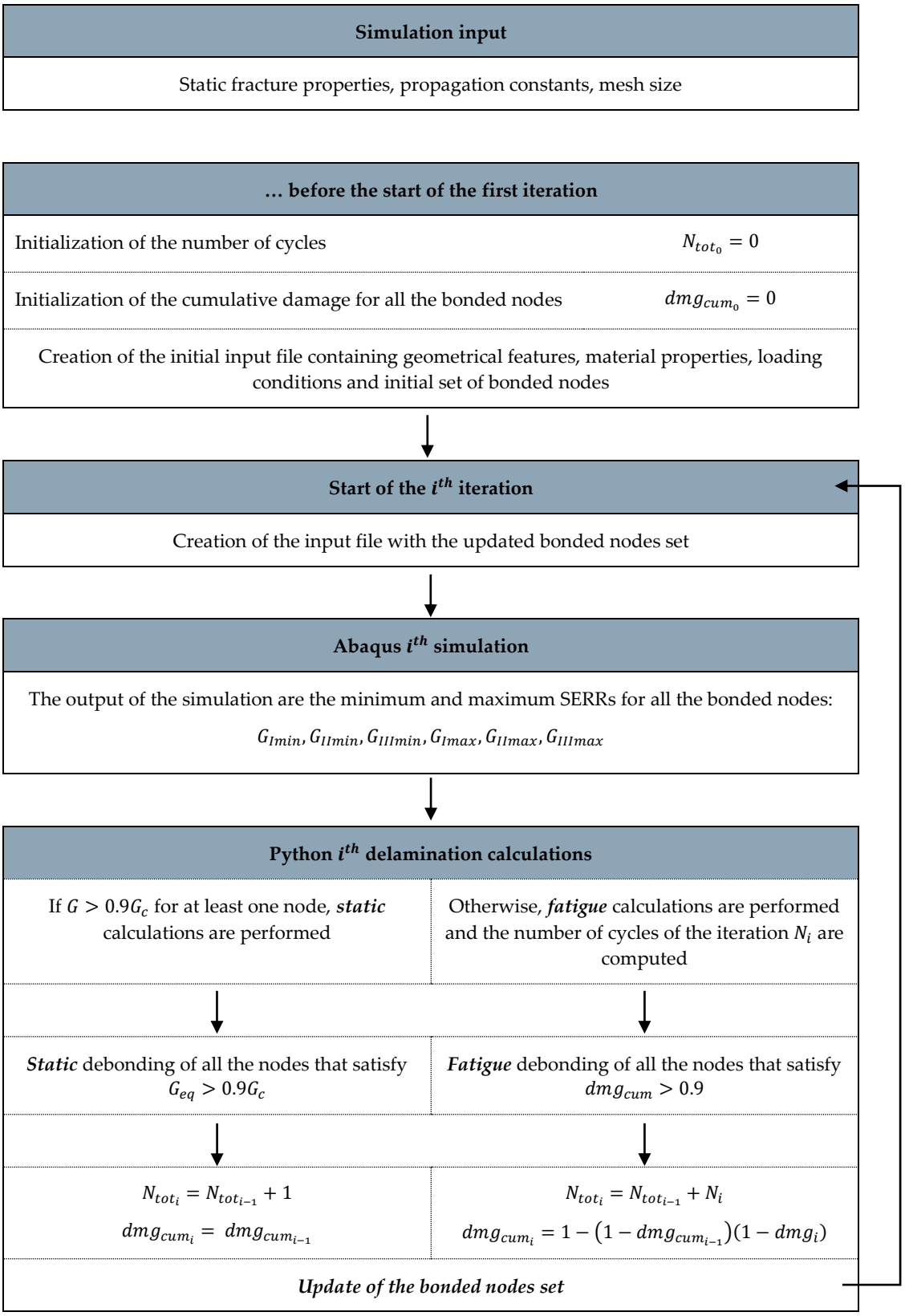

Fig. 25: Flow chart of the SSF algorithm.

2 Materials and methods

In the first section, the modifications made to the SSF algorithm are presented. Then, a description of the two case studies is provided in the second and third sections.

2.1. Differences with respect to the original version of the SSF algorithm

In order to perform faster numerical simulations, the fracture toughness of modes I, II and III within the Abaqus tool are set to a very large value. In this way, no node can be released statically during those simulations and there is no need to extract the information about the bonded nodes at the end of them, since they are the same as the initial ones. Nevertheless, this variation has some implications.

- During the Abaqus simulations, if the values of SERR at the delamination front are higher than the real critical ones, an altered SERR distribution will arise. On the other hand, this should not influence in a significant way the final results. In fact, the nodes that would have been released statically during the numerical simulation of the original SSF algorithm, are the same nodes that satisfy the static debonding criterion also in the Python code.
- It is probable that the number of iterations required to release statically the same nodes will be higher. As a consequence, even if each iteration is faster, it is not possible to state that the time needed to run the entire simulation is actually reduced if static debonding is present.
- The number of cycles for each static iteration of Python will increase by 1 the count of the total number of cycles, while if the nodes are released in Abaqus, no cycle increment is added.

However, it can be argued that, in principle, no static debonding should occur because the applied loads in the simulations are below the critical ones. Nevertheless, due to an intrinsic limitation of the VCCT, stress concentrations arise on the stepped fronts so that in correspondence of discontinuities the SERR values are higher than the critical one. Consequently, all the static debonding, regardless of the way they are accounted for, are to be considered as numerical errors.

The most relevant change to the original version of the SSF algorithm concerns the definition of the law describing the cumulative damage, parameter that quantifies the

reduction of life of a node when subject to a certain number of loading cycles at specific SERR levels.

The original one was:

$$dmg_{cum_i} = dmg_{cum_{i-1}} + dmg_i \quad \text{Eq. 40}$$

where dmg_{cum_i} and $dmg_{cum_{i-1}}$ are, respectively, the cumulative damage of the i^{th} and $(i-1)^{th}$ iterations and dmg_i is the damage of the i^{th} iteration, defined in Eq. 62.

The new one is:

$$\begin{aligned} dmg_{cum_i} &= 1 - \left(1 - dmg_{cum_{i-1}}\right)(1 - dmg_i) \\ &= dmg_{cum_{i-1}} + \left(1 - dmg_{cum_{i-1}}\right)dmg_i \end{aligned} \quad \text{Eq. 41}$$

The demonstration of Eq. 41 is provided in A.1.

In both the formulations, dmg_{cum_i} is function of $dmg_{cum_{i-1}}$ and dmg_i.

Since for the most critical node of the i^{th} iteration dmg_i is equal to 1, the new law guarantees that dmg_{cum_i} doesn't exceed the limit value of 1. Conversely, the implementation of Eq. 40 would cause an underestimation of the actual remaining life the nodes.

Besides, it was added the possibility to extract, along with the maximum SERRs, G_{max}, also the minimum ones, G_{min}. In this way, a wider range of propagation laws can be adopted and a numerical evaluation of local mode mixities (Eq. 6) and load ratios (Eq. 14) can be performed.

Finally, in the new version of the algorithm, several files are created and/or updated in each iteration to monitor in real time how the simulation is proceeding and to post-process the data.

2.2. Case study 1: delamination of a DCB specimen under different mode mixities

2.2.1. Experimental test

To validate the SSF algorithm, Martulli and Bernasconi [1] considered three experimental tests on fatigue delamination of composites published by [10], [40], [41]. The one that is analyzed also in this work concerns the study conducted by Armanios et al. on the delamination growth under mode I, mode II and mixed mode fatigue loading of the HTA/6376C, a CFRP laminate, whose mechanical properties are reported in Table 1. Among the objectives of their study, there is the determination of the Paris-equation constants for the three analyzed modes

Table 1: Mechanical properties of the HTA/6376C composite laminate [10].

Symbol	*Description*	*Value*
$E_F = E_1$	Elastic modulus in the fiber direction	120 GPa
$E_T = E_2 = E_3$	Elastic modulus in the transverse direction	10.5 GPa
$G_{12} = G_{13}$	Shear modulus in the planes parallel to the fibers	5.25 GPa
G_{23}	Shear modulus in the plane transverse to the fibers	3.48 GPa
$\upsilon_{12} = \upsilon_{13}$	Poisson coefficient in the planes parallel to the fibers	0.3
υ_{23}	Poisson coefficient in the plane transverse to the fibers	0.51

The specimen lay-up was $[0_{12}//(\pm 5/0_4)_S]$, where the sign "//" refers to the plane of the artificial delamination. The off-axis angle was introduced to reduce the fiber bridging during the delamination growth. Since Olsson et al. [42] found that the thickness of the starter film affects the toughness at the initiation of the crack growth, the artificial starter crack was made of a very thin polyimide film (7.5 μm-thick).

The geometrical features and dimensions of the specimen are shown in Fig. 26.

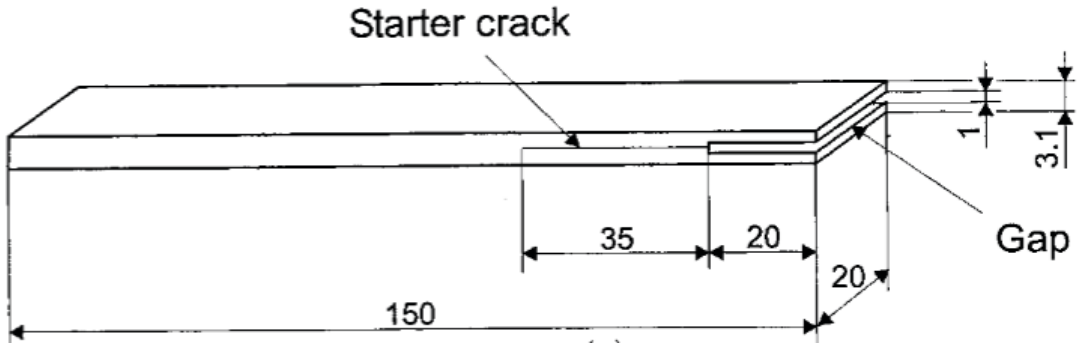

Fig. 26: Geometrical features and dimensions of the CFRP specimen [10].

For pure mode I and mode II experiments, DCB and ENF tests were employed, while for the mixed mode ones the MMB test was used. All the tests have been performed in displacement control at 0.1 load ratio.

The delamination growth length was measured with an instrumented travelling microscope at intervals, temporarily stopping the application of the loads. The crack tip position was identified on both the edges, with an accuracy of 0.01 mm.

In order to plot the crack propagation rate, the researchers [10] followed the considerations of Wilkins et al. [43] to overcome the difficulties in the evaluation of the SIF range, required by the original version of the Paris equation. However, since the tests were performed with a load ratio of 0.1, the minimum SERR in a loading cycle was much smaller than the maximum one. Therefore, the SERR range was approximated by the maximum SERR only, as shown by the following relationship derived from Eq. 14:

$$\frac{G_{min}}{G_{max}} = R^2 = 0.1^2 = 0.01 \Longrightarrow \Delta G = G_{max} - G_{min} = 0.99 G_{max} \simeq G_{max}$$

As a consequence, Armanios and his colleagues [10] adopted as correlating parameters the maximum SERR G_{max} (Eq. 20) and the normalized maximum SERR $\hat{G}_{\max}$ (Eq. 21) to plot the fatigue propagation results.

The G_{max} was calculated through the compliance method [11], as described in section 1.1.3. In particular, the load-only formulation was adopted, so that no displacement measurements were needed during the tests. The expression for G_I is reported in Eq. 11b.

The critical SERR values, obtained in the quasi-static tests conducted by Johnson et al. [45], are reported in Table 2.

Table 2: Critical values of SERR for the composite laminate used by [10] for the different loading modes.

$G_{Ic}\ [N/mm]$	$G_{IIc}\ [N/m]$	$G_{50\%mix,c}\ [N/m]$
0.260	1.002	0.447

2.2.2. Numerical model

To model the specimen that was used in the fatigue tests run by Armanios et al. [10], two identical laminates are assembled. Each laminate has the same mechanical properties, dimensions and stacking sequence of the actual specimens, apart from the overall length, that has been reduced from 150 mm to 100 mm The model of the specimen and the corresponding dimensions are reported in Fig. 27 and Table 3, respectively.

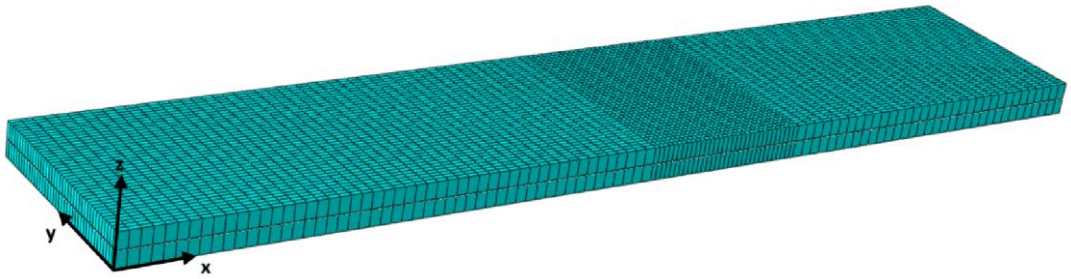

Fig. 27: Numerical model of the DCB specimen.

Table 3: Dimensions of the DCB specimen.

Geometrical dimension	*Value*
Total length of the specimen	100 mm
Initial unbonded length, including the pre-crack	35 mm
Propagation length	15 mm
Tied length	50 mm
Total thickness of the specimen	3.1 mm
Width of the specimen	20 mm

In order to simulate the fatigue test, the specimen has been divided into three zones: the unbonded zone, that corresponds to the starter crack artificially created in the actual specimen and that includes also the pre-crack needed by the VCCT, the propagation zone, where the delamination is allowed to grow, and the tied zone. These latter two zones are not distinguished in the experimental case.

On the basis of the mesh sensitivity analysis performed by Martulli and Bernasconi [1], a 0.5 mm mesh was used only in correspondence of the pre-crack and of the propagation zone, while a coarser mesh of 1 mm is adopted in the remaining zones. The mesh elements are the reduced integration 8-nodes continuum shell elements (SC8R), with only one element through the thickness of each laminate.

To investigate the fatigue delamination of the laminate under mode I, mode II and mixed mode loadings, Armanios et al. [10] have adopted, respectively, DCB, ENF and MMB tests under displacement control. However, in this work the approach followed by Martulli and Bernasconi [1] has been adopted. The researchers [1] simulated the

three loading modes by applying different bending moments at the unbonded tips of the laminate (Fig. 28), as suggested by [12]. In case of mode I, the applied moments are equal and opposite, in case of mode II, they are equal, and for the mixed mode case, they are proportional through the parameter ρ. In particular, the proportionality coefficient ρ is derived from the beam theory and, in order to achieve a 50% mode mixity, its value is:

$$\rho = \frac{1 - \frac{\sqrt{3}}{2}}{1 + \frac{\sqrt{3}}{2}} \qquad \text{Eq. 42}$$

Thanks to the loading conditions the specimens are subject to, the theoretical applied SERRs don't depend on the crack length. As a result, the delamination rate should remain constant during propagation. The theoretical SERR can be computed with the following formulas [12], [46]:

$$G_I = \frac{M^2}{EIB} \qquad \text{Eq. 43}$$

$$G_{II} = \frac{3M^2}{4EIB} \qquad \text{Eq. 44}$$

$$G_I = G_{II} = \frac{3}{4\left(1 + \frac{\sqrt{3}}{2}\right)^2} \frac{M^2}{EIB} \qquad \text{Eq. 45}$$

where M is the applied moment, E is the material Young modulus in the direction of the fibers, I is the second moment of inertia and B is the specimen width.

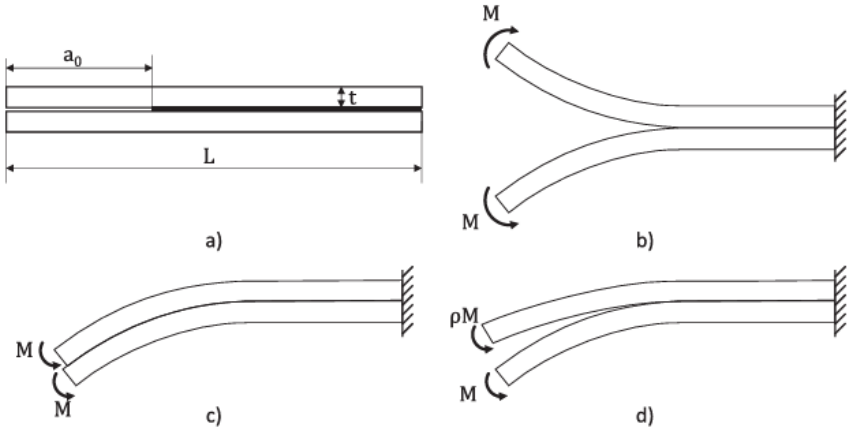

Fig. 28. DCB specimen represented in four situations: unloaded (a), mode I loading (b), mode II loading (c), mixed mode loading (d) [1].

In total, six simulations have been performed, two for each loading mode. The moments that have been applied are reported in Table 4.

Table 4: Applied moments.

Mode	*Simulation*	*Moments [Nmm]*	
Mode I	1	1000	-1000
	2	1500	-1500
Mode II	3	2000	2000
	4	3100	2000
Mixed Mode	5	1500	107.7
	6	2000	143.6

2.2.3. Fatigue propagation law

The correlating parameter of the implemented propagation law is the normalized maximum SERR $\hat{G}_{\max}$. The corresponding equation, that has been already introduced in section 1.2.1, is:

$$\frac{da}{dN} = D\left(\frac{G_{max}}{G_c}\right)^m = D(\hat{G}_{max})^m \qquad \text{Eq. 21}$$

The SSF algorithm evaluates G_{max}, G_c and the coefficients D and m for each node in each fatigue iteration, as described in the next lines.

G_{max} is the maximum equivalent SERR, that can be calculated according to Eq. 5 by using the maximum SERR values of the three modes ($G_{I,\max}$, $G_{II,\max}$, $G_{III,\max}$) extracted from the quasi-static simulation.

The dependence of the fracture toughness G_c on the mode mixity MM is taken into account by Eq. 37. The material constants are reported in Table 5 while the mode mixity is calculated through Eq. 6 in correspondence of $G_{I,\max}$, $G_{II,\max}$ and $G_{III,\max}$.

Also the coefficients D and m depend on the mode mixity. They are calculated by means of the equations presented in [46]:

$$\ln(D) = \ln(D_I) + \ln(D_m)\,MM + \ln\left(\frac{D_{II}}{D_I D_m}\right) MM^2 \qquad \text{Eq. 46}$$

$$m = m_I + m_m MM + (m_{II} - m_I - m_m) MM^2 \quad \text{Eq. 47}$$

being D_I and m_I the coefficients of the propagation law for mode I ($MM = 0$) and D_{II} and m_{II} for mode II ($MM = 1$), while D_m and m_m are material fitting parameters. All these quantities are provided in Table 5.

Table 5: Fatigue material constants [1].

$D\ [mm/cycle]$		
D_I (pure mode I)	D_{II} (pure mode II)	
0.0616	2.99	
$m\ [-]$		
m_I	m_{II} (mode II)	
5.4	4.5	
Material fitting parameters		
D_m [mm/cycle]	m_m [-]	η [-]
458,087	4.94	2.73

2.3. Case study 2: master propagation curve for mode I fatigue loading of a composite laminate

2.3.1. Experimental test

The second case study, aimed at studying the load ratio effect on the performance of the SSF algorithm, is based on the experimental work of Simon et al. [13] about the identification of a master propagation curve, independent from the load ratio, for a CFRP laminate.

The researchers have carried out both quasi-static and constant amplitude fatigue tests on DCB specimens made of a plain-woven laminate prepreg (G0814/913) under mode I loading. The quasi-static tests were necessary to determine the material resistance curve as a function of the delamination length, while the fatigue ones allowed to identify the propagation rate curves for four values of applied displacement ratios.

The specimens were arranged in a multi-directional layup of 15 plies, as represented in Fig. 29. The mechanical properties of the plies are reported in Table 6.

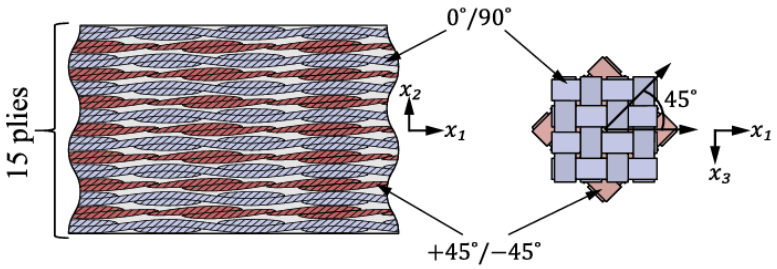

Fig. 29: Laminate layup and plies arrangement of the specimens [13].

Table 6: Mechanical properties of the 0/90 and +45/-45 plies of the composite laminates [13].

Symbol	*Description*	*0/90 plies*	*+45/-45 plies*
$E_1 = E_3$	In plane elastic modulus	57.3 GPa	13.6 GPa
E_2	Out of plane elastic modulus	7.6 GPa	7.6 GPa
G_{13}	In plane shear modulus	3.9 GPa	27.6 GPa
$G_{23} = G_{21}$	Out of plane shear moduls	2.5 GPa	2.5 GPa
υ_{13}	In plane Poisson coefficient	0.04	0.77
$\upsilon_{23} = \upsilon_{21}$	Out of plane Poisson coefficient	0.07	0.07

To initiate the crack, a PTFE film 35.4 μm thick was inserted between the 7^{th} and 8^{th} plies.

Both the quasi-static and the fatigue tests have been carried out on DCB specimens loaded by means of two piano hinges (Fig. 30a) and a support was placed under the free edge. The sides of the specimen were painted with a white acrylic paint from the initial delamination front onwards, reference marks were drawn on it and a millimeter paper was attached to the top of the specimen in order to allow the calibration of the pictures taken during the test (Fig. 30b).

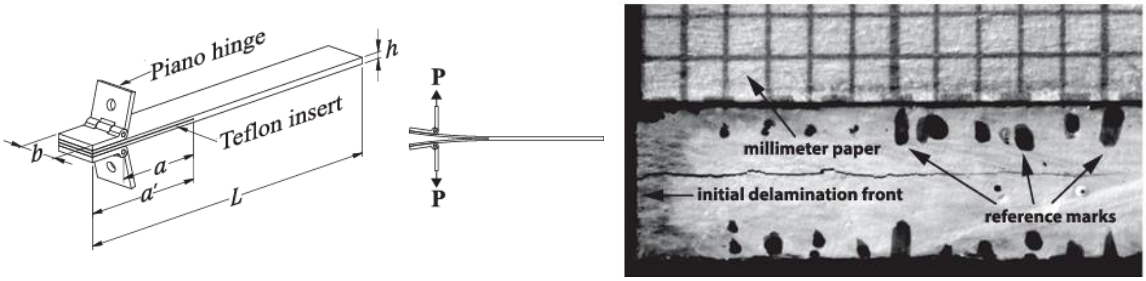

(a) (b)

Fig. 30: (a) Representation of the specimen geometrical features and loading conditions; (b) Picture of a specimen at the end of the test [13].

All the tests were run in displacement control loading conditions. The researchers have proven that the machine used to test the specimens had a negligible compliance with respect to the one of the specimens so that the specimen opening displacement δ was assumed to be equal to the loading machine actuator displacement d.

The quasi-static tests were performed on a total of five specimens. The authors observed a high dependence of the specimen compliance on the initial delamination length, while the fracture toughness behavior was similar for all the specimens. In particular, after an initial phase in which it increased monotonically as the delamination advances, it reached a plateau value of 0.711 N/mm (Table 7).

Table 7: Fracture toughness dependence on the delamination growth [13].

Phase	$\Delta a\ [mm]$	$G_{Ic}\ [N/m]$
Initial	0	508
Monotonic rise	$0 \div 10$	$586 + 27(\Delta a)^{0.65}$
Stable	> 10	711

Concerning the constant displacement amplitude fatigue tests, they were performed on eight specimens from batch 5 (Table 8). At the beginning, a quasi-static displacement was applied to form a natural delamination front from the edge of the Teflon insert. The imposed maximum displacement during the fatigue test, d_{max}, was set equal to the displacement recorded in this preliminary procedure while the minimum one, d_{min}, was calculated from the displacement ratio of the test, R_d, with the following equation:

$$d_{min} = R_d d_{max} \quad \text{Eq. 48}$$

In order to monitor the delamination growth, pictures of the specimen front side were taken at intervals by interrupting the test, while at end of it the final delamination length was measured on both sides. On the other hand, the number of cycles N, the maximum and minimum actuator displacements d_{max} and d_{min} and the maximum and minimum loads P_{max} and P_{min} were recorded at each cycle.

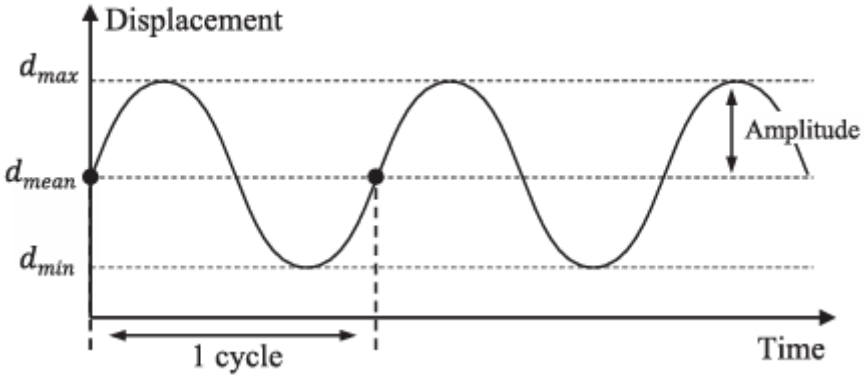

Fig. 31: Displacement - time curve of the constant amplitude fatigue tests [13].

In Table 8 the eight specimens are listed along with the corresponding displacement ratio R_d, the maximum applied displacement d_{max}, the delamination length before the application of the quasi-static load a_0, the delamination length at the beginning of the fatigue loading a_i, the final delamination length a_f and the total number of cycles N_{tot}.

Table 8: Fatigue specimen data [13].

Specimen	R_d $[-]$	d_{max} $[mm]$	a_0 $[mm]$	a_i $[mm]$	a_f $[mm]$	N_{tot} $[cycles]$
FTG-5-02	0.1	11.6	49.0	51.1	68.4	1,770,600
FTG-5-08	0.1	13.0	49.2	54.2	71.7	1,638,600
FTG-5-03	0.33	11.2	47.6	49.2	64.4	2,581,500
FTG-5-06	0.33	10.8	48.3	50.4	64.6	2,940,000
FTG-5-04	0.5	11.5	48.1	50.2	59.7	2,700,000
FTG-5-07	0.5	12.0	49.0	51.1	64.4	2,870,000
FTG-5-05	0.75	14.4	49.0	53.9	60.0	3,000,000
FTG-5-09	0.75	13.0	48.6	51.8	58.5	954,900

In order to identify the propagation law equations by fitting the experimental data, it was necessary to estimate the values of G_I during the delamination.

Due to the multi-directional layup of the specimen, the delamination occurred between plies with different material directions. As a result, to calculate G_I, Simon et al. [13] didn't follow the methods suggested the ASTM standard D5528-13 for UD laminates but relied on a Finite Element Analysis (FEA). For each fatigue-tested specimen, five numerical simulations have been performed in correspondence of five delamination lengths that span from the initial to the final delamination lengths. It was assumed that the front was straight and that the mode mixity was zero so that the extracted values of SERR were regarded to as $G_{I,FE}$. At the end of the simulations, these values were fitted with the delamination lengths and the following analytical formulation was obtained:

$$G_{I,FE} = C_1 a^2 + C_2 a \qquad \text{Eq. 49}$$

where C_1 and C_2 are fitting parameters. Since the specimens have slightly different dimensions, each one has its own fitting parameters.

All the FE simulations were performed by applying a load of 20 kN (P_{FE}) and, since the SERR is proportional to the square of the load, the actual G_I was calculated as:

$$G_I = \left(\frac{P}{P_{FE}}\right)^2 G_{I,FE} = \left(\frac{P}{P_{FE}}\right)^2 (C_1 a^2 + C_2 a) \qquad \text{Eq. 50}$$

The delamination length was estimated for each cycle thanks to the power law (Eq. 52) that was fitted by using the recorded values of a and the corresponding values of the compliance C, that were easily calculated through Eq. 51:

$$C = \frac{d_{max} - d_{min}}{P_{max} - P_{min}} \quad \text{Eq. 51}$$

The power law used to estimate a was:

$$a = A_1 C^{A_2} \quad \text{Eq. 52}$$

where A_1 and A_2 are fitting parameters.

At this point, the delamination length was expressed as a function of the number of cycles by fitting the data plotted in the $a - N$ plane:

$$a = f(N) \quad \text{Eq. 53}$$

Finally, the propagation rate has been analytically calculated by differentiating Eq. 53:

$$\frac{da}{dN} = \frac{d}{dN}[f(N)] \quad \text{Eq. 54}$$

As a result, for each cycle it is possible to correlate the value of G_I (Eq. 50), function of a and P, to the corresponding value of propagation rate (Eq. 54), function of N.

At first, Simon et al. [13] used as correlating parameters the normalized maximum SERR $\hat{G}_{max}$ and the normalized effective SERR range $\Delta\hat{G}_{eff}$. Then, with the aim of creating a master curve independent from the load ratio, they employed a modified version of the Hartman-Shijve equation (Eq. 29).

More details concerning the implemented propagation law in the SSF algorithm will be given in the section 2.3.3.

2.3.2. Numerical model

Four constant amplitude fatigue tests have been simulated. The analyzed specimens are listed in Table 9 while a graphical representation is given in Fig. 32.

Since the starter crack was not exactly at half of the thickness of the specimen, two different parts were modelled in the Abaqus software by using the composite layup tool and then assembled.

As done for the first case study, the numerical specimens were partitioned into three parts: an unbonded zone, a propagation zone and a tied zone. Also a pre-crack constituted by two rows of nodes was created to allow the application of VCCT. Since the maximum delamination reached in the fatigue tests was 15 mm, the propagation

zone was set to a length of 25 mm to limit the number of bonded nodes and, consequently, the computational time.

The displacement was applied at the center of the right edge of the upper laminate, while a pin constrained the right edge of the lower one. Besides, a spring of stiffness $k = 12\ N/mm$ was interposed between the upper laminate and the point of application of the displacement due to compliance issues. More details about the addition of the spring are provided in A.2.

For all the specimen models, a mesh of 1 mm was used.

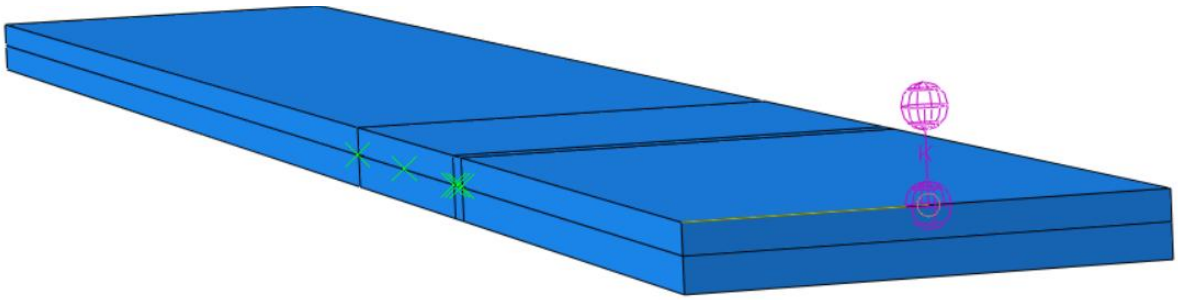

Fig. 32: Abaqus model of the specimen FTG-5-02.

In Table 9, the starter crack length a_0 and the specimen length L, width b and thickness h are reported for the simulated specimens. Concerning the layup arrangement, the geometrical features and the material properties, it is possible to refer to Fig. 29, Fig. 30a and Table 6, respectively, while the information about the applied displacement and the load ratio are reported in Table 8.

Table 9: Dimensions in mm of the numerical specimens.

Specimen	a_0	L	b	h
FTG-5-02	51	204	26	3.63
FTG-5-03	49	204	26	3.65
FTG-5-07	51	204	26	3.63
FTG-5-05	54	204	26	3.67

2.3.3. Fatigue propagation law

Fatigue delamination was predicted by the SSF algorithm through the modified version of the Hartman-Shijve equation [13], presented in section 1.2.2:

$$\frac{da}{dN} = D\left(\frac{\sqrt{\hat{G}_{max}} - \sqrt{\hat{G}_{max}^{(th)}}}{\sqrt{1-\sqrt{\hat{G}_{max}}}}\right)^{m} = D(\Delta\bar{K})^{m} \qquad \text{Eq. 29}$$

where $\hat{G}_{max}^{(th)}$ is the normalized threshold maximum SERR with respect to the fracture toughness G_c.

Since the normalized effective SERR range $\Delta\hat{G}_{eff}$ is defined as (section 1.1.4):

$$\Delta\hat{G}_{eff} = \left(\Delta\sqrt{\hat{G}}\right)^2 = \left(\sqrt{\hat{G}_{max}} - \sqrt{\hat{G}_{min}}\right)^2 = \hat{G}_{max}(1-R)^2 \qquad \text{Eq. 16}$$

and its threshold value $\Delta\hat{G}_{eff}^{(th)}$ is assumed to be constant (section 1.2.1), the normalized threshold maximum SERR $\hat{G}_{max}^{(th)}$ is expressed as:

$$\hat{G}_{max}^{(th)} = \frac{\Delta\hat{G}_{eff}^{(th)}}{(1-R)^2} \qquad \text{Eq. 30}$$

$\Delta\hat{G}_{eff}^{(th)}$ was calculated by the authors as the intersection point of the $\Delta\hat{G}_{eff}$ curves plotted as functions of the number of cycles N (Fig. 33).

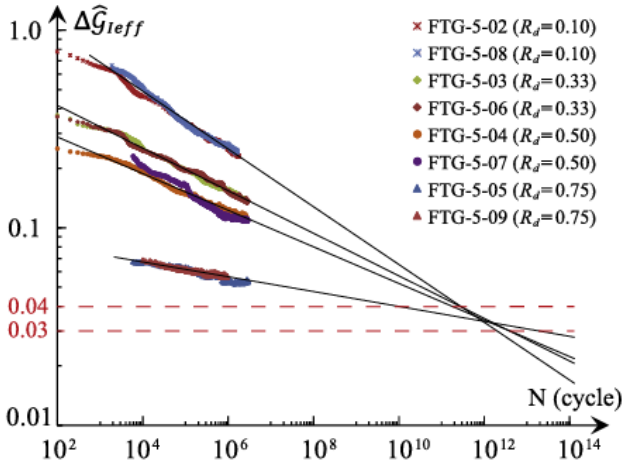

Fig. 33: Diagram used by [13] to identify the normalized threshold effective SERR range.

The coefficients and constants of the equation of the master propagation curve have been provided by Simon et al. [13] (Table 10).

Table 10: Propagation law parameter of the master curve identified by [13].

$D\ [mm/cycle]$	m [-]	$\Delta\hat{G}_{eff}^{(th)}$ [-]	$G_{Ic}\ [N/mm]$ *stabilized*
$1.1e-4$	5.2	0.0365	0.711

It is important to note that, in the present work, the fracture toughness was considered constant and equal to its stabilized value, as reported in Table 10, even if experimental results gave evidence of its dependence on the propagation length (Table 7).

Finally, the propagation law implemented in the SSF algorithm was:

$$\frac{da}{dN} = 1.1e-4\left(\frac{\sqrt{\hat{G}_{max}}-\sqrt{\frac{0.0365}{(1-R)^2}}}{\sqrt{1-\sqrt{\hat{G}_{max}}}}\right)^{5.2}\ \frac{mm}{cycle} \qquad \text{Eq. 55}$$

3 Results

3.1. Case study 1: delamination of a DCB specimen under different mode mixities

The simulations were made on a numerical model of the CFRP laminate used by Armanios et al. [10] in their experimental tests and the propagation law implemented in the SSF algorithm was based on the corresponding output curves. Since in experimental tests and numerical simulations the loading conditions were different, it has no physical meaning to evaluate if the numerical model propagated as the real one. However, it is still possible to determine if the SSF algorithm was able to predict the propagation rates and if the new damage formulation improved the performance.

3.1.1. Comparison between expected and predicted propagation rates

As discussed in section 2.2.2, two simulations were carried out for each loading mode by applying different bending moments (Table 4). The propagation law, presented in section 2.2.3, is reported below to facilitate the comprehension of the following analysis.

$$\frac{da}{dN} = D\left(\frac{G_{max}}{G_c}\right)^m \qquad \text{Eq. 21}$$

To calculate the expected propagation rate of each simulation, it is assumed that:

- The maximum SERR distribution was uniform on the delamination front.
- The maximum SERR on the delamination front was constant during propagation.
- The numerical mode mixity, that was computed through the numerical SERRs, was equal to the theoretical one.

The theoretical maximum SERR $G_{max}^{(t)}$ (Eq. 43, Eq. 44, Eq. 45), the critical SERR G_c (Eq. 37) and the coefficients of the propagation law D (Eq. 46) and m (Eq. 47) are calculated according to the mode mixity of each simulation (Table 11). By means of the propagation law (Eq. 21), the expected propagation rates are estimated (

Table 12).

Table 11: Mode mixity dependent quantities.

Mode	*I*	*II*	*Mixed*
MM	0.0	1.0	0.5
$G_c\ [N/mm]$	0.266	1.002	0.377
$D\ [mm/cycle]$	0.0031	0.1490	0.2113
m	5.40	4.50	6.41

Table 12: Expected propagation rates.

Simulation	*1*	*2*	*3*	*4*	*5*	*6*
$G_{max}^{(t)}[N/mm]$	0.067	0.151	0.201	0.484	0.065	0.116
$G_{max}^{(t)}/G_c$	0.252	0.568	0.201	0.483	0.173	0.307
$da/dN\ [mm/cycle]$ *Expected*	**1.82e-6**	**1.45e-4**	**1.09e-4**	**5.60e-3**	**2.72e-6**	**1.09e-4**

On the other hand, the propagation rates predicted by the SSF algorithm are calculated as the ratio between the final delamination length, a_f, and total number of cycles that were necessary to release all the nodes in the row, N_{tot}. The results are reported in Table 13.

Table 13: Predicted propagation rates.

Simulation	*1*	*2*	*3*	*4*	*5*	*6*
$a_f\ [mm]$	4	4	4	4	4	4
$N_{tot}\ [cycles]$	1,195,811	14,704	36,127	686	915,446	23,182
$da/dN\ [mm/cycle]$ *Predicted*	**3.35e-6**	**2.72e-4**	**1.11e-4**	**5.83e-3**	**4.37e-6**	**1.73e-4**

Finally, the comparison between expected and predicted propagation rates is given in Table 14 and can be visualized in Fig. 34.

Table 14: Percentage of overestimations of the propagation rates.

Simulation	*1*	*2*	*3*	*4*	*5*	*6*
Percentage of overestimation	**+84%**	**+88%**	**+2%**	**+4%**	**+61%**	**+59%**

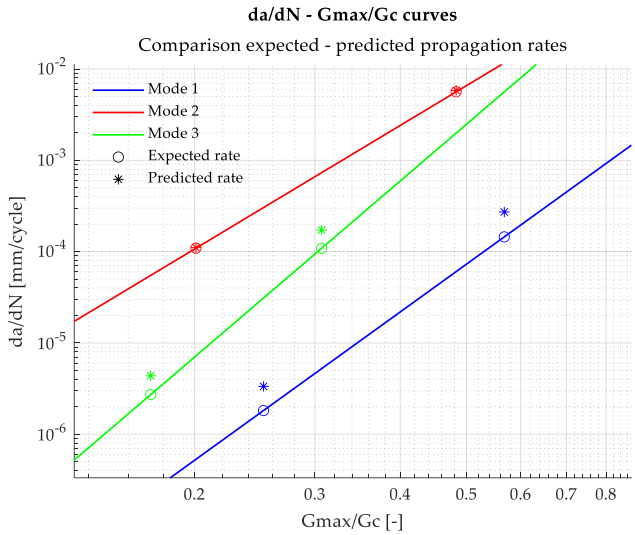

Fig. 34: Comparison between expected and predicted propagation rates.

It can be noted that the results are quite accurate in the case of mode II loading conditions, while the propagation rates were highly overestimated in the mode I and mixed mode simulations.

The possible reasons at the basis of the disagreement between expected and predicted delamination rates are various:

- The numerical mode mixity, the effect of which was taken into account in the SSF algorithm, was different with respect to the theoretical one.
- The mean value of the numerical maximum SERR distribution on the delamination front was different with respect to the theoretical one.
- The quasi-static simulations were affected by numerical errors in the SERR calculation.

During the simulations, the numerical value of the mode mixity was calculated according to Eq. 6 for each node at each iteration. Concerning modes I and II, the local mode mixities were equal to the theoretical ones, while the mode mixity distribution

was not uniform on the delamination front for the mixed mode case (Fig. 35). However, since the average value matched the theoretical one for both the initial and final fronts, the mode mixity effect on the propagation law, even if locally present, is not considered as a cause of the overestimation of the delamination rates.

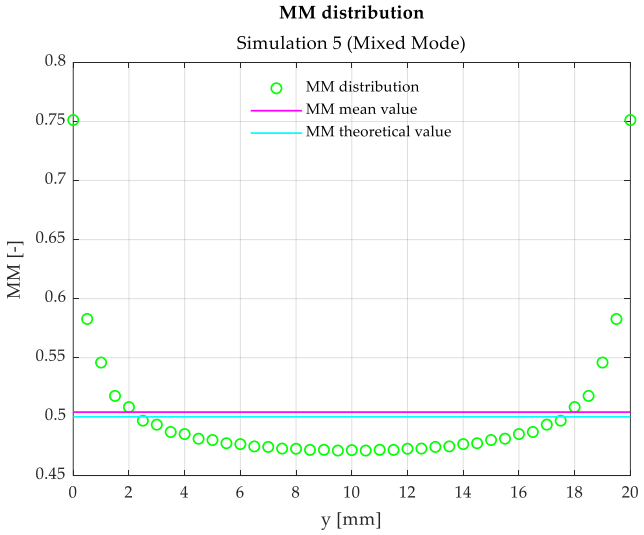

Fig. 35: Mode mixity distribution along the initial delamination front of Simulation 5.

Similarly, the numerical SERR distribution is compared with the theoretical one obtained from [12] (Eq. 43, Eq. 44, Eq. 45). Since the distribution was not uniform, the mean SERR value is used in the comparison (Table 15).

Table 15: Comparison between analytical and numerical mean SERR values on the delamination front.

Simulation	*1*	*2*	*3*	*4*	*5*	*6*
$G_{max}^{(t)}$ $[N/mm]$	0.067	0.151	0.201	0.484	0.065	0.116
$G_{max}^{(num)}$ $[N/mm]$	0.066	0.148	0.200	0.481	0.064	0.114
Percentage difference	**-1.5%**	**-2.0%**	**-0.4%**	**-0.6%**	**-1.5%**	**-1.7%**

From Table 15 it can be observed that in all the simulations the mean value of the numerical maximum SERR distribution was slightly lower than the theoretical one. Knowing that the propagation rate increases as the maximum SERR increases (Eq. 21), the new expected propagation rates would be lower than the original ones and the difference with the predicted propagation rates would be even higher. Since the

difference is not as high and the effect would be opposite, the error is not caused by the method adopted to estimate the mean SERR value.

In Fig. 36, the SERR distributions on the delamination fronts corresponding to the first three iterations of a simulation are represented for mode I, mode II and mixed mode.

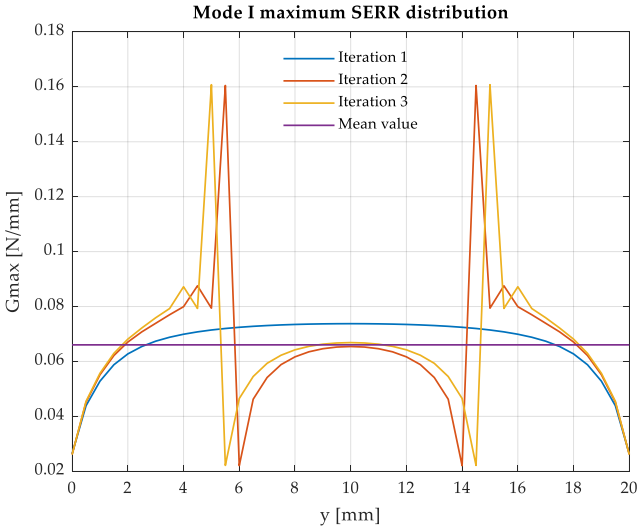

(a) Simulation 1

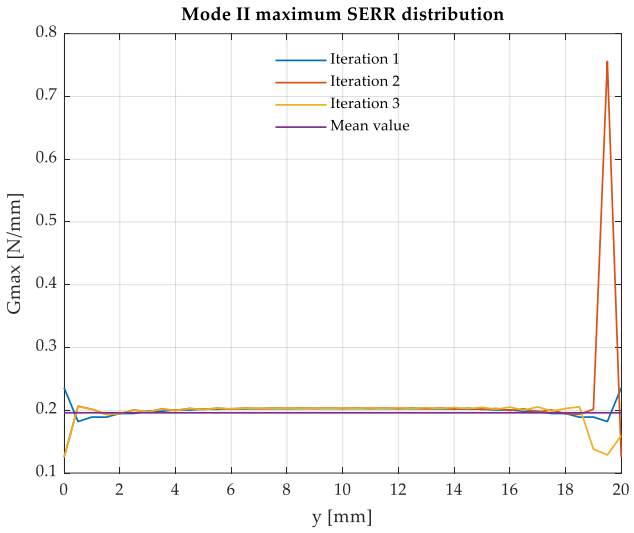

(b) Simulation 3

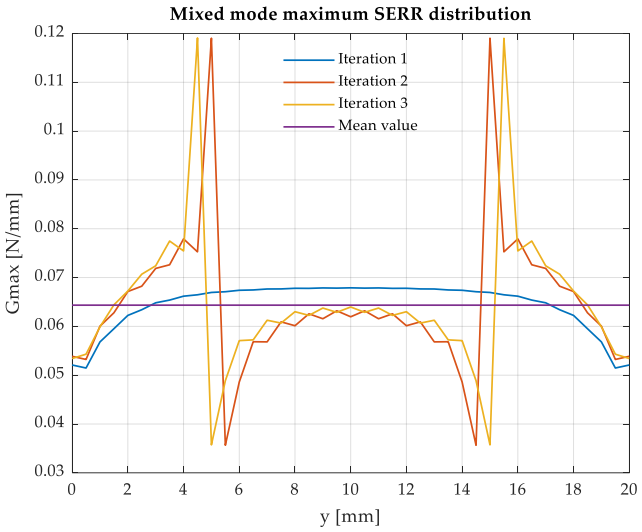

(c) Simulation 5

Fig. 36: Maximum SERR distributions on the front in the first three iterations of mode I, mode II and mixed mode.

During an iteration, only the nodes with the highest values of SERR are released. This introduces a curve in the delamination front that, on a regular mesh, is represented by a stepped profile. The discontinuities behave like stress risers causing peaks in the SERR distribution and the consequent underestimation of the number of cycles needed to release the affected nodes. Since the complete debonding of a row occurs in several iterations, the total number of cycles for its release is calculated as the sum of the number of cycles of the single iterations. If in some of them the SERR distribution is characterized by peaks, the number of cycles to debond the entire row is underestimated and, consequently, the predicted propagation rate overestimated. As a result, both the frequency and the amplitude of such numerical errors have a significant influence on the evaluation of the propagation rate.

In mode I simulations (Fig. 36a), the debonding of a row started with the release of the central nodes of the front. Then, in each of the subsequent iterations up to the end of the row, only the two specular nodes in correspondence of the peaks were released. Depending on the amplitude of the applied load, the release happened due to fatigue (Simulation 1) or statically due to an exceedance of the 90% of the fracture toughness (Simulation 2). However, in both cases, the number of cycles for the debonding of a row was lower than the real one because of the overestimated maximum SERR values. In particular, in case of Simulation 2, since each static release caused an increment of just 1 cycle to the total count of the number of cycles, it is possible to affirm that each row debonded in a number of cycles that was approximately equal to the one necessary to release the central nodes only. This could be the reason why the error in Simulation 2 is 4% higher than the one of Simulation 1, in which, even if SERR peaks were present, all the nodes were released by fatigue in more than one cycle.

Also in mode II simulations (Fig. 36b) some numerical errors were present but their impact was lower than in mode I. A significant spike occurred in the second iteration due to a local increment of mode III SERR, but both in the first and in the third ones the peak to average ratio didn't exceed the value of 1.2 (Table 16).

Finally, the maximum SERR distributions of the mixed mode simulations (Fig. 36c) were similar to the ones of mode I but the peaks were less pronounced thanks to the co-presence of mode II, less sensitive to numerical errors.

Table 16: Peak to average ratio of the maximum SERR distribution.

Simulation	*1*	*2*	*3*	*4*	*5*	*6*
Iteration 1	1.1	1.1	1.2	1.2	1.1	1.1
Iteration 2	2.4	2.4	3.6	3.1	1.8	1.8
Iteration 3	2.4	2.4	1.1	1.1	1.9	1.8

The effects of the previously discussed numerical errors on the predicted delamination rates can be amplified by the steepness of the propagation curve (Fig. 37).

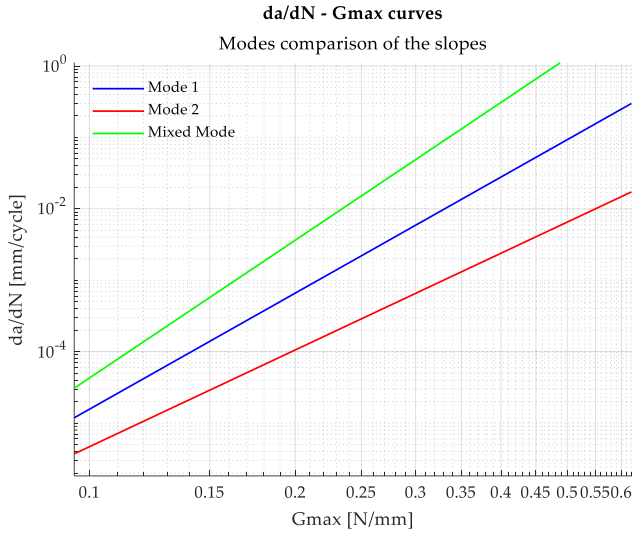

Fig. 37: Propagation rate curve as a function of the maximum SERR.

The slope of the propagation curves increases with the exponent m of the propagation law. In fact, in the logarithmic plane, the following relationship holds:

$$slope = m \qquad \text{Eq. 56}$$

Both Fig. 37 and Eq. 56 suggest that the mixed mode propagation curve is the most steep and that, as a consequence, the corresponding simulations were the most prone to the amplification of the numerical errors effects.

To determine analytically which would be the error Err_{rate} on the propagation rate if the error $Err_{G_{max}}$ is committed in the evaluation of the maximum SERR of a node, the following equation, derived from Eq. 21, can be used:

$$Err_{rate} = Err_{G_{max}}^{m} \qquad \text{Eq. 57}$$

The graphical representation of Eq. 57 is given in Fig. 38a.

For example, if in an iteration the maximum SERR of a node is 30% higher than the actual value, the calculated propagation rate of that node is 3.3, 4.1 or 5.4 times the correct one in case of mode I, mode II or mixed mode, respectively (Fig. 38b).

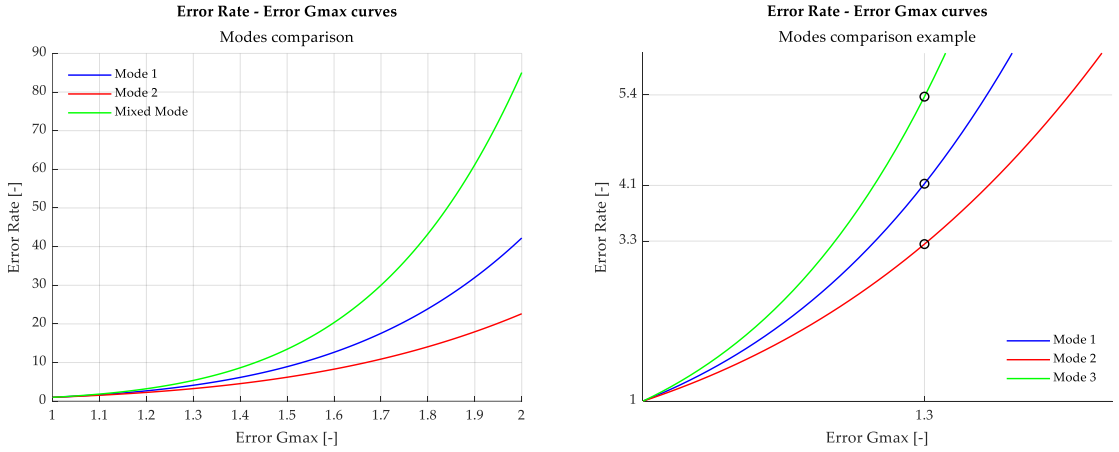

(a) Error curves (b) Error curves example

Fig. 38: (a) Representation of the error on the propagation rate as a function of the error on the maximum SERR; (b) Comparison of the errors on the propagation rate due to a 30% overestimation of the maximum SERR.

Besides, it is also interesting to evaluate which is the maximum SERR value that, according to the propagation law equation (Eq. 21), corresponds to the predicted propagation rate. From now on this quantity will be referred to as the effective maximum SERR, $G_{max}^{(eff)}$. Concerning its physical meaning, it can be considered as the driving SERR for the predicted propagation rate. In fact, if on the delamination front the maximum SERR was uniformly distributed at the effective maximum SERR value, the crack would advance at the predicted velocity. Fig. 39 can help to visualize the concept.

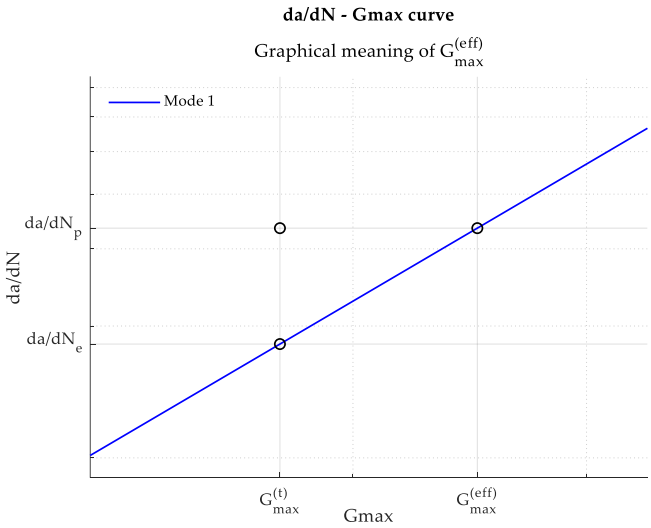

Fig. 39: Graphical meaning of $G_{max}^{(eff)}$.

The effective maximum SERR can be calculated as:

$$G_{max}^{(eff)} = (Err_{rate})^{\frac{1}{m}} * G_{max}^{(t)} \quad \text{Eq. 58}$$

Table 17 allows a comparison among the theoretical maximum SERR $G_{max}^{(t)}$, the maximum of the maximum SERR distribution on a straight front $G_{max}^{(max)}$ and the effective maximum SERR $G_{max}^{(eff)}$ for each simulation.

Table 17: Comparison of $G_{max}^{(eff)}$ with $G_{max}^{(t)}$ and $G_{max}^{(max)}$.

Simulation	*1*	*2*	*3*	*4*	*5*	*6*
$G_{max}^{(eff)}$ $[N/mm]$	0.075	0.170	0.202	0.488	0.070	0.125
$G_{max}^{(t)}$ $[N/mm]$	0.067	0.151	0.201	0.484	0.065	0.116
Percentage difference of $G_{max}^{(eff)}$ *with respect to* $G_{max}^{(t)}$	**+12.0%**	**+12.4%**	**+0.4%**	**+0.9%**	**+7.7%**	**+7.5%**
$G_{max}^{(max)}$ $[N/mm]$	0.074	0.166	0.236	0.566	0.068	0.120
Percentage difference of $G_{max}^{(eff)}$ *with respect to* $G_{max}^{(max)}$	**+1.4%**	**+2.4%**	**-14.4%**	**-13.8%**	**+2.9%**	**+4.2%**

From Table 17 it is possible to note that, in case of mode I, the effective maximum SERR has the highest deviation with respect to the theoretical mean value while, in case of mode II, the two quantities are very close. Moreover, the effective maximum SERR is slightly higher than the maximum of the maximum SERR distribution on the straight front for both mode I and mixed mode. These results confirm that the prediction of the propagation rate was accurate only for the mode II simulations.

To summarize the discussion about the possible causes of disagreement between the expected and the predicted propagation rates and of the differences in terms of accuracy among the three modes, the following considerations can be made:

- The main cause of disagreement between the expected and the predicted propagation rates are identified in the VCCT limitations in calculating reliable SERR values on stepped fronts.

- Depending on the loading mode, the amplitude and the frequency of the numerical errors change. Mode I and mode II are, respectively, the most and least affected loading configurations.
- The steeper is the slope of the propagation curve, the more the effects of the numerical errors are amplified. The mixed mode has the highest sensitivity to them.

According to the previous observations, it is possible to conclude that:

- Mode I is the most subject to numerical errors. In fact, it predicted propagation rates that were nearly 90% higher than the expected ones with effective maximum SERRs 12% higher than the theoretical ones.
- Mode II is the least affected by numerical errors. Even if it happened that the peaks in the maximum SERR distribution were much higher than the average value, in several iterations the peak to average ratio was lower than 1.2. Besides, being its propagation rate curve the not so steep, also the amplification of the numerical errors was less impactful than in the other two cases. As a result, the error in the prediction of the propagation rates was less than 5% and the effective maximum SERRs were close the theoretical ones in both the simulations.
- The mixed mode, in terms of numerical errors, showed a behavior that was in between the ones of the two pure modes, as could be expected. On the other hand, its propagation rate curve is characterized by the highest slope of the three so that, even if the numerical errors were less present than in mode I, they were more amplified. Therefore, the propagation rates were overestimated by about 60% and the effective maximum SERRs were approximately 8% higher than the theoretical ones.

3.1.2. Effect of the implemented cumulative damage law on the performance

The following analysis is about the comparison between the accuracy reached through the implementation of the two different cumulative damage laws presented in section 2.1.

Before discussing the results, it is necessary to highlight that in the present work the propagation length was drastically reduced. In fact, in [1] the delamination was allowed to grow for 30 mm, while in this set of simulations it propagated for 4 mm. In principle, this shouldn't have caused any effect in the evaluation of the propagation rate because it was supposed to be constant thanks to the applied loading conditions. To check whether this was actually the case, the propagation rates, calculated at each row as the ratio between the total delamination length and the number of cycles from

the beginning of the simulation, are plotted as functions of the delamination length itself. However, to better analyze how the propagation rate in correspondence of the single rows is varying, also the points corresponding to the ratio between the mesh size and the number of cycles to release each are plotted. While the propagation rates calculated with the first method can be referred to as “cumulative”, the second ones are defined “local”.

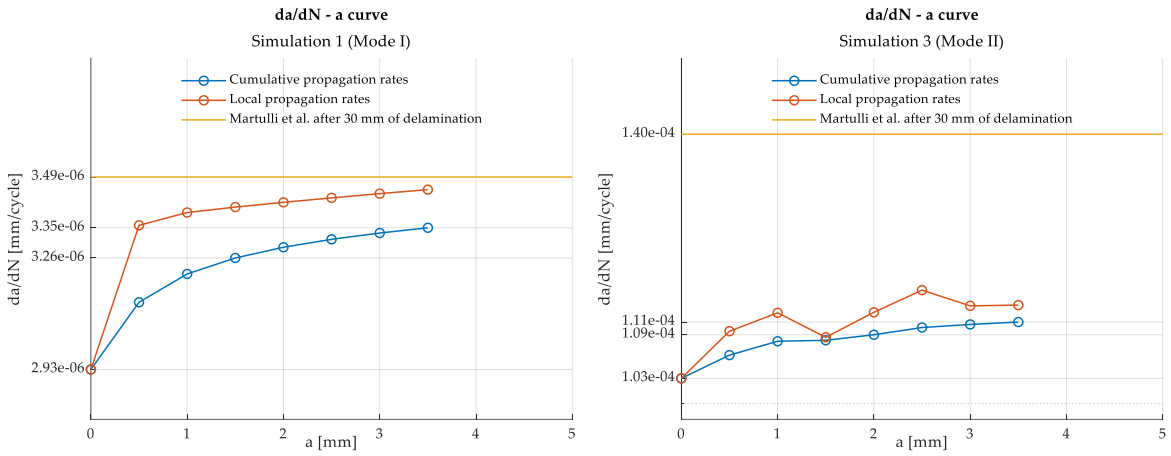

(a) Mode I (b) Mode II

Fig. 40: Dependence of the propagation rate on the delamination length.

From Fig. 40 it can be noted that, for both modes I and II, the propagation rate in the first 0.5 mm of delamination was much lower than the following ones. This is because the initial front needed more cycles to go from straight to curved. In fact, the subsequent straight fronts were assumed to be straight only by the FE software but, actually, their curvature was taken into account by the cumulated damage of the nodes lying on them.

However, some substantial differences between the two modes are present. In fact, the propagation rates at the end of the simulation for modes I and II were, respectively, 95% and 79% of the ones obtained by Martulli and Bernasconi [1]. Moreover, the local propagation rates increased in a monotonic way only in the mode I simulations. A possible reason for this is identified in the slight increase of the maximum SERR on the front during propagation.

In Fig. 41 the relative positions of the predicted propagation rates, corresponding to the two different cumulative damage laws, are represented against the reference Paris curves. By also considering the previous discussion about the dependence of the

propagation rate on the delamination length, it can be concluded that no improvement was reached for mode I, while the prediction for mode II was slightly more accurate. This could be, at least in part, a consequence of the fact that, being mode I more subject to numerical errors, also the impact of the implemented damage law on the overall performance of the algorithm was less significant.

To conclude, the improvements in terms of accuracy in the prediction of the propagation rate of the mixed mode simulations were in between the ones of the two pure modes.

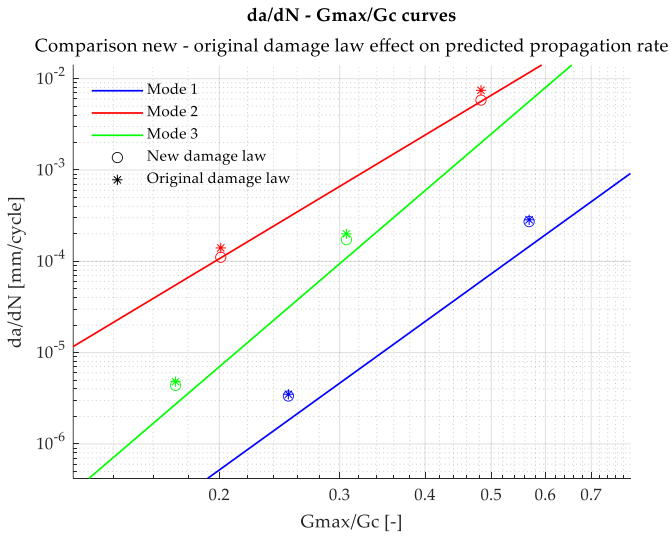

Fig. 41: Comparison of the predicted propagation rates with the original and the new damage laws.

3.2. Case study 2: master propagation curve for mode I fatigue loading of a composite laminate

Contrarily to the previous case study, not only was the laminate modelled with the same geometrical and mechanical characteristics of the real ones, but also the loading conditions were accurately reproduced. Consequently, after an analysis of the SSF performance, also the numerical and experimental results are compared.

3.2.1. Comparison between the first and the second case study

As described in section 2.3, four mode I constant amplitude fatigue loading simulations were carried out at different displacement ratios. The law that was implemented to control the fatigue delamination, already introduced in section 2.3.3, is:

$$\frac{da}{dN} = D\left(\frac{\sqrt{\hat{G}_{I,max}} - \sqrt{\hat{G}_{I,\max}^{(th)}}}{\sqrt{1-\sqrt{\hat{G}_{I,max}}}}\right)^{m} = D(\Delta\bar{K})^{m} \qquad \text{Eq. 29}$$

As done for the first case study, the predictive capabilities of the SSF algorithm are tested by comparing the expected and predicted propagation rates. Under the assumption that the delamination is driven by the mean value of the mode I maximum SERR distribution on the front, the expected propagation rates are calculated by evaluating Eq. 29 in correspondence of that quantity. In displacement control conditions, the SERR decreases as the delamination advances. Therefore, an estimation of the mean value of the numerical mode I maximum SERR distribution, $G_{I,max}^{(num)}$, is performed after each millimeter of propagation in correspondence of the straight fronts (Fig. 42).

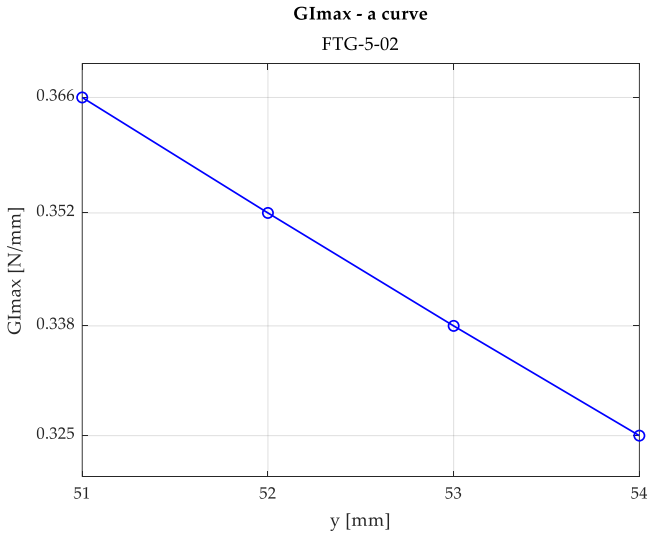

Fig. 42: Dependence of the mean value of the numerical mode I maximum SERR distribution on the delamination length.

In order to evaluate the propagation rate predicted by the SSF algorithm in correspondence of a row, the distance da between two rows, equal to the mesh size, is divided by the number of cycles dN that were necessary to release that row.

The comparison between expected and predicted propagation rates for the specimen FTG-5-02 can be visualized in Fig. 43 and it is quantified in Table 18.

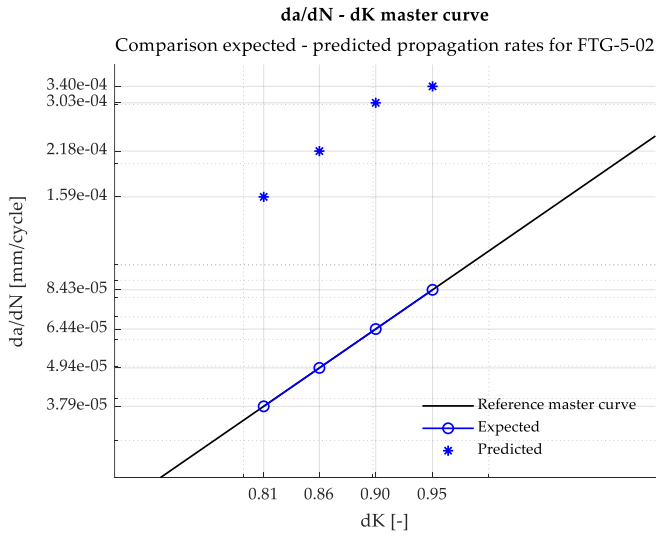

Fig. 43: Comparison between expected and predicted propagation rates for the specimen FTG-5-02.

Table 18: Comparison between expected and predicted propagation rates for the specimen FTG-5-02.

$a\ [mm]$	*51*	*52*	*53*	*54*
$da/dN\ [mm/cycle]$ *Expected*	8.4e-5	6.4e-5	4.9e-5	3.8e-5
$da/dN\ [mm/cycle]$ *Predicted*	3.40e-4	3.03e-4	2.18e-4	1.59e-4
Percentage of overestimation	**+303%**	**+371%**	**+341%**	**+320%**

From Table 18, it is possible to note that the predicted propagation rates were about four times the expected ones, while the overpredictions in the first case study for the same loading mode were less than 90%. In that case, the disagreement with the expected propagation rates was explained by the presence of peaks in the maximum SERR distribution along the curved fronts. Due to the much worse accuracy, here it is considered the possibility that numerical errors occurred also in the maximum SERR distribution along the straight fronts.

By observing Fig. 44, it is visible a drop in the mode I maximum SERR distribution in correspondence of the nodes at the extremities; in that location, the mode I SERR value is about ten times lower than the one in the adjacent nodes.

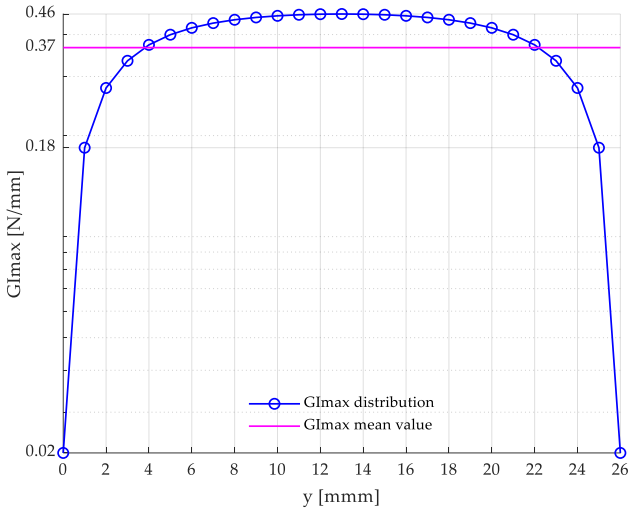

Fig. 44: Mode I maximum SERR distribution on the initial straight front for the specimen FTG-5-02.

It was noted that, in correspondence of the lateral nodes, the mode mixity changed during the release of a row. At the beginning, when the front was straight, the mode

mixity was 0.4, while at the end, when the same nodes were the last remaining ones, it was 0.04. In fact, on the straight fronts, part of the energy that should have belonged to mode I was converted in mode III SERR peaks. As a consequence, the driving SERR of the expected propagation rates, calculated as the mean value of the mode I maximum SERR distribution on the straight front, result to be underestimated. The final cause is an increase of the discrepancy with the predicted propagation rates.

The driving SERR of the expected propagation rates is now estimated by means of the compliance method (A.3). The comparison between the SERR values obtained by averaging the numerical distribution, $G_{I,max}^{(num)}$, and by applying the compliance method, $G_{I,max}^{(compl)}$, is represented in Fig. 45 and quantified in Table 19.

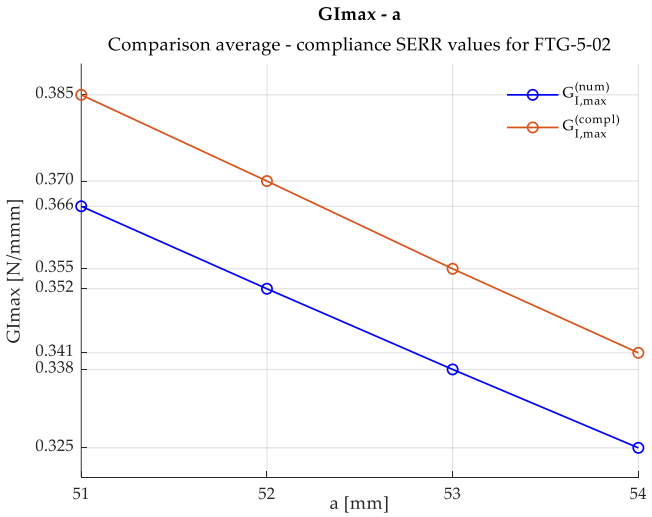

Fig. 45: Comparison between the mode I maximum SERR values obtained by averaging the numerical distribution and by applying the compliance method for the specimen FTG-5-02.

Table 19: Comparison between $G_{I,max}^{(num)}$ and $G_{I,max}^{(compl)}$ for the specimen FTG-5-02.

$a\ [mm]$	*51*	*52*	*53*	*54*
$G_{I,max}^{(num)}\ [N/mm]$	0.366	0.352	0.338	0.325
$G_{I,max}^{(compl)}\ [N/mm]$	0.385	0.370	0.355	0.341
Percentage difference	**+5.2%**	**+5.2%**	**+5.0%**	**+5.0%**

It can be noted that the maximum SERR estimated through the compliance method is about 5% higher than the numerical one during all the propagation. At this point, it

could be interesting to evaluate how would change the error in the prediction of the propagation rates if the expected ones are calculated in correspondence of $G_{I,max}^{(compl)}$.

Table 20: Comparison between expected and predicted propagation rates for the specimen FTG-5-02 in case the mode I maximum SERR is calculated through the compliance method.

$a\ [mm]$	*51*	*52*	*53*	*54*
$da/dN\ [mm/cycle]$ *Expected*	1.21e-4	9.2e-5	6.9e-5	5.2e-5
$da/dN\ [mm/cycle]$ *Predicted*	3.40e-4	3.03e-4	2.18e-4	1.59e-4
Percentage of overestimation	***+182%***	***+232%***	***+217%***	***+205%***

From Table 20 it can be observed that also a small increase in the SERR values (+5%) has a huge impact on the expected propagation rates: in fact, the overestimation decreases from about +300% to +200%. This means that the adopted propagation law is very sensitive to small changes in the SERR values. Therefore, it is possible that the errors on the prediction of the propagation rates in the simulation under analysis were more amplified than in the ones of the first case study due to a steeper propagation rate curve. For this reason, a graphical comparison is performed in Fig. 46.

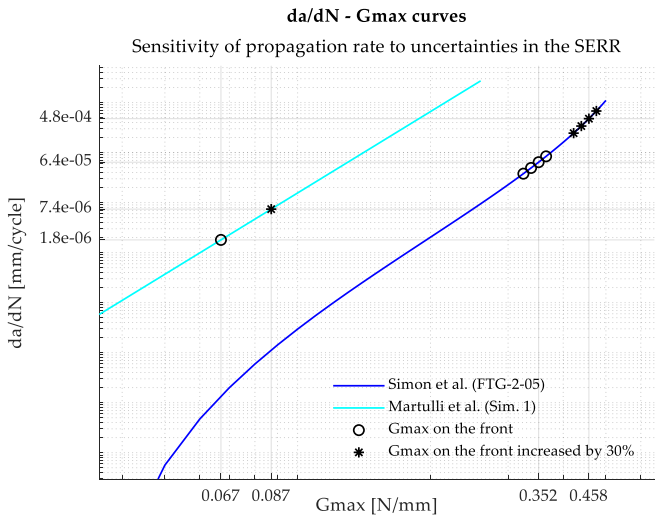

Fig. 46: Comparison between the slopes of the propagation rate curve of the specimen FTG-2-05 and the Simulation 1 of the first case study.

From Fig. 46 it is possible to note that the slope of the propagation curve for the specimen FTG-5-02 is higher and that, therefore, same variations in the maximum SERR have a bigger impact on the propagation rate (Eq. 57).

For example, if the error on the SERR estimation of a node consists in a 30% increase with respect to the actual value, the error on the propagation rate of the same node ranges between +550% and +700% for the specimen FTG-5-02, while it is about +300% for the Simulation 1 of the first case study. It is necessary to highlight that, since the slope of the propagation rate curve of the specimen FTG-5-02 is not constant, the same error on different SERRs causes different errors on the propagation rate. For this reason, the four $G_{I,max}^{(num)}$ values previously calculated where used as reference just to have an idea of the errors that could be committed on the propagation rates (Table 21).

Table 21: Errors in the propagation rate in correspondence of a 30% overestimation of the SERR for the specimen FTG-5-02.

$a\ [mm]$	*51*	*52*	*53*	*54*
$da/dN\ \ [mm/cycle]$ *in correspondence of* $G_{I,max}^{(num)}$	8.4e-5	6.4e-5	4.9e-5	3.8e-5
$da/dN\ \ [mm/cycle]$ *in correspondence of* $1.3G_{I,max}^{(num)}$	6.80e-4	4.77 e-4	3.40 e-4	2.45 e-4
Overestimation of the propagation rate	**+700%**	**+645%**	**+594%**	**+545%**

A final consideration concerns the identification of the effective mode I maximum SERRs $G_{I,max}^{(eff)}$, the meaning of which was introduced in section 3.1.1 and represented in Fig. 39. They can be compared to the mean and maximum values of the mode I maximum SERR distributions on each straight front during propagation.

Table 22: Comparison of $G_{I,max}^{(eff)}$ with $G_{I,max}^{(num)}$, $G_{I,max}^{(compl)}$ and $G_{I,max}^{(max)}$.

$a\ [mm]$	*51*	*52*	*53*	*54*
$G_{I,max}^{(eff)}\ [N/mm]$	0.440	0.434	0.416	0.400
$G_{I,max}^{(num)}\ [N/mm]$	0.366	0.352	0.338	0.325
Percentage difference of $G_{I,max}^{(eff)}$ *with respect to* $G_{I,max}^{(num)}$	**+20%**	**+23%**	**+23%**	**+23%**
$G_{I,max}^{(compl)}\ [N/mm]$	0.385	0.370	0.355	0.341
Percentage difference of $G_{I,max}^{(eff)}$ *with respect to* $G_{I,max}^{(compl)}$	**+14%**	**+17%**	**+17%**	**+17%**
$G_{I,max}^{(max)}$	0.461	0.444	0.427	0.411
Percentage ratio between $G_{I,max}^{(eff)}$ *and* $G_{I,max}^{(max)}$	**95%**	**98%**	**97%**	**97%**

It can be observed that the effective mode I maximum SERRs are about 20-25% higher than the mean value of the numerical SERR distribution, 14-17% higher than the SERR calculated through the compliance method and about equal to 97% of the maximum value. Since all the iterations, apart from the first and the last ones, for the release of a row were characterized by static debonding of the nodes, it is not a surprise to find that the effective maximum SERRs are close to the maximum of each distribution. This means that, due to the numerical errors, the SSF algorithm predicted propagation rates nearly as if the SERR on the front were uniformly distributed at a level close to the maximum value of the SERR distribution on the straight front. In other words, as observed for the mode I simulations of the first case study, the predicted propagation rates were not driven by the mean value of the SERR distributions but by the maximum one.

The comparison between the simulation performed on the specimen FTG-5-02 and the Simulation 1 of the first case study can be summarized in the following points:

- The overestimation of the predicted propagation rates for the specimen FTG-5-02 was in the order of +300%, while the one in the first case study was less than +90%. The reasons at the basis of this difference are identified in the underestimation of the mode I mean SERR value due to the presence of mode III SERR peaks in the

lateral nodes and in the higher amplification of the errors due to a steeper propagation curve in the specimen FTG-5-02.

- In both the cases, the effective maximum SERR, that can be considered as the driving SERR for the predicted propagation rates, is closer to the maximum value of the maximum SERR distributions on the straight fronts than to the mean one.

3.2.2. Dependence of the SSF algorithm performance on the load ratio

The specimens used for the four simulations are reported in Table 23 along with the respective load ratio R, threshold mode I maximum SERR $G_{I,max}^{(th)}$ and critical mode I SERR $G_{I,c}$.

Table 23: Fatigue constants for each specimen.

Specimen	*FTG-5-02*	*FTG-5-03*	*FTG-5-07*	*FTG-5-05*
R [-]	0.1	0.33	0.5	0.75
$G_{I,max}^{(th)}$ $[N/mm]$	0.032	0.058	0.104	0.415
$G_{I,c}$ $[N/mm]$	0.711	0.711	0.711	0.711

In order to compare the performance of the four simulations, the accuracy in the prediction of the propagation rates is evaluated at the second row of each specimen. In Table 24, expected and predicted propagation rates are compared. To be noted that the expected ones are calculated in correspondence of the mean value of the mode I maximum SERR distribution on the straight fronts, $G_{I,max}^{(num)}$.

Table 24: Comparison between expected and the predicted propagation rates.

Specimen	*FTG-5-02*	*FTG-5-03*	*FTG-5-07*	*FTG-5-05*
$G_{max}^{(num)}$ $[N/mm]$	0.352	0.356	0.377	0.487
da/dN $[mm/cycle]$ *Expected*	6.44e-5	3.06e-5	1.30e-5	6.52e-9
da/dN $[mm/cycle]$ *Predicted*	3.03e-4	1.68e.4	9.96e-5	1.02e-5
Overestimation of the propagation rate in correspondence of $G_{max}^{(num)}$	**+371%**	**+449%**	**+669%**	**+156,300%**

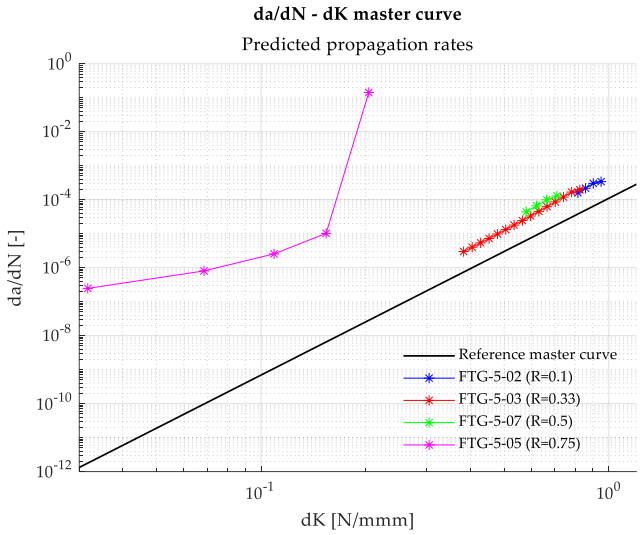

Fig. 47: Predicted propagation rates with respect to the reference master curve.

By increasing the load ratio, the points corresponding to the predicted propagation rates tend to move away from the propagation master curve, indicating that the accuracy decreases (Fig. 47). In particular, the simulation carried out at the load ratio of 0.75 predicted a propagation rate 14,000,000 higher than the expected one after a delamination of 4 mm. Besides, the debonding of the first row of the same specimen, represented by the pink point on the right, was completely static, so that the overprediction was even higher.

In the previous section it was observed that numerical errors in the SERR distribution occurred along both the straight and the curved fronts. In particular, the ones along the straight fronts caused an underestimation of the mean value of the mode I SERR

distribution, and, as a consequence, of the corresponding expected propagation rate, while the ones along the curved fronts consisted in peaks in the mode I SERR distribution that led to an overestimation of the predicted propagation rates, mostly related to the static release of the nodes.

To check whether the lateral mode III peaks in the SERR distribution on the straight fronts have had the same impact in all the simulations, the mode I maximum SERRs calculated through the compliance method $G_{I,max}^{(compl)}$ (A.3) are compared with the numerical average of the corresponding distributions $G_{I,max}^{(num)}$ (Table 25).

Table 25: Percentage difference between $G_{I,max}^{(compl)}$.and $G_{I,max}^{(num)}$ and overestimation of the propagation rates in correspondence of $G_{I,max}^{(compl)}$.

Specimen	*FTG-5-02*	*FTG-5-03*	*FTG-5-07*	*FTG-5-05*
$G_{I,max}^{(compl)}$ $[N/mm]$	0.371	0.376	0.396	0.512
Percentage difference of $G_{I,max}^{(compl)}$ *with respect to* $G_{I,max}^{(num)}$	**+5.2%**	**+5.5%**	**+5.0%**	**+5.1%**
Overestimation of the propagation rate in correspondence of $G_{max}^{(compl)}$	**+232%**	**+264%**	**+394%**	**+26,000%**

From Table 25 it is possible to note that, in all the cases, the difference between the two SERR values is about 5%. However, even if the error in the prediction of the propagation rates has decreased, the degradation of the accuracy at high load ratio levels is still present.

In the previous sections (3.1.1, 3.2.1) it was observed how relevant is the influence of the sensitivity of the propagation rate to small variations in the SERR values. In fact, the steeper the propagation rate curve, the higher is the amplification of the errors in the SERR estimation. Therefore, to evaluate if this has a role on the load ratio effect on the performance, the propagation rate curves were plotted as functions of the mode I maximum SERR (Fig. 48).

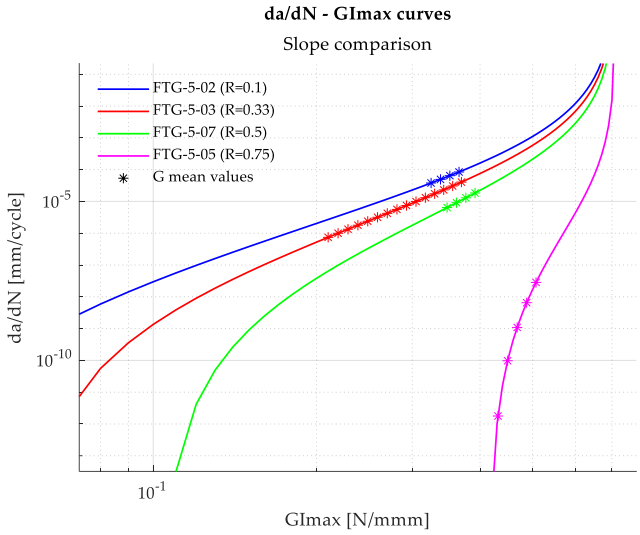

Fig. 48: Propagation rate curves as functions of the mode I maximum SERR.

By increasing the load ratio, the slope of the propagation rate curve increases, as it was observed in section 1.2.1. In particular, in case of a load ratio equal to 0.75 (specimen FTG-5-05), the curve is nearly vertical. These considerations give reason to the fact that the same numerical errors in the estimation of the mode I maximum SERR, both in terms of underestimation of the mean value in the straight fronts and of SERR peaks in the stepped ones, are much more detrimental at high load ratios.

To quantify the previous observations, in Table 26 are reported the errors in the propagation rate in correspondence of an overestimation of 30% of the mode I maximum SERR. As reference, the mean SERR values $G_{I,max}^{(num)}$ at 1 mm of propagation are used.

Table 26: Estimation of the errors in the propagation rate in correspondence of a 30% overestimation of the mean SERR at 1 mm of propagation.

Specimen	*FTG-5-02*	*FTG-5-03*	*FTG-5-07*	*FTG-5-05*
da/dN $[mm/cycle]$ *in correspondence of* $G_{I,max}^{(num)}$	6.4e-5	3.1e-5	1.3e-5	6.5e-9
da/dN $[mm/cycle]$ *in correspondence of* $1.3G_{I,max}^{(num)}$	4.77 e-4	2.69e-4	1.69e-4	2.65 e-5
Error in the propagation rate	**+645%**	**+768%**	**+1200%**	**+407,500%**

Finally, the effective mode I maximum SERR values are calculated (Table 27). The observations concerning the comparison between this quantity and the mean and maximum values of the SERR distribution are aligned with the ones already presented in sections 3.1.1 and 3.2.1.

Table 27: Comparison of $G_{max}^{(eff)}$ with $G_{max}^{(num)}$, $G_{max}^{(compl)}$ and $G_{max}^{(max)}$.

Specimen	*FTG-5-02*	*FTG-5-03*	*FTG-5-07*	*FTG-5-05*
$G_{I,max}^{(eff)}$ $[N/mm]$	0.434	0.440	0.466	0.616
$G_{I,max}^{(num)}$ $[N/mm]$	0.352	0.356	0.377	0.487
Percentage difference of $G_{I,max}^{(eff)}$ *with respect to* $G_{I,max}^{(num)}$	**+23%**	**+23%**	**+24%**	**+26%**
$G_{max}^{(compl)}$ $[N/mm]$	0.371	0.376	0.396	0.512
Percentage difference of $G_{I,max}^{(eff)}$ *with respect to* $G_{max}^{(compl)}$	**+17%**	**+17%**	**+18%**	**+20%**
$G_{I,max}^{(max)}$	0.444	0.448	0.475	0.616
Percentage ratio between $G_{I,max}^{(eff)}$ *and* $G_{I,max}^{(max)}$	**95%**	**98%**	**98%**	**100%**

The discussion about the load ratio effect on the accuracy of the prediction of the propagation rates can be summarized in the following considerations:

- Since the geometry and the loading conditions of the specimens were very similar within the FE software, also the type of numerical errors was the same independently from the load ratio.
- By increasing the load ratio, the slope of the propagation curve becomes steeper so that the sensitivity to the errors in the evaluation of the SERR increases. This is identified as the main cause of the deterioration of the performance at high load ratios.
- Independently from the load ratio, the driving SERR of the predicted propagation rates is closer to the maximum value of the distribution than to the mean one. This is related to the fact that the majority of the iterations are characterized by a static release of the nodes caused by the peaks in the mode I maximum SERR distribution on the stepped fronts.

3.2.3. Comparison between numerical simulation and experimental tests results

In order to estimate how close the simulation results were to the experimental ones, the most immediate procedure would consist in comparing the delamination length - number of cycles curves.

In the paper published by Simon et al. [13] these diagrams are absent but, on the other hand, the information concerning the final delamination length and the total number of cycles is provided. However, a proper comparison is possible only for two specimens (FTG-5-03, FTG-5-05) out of four because the simulations corresponding to the other two specimens aborted before reaching the prescribed delamination length. Since the propagation rate was overestimated by the SSF algorithm, as discussed in sections 3.2.1 and 3.2.2, it is expected that the total number of cycles was lower than the real one. In Table 28, a_i refers to the initial delamination length while a_f to the final one.

Table 28: Comparison between experimental / numerical propagation length and number of cycles.

Specimen	a_i *[mm]*	*Propagation [mm]*	a_f *[mm]*	N_{tot} *[cycles]*	*Experimental/Numerical*
FTG-5-02	51.1	17.3	68.4	1,770,600	*Experimental*
	51.0	4.0	55.0	17,107	*Numerical*
FTG-5-03	49.2	15.2	64.4	2,581,500	*Experimental*
	49.0	15.0	64.0	1,282,761	*Numerical*
FTG-5-07	51.1	13.3	64.4	2,870,000	*Experimental*
	51.0	4.0	55.0	55,594	*Numerical*
FTG-5-05	53.9	6.1	60.0	954,900	*Experimental*
	54.0	6.0	60.0	19,822,725	*Numerical*

Concerning the specimen FTG-5-03, the number of cycles predicted by the simulations were about half the ones of the experimental tests. To check if the incongruence is only an effect of the numerical errors in the SERR distribution, it is possible to estimate which would be the "theoretical" number of cycles needed to reach the same propagation length. To determine this quantity, the interpolation of the SERR values obtained through the compliance method is used to identify the dependence of the mode I maximum SERR on the delamination length. Then, the overall propagation length is discretized in 0.01 mm long segments in which the SERR and the propagation rate, calculated through the propagation law equation (Eq. 29), are assumed to be constant.

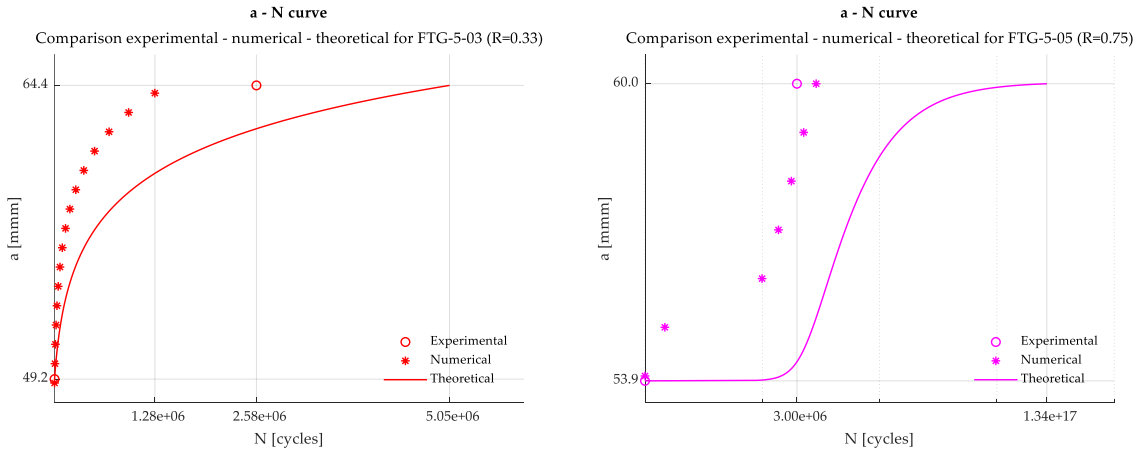

(a) FTG-5-03 (b) FTG-5-05

Fig. 49: $a - N$ curve: comparison among experimental, numerical and theoretical results.

In Fig. 49a it can be noted that the theoretical number of cycles are about two times the ones obtained experimentally, meaning that the SERR in the simulation was lower during the advancement of the delamination front. This disagreement could be caused by:

- Numerical errors in the evaluation of force and displacement used to calculate the compliance necessary to define the SERR dependence on the delamination length.
- Wrong evaluation of the mode I maximum SERR during the experimental propagation.
- Incorrect reproduction of the experimental specimen and of the loading conditions in the FE software.

If force and displacement are affected by numerical errors, then also the estimation of the compliance is not reliable. Therefore, in correspondence of the same delamination

length, the values of the mode I maximum SERR, and, as a consequence, of the propagation rate, are different from the ones in the experimental test.
Similarly, some errors could have been committed in the evaluation of the mode I maximum SERR during the experimental test. In this case, the fitted propagation law would be wrong.
Finally, as discussed in A.2, by comparing the numerical and experimental load – displacement curves for the FTG-5-05 specimen, a lower value of compliance was highlighted in the numerical model. Consequently, a spring of 12 N/mm was attached to the tip of the laminate model to increase its value up to the correct one. Nevertheless, different issues are connected to this procedure:

- The fact itself that the compliance of the numerical model was lower than the one of the specimen is symptom of some intrinsic inconsistency between the simulation and the experimental test. In fact, the required spring has a stiffness much lower than the one that would have been necessary to take into account the non-infinite rigidity of the loading machine.
- The spring stiffness was calculated for the specimen FTG-5-05 since its load – displacement curve was the only one to be provided. Due to not identical geometrical dimensions, it is possible that the other specimen would have required a different value of spring stiffness.
- Being the spring stiffness low and the total applied displacement constant, the effective opening displacement of the laminate tips was slightly increasing during propagation. The proof of this is provided in A.2.
- It is not possible to check how the compliance of the experimental specimen is changing during the propagation and, consequently, which is the actual SERR value on the front at a specific delamination length.

From the observations above, it can be understood that there are many variables that could have contributed to the disagreement between the experimental and the theoretical-numerical results.

The output concerning the specimen FTG-5-05 is more critical. In fact, even if the propagation rate was highly overestimated, the number of cycles predicted by the simulation were about 20 times the experimental ones.

Besides, Fig. 49b shows that the theoretical number of cycles are a hundred billion times higher than the cycles reached in the test. This is a clear proof that, as in the previous specimen, the values of SERR calculated through the compliance are lower than the experimental ones. In particular, at the end of the simulation, the SERR values were approximately equal to the threshold maximum SERR (Table 23) and the propagation rates in the order of 1e-19 mm/cycle.

However, it should be noted that the propagation rate curve used to calculate the theoretical number of cycles, that is the one implemented in the SSF algorithm as well, is independent from the propagation length, while the one fitted by Simon et al. [13]

on the experimental data considers the monotonic increase of the critical SERR in the first 10 mm of propagation. If this dependence had been considered, the estimated propagation rates would have been higher and the overall number of cycles lower, so that a closer value to the experimental one would have been obtained.

In the following lines, the most relevant considerations of this section are summed:

- A disagreement among experimental, numerical and theoretical results was observed.
- The numerical results shouldn't be considered reliable due to the huge impact of numerical errors.
- The disagreement between the experimental and the theoretical number of cycles was caused by the fact that, in correspondence of the same delamination length, the estimated SERR value was different. In particular, the experimental SERRs were higher than the ones calculated through the compliance method. The reasons of the incongruence were related to possible numerical errors in the estimation of the SERR through the compliance method, implementation of a wrong propagation rate law due to incorrect evaluation of the SERR during the experimental tests, inconsistent numerical model and implementation of a simplified propagation law.

4 Conclusion and future developments

The aim of the present work was to test the capabilities of the SSF algorithm to predict the fatigue delamination of composites and, in particular, to determine how its performance vary depending on mode mixity and load ratio.

Since the fatigue simulations were carried out on simple composite laminates, it was possible to estimate the expected propagation rates. For this purpose, the propagation law equation was evaluated in correspondence of the mean value of the SERR distribution on the front, assumed to be the driving SERR of the delamination rate. This value was calculated or analytically or through the average of the numerical SERR distribution or by means of the compliance method according to the data available in the different case studies.

In all the simulations the algorithm overestimated the propagation rates. The main cause of inaccuracy was identified in the numerical errors introduced by the VCCT while calculating the SERR values on stepped fronts. In fact, since the actual delamination front is curved and the adopted mesh is regular, the resulting front profile is stepped. The discontinuities behave like stress risers causing peaks in the SERR distribution and the consequent underestimation of the number of cycles needed to release the affected nodes. Besides, if the applied load is sufficiently high, the SERR peaks exceed the 90% of the fracture toughness and a static release of the nodes takes place so that the introduced error is even higher.

Given the presence of numerical errors on the evaluation of the SERR, a factor able to amplify their impact is the steepness of the propagation rate curve: larger the slope, higher the errors in the estimation of the propagation rate of the single nodes and, consequently, of the number of cycles necessary to release them.

The simulations carried out on the HTA/6376C laminate have shown a strong dependence of the accuracy on the loading mode. The combined effect of severe SERR peaks and of a steep Paris curve has made the mode I simulations the least accurate ones. Conversely, the predicted propagation rates were close to the expected ones in the mode II simulations. In fact, not only they were less affected by SERR peaks but also less sensitive to them. Finally, the profiles of the SERR distributions under mixed mode loading conditions were similar to the ones observed under mode I but the peaks

were less pronounced thanks to the co-presence of mode II. However, being the slope of the corresponding propagation rate curve the highest of the three, the effects of the errors in the SERR estimation were more amplified. Therefore, the mixed mode simulations performed slightly better than the mode I ones.

On the other hand, the simulations on the G0814/913 laminate have demonstrated that the performance of the SSF algorithm is influenced by the load ratio too. Since in the FE software the four simulations were performed on specimen with nearly identical dimensions and similar applied displacements, the type of numerical errors occurred in the SERR distribution were the same. As a result, the discriminant in the very different performance was the sensitivity of the propagation rates to the errors in the SERR distribution. By increasing the load ratio, the slope of the propagation curves, expressed as functions of the maximum SERR, increases: this is the reason why the accuracy degraded passing from 0.1 to 0.75 load ratio.

On the basis of the above considerations, it is possible to conclude that the dependence of the performance on mode mixity and load ratio is strictly related to the presence of numerical errors and that, therefore, the next step to validate the predictive capabilities of the SSF algorithm on real and more complex structures is the management of such errors.

A possible strategy to make the extracted SERR values closer to the actual ones is already in phase of development. The idea consists in smoothing the mesh on the delamination front after each iteration in order to approximate the actual front and to avoid the presence of numerical errors in the SERR distribution. At the expense of an increase in the computational time, the accuracy and reliability would be higher and the SSF algorithm could become a concrete and powerful tool to predict the fatigue delamination of composites.

Bibliography

[1] L. M. Martulli and A. Bernasconi, "An efficient and versatile use of the VCCT for composites delamination growth under fatigue loadings in 3D numerical analysis: the Sequential Static Fatigue algorithm," *Int J Fatigue*, vol. 170, p. 107493, May 2023, doi: 10.1016/J.IJFATIGUE.2022.107493.

[2] M. L. M. Bernasconi Andrea, "Material of the course 'Ligthweight Design of Mechanical Structures.'"

[3] L. Yao, R. Alderliesten, M. Zhao, and R. Benedictus, "Bridging effect on mode I fatigue delamination behavior in composite laminates," *Compos Part A Appl Sci Manuf*, vol. 63, pp. 103–109, Aug. 2014, doi: 10.1016/J.COMPOSITESA.2014.04.007.

[4] Srinivasan Sridharan, *Delamination Behaviour of Composites*. 2008.

[5] A. C. ; C. Fisher, *Introduction to Contact Mechanics*. 2007.

[6] Y. Qiao, Z.-X. Zhang, and S. Zhang, "An Experimental Study of the Relation between Mode I Fracture Toughness, KIc, and Critical Energy Release Rate, GIc," *Materials*, vol. 16, no. 3, p. 1056, Jan. 2023, doi: 10.3390/ma16031056.

[7] Chun Hui Wang, "Introduction to Fracture Mechanics," 1996.

[8] H. Moustabchir, J. Arbaoui, A. Zitouni, S. Hariri, and I. Dmytrakh, "Numerical analysis of stress intensity factor and T-stress in pipeline of steel P264GH submitted to loading conditions," *Journal of Theoretical and Applied Mechanics*, p. 665, Jul. 2015, doi: 10.15632/jtam-pl.53.3.665.

[9] C. Hui, C. Chen, X. Legrand, and P. Wang, "Investigation of the Interlaminar Shear Performance of Tufted Preforms and Composites under Mode II Loading Condition," *Polymers (Basel)*, vol. 14, no. 4, p. 690, Feb. 2022, doi: 10.3390/polym14040690.

[10] E. Armanios, R. Bucinell, D. Wilson, L. Asp, A. Sjögren, and E. Greenhalgh, "Delamination Growth and Thresholds in a Carbon/Epoxy Composite Under Fatigue Loading," *Journal of Composites Technology and Research*, vol. 23, no. 2, p. 55, 2001, doi: 10.1520/CTR10914J.

[11] W. Johnson, J. Masters, D. Wilson, M. Juntti, L. Asp, and R. Olsson, "Assessment of Evaluation Methods for the Mixed-Mode Bending Test," *Journal of Composites Technology and Research*, vol. 21, no. 1, p. 37, 1999, doi: 10.1520/CTR10611J.

[12] P. Robinson, U. Galvanetto, D. Tumino, G. Bellucci, and D. Violeau, "Numerical simulation of fatigue-driven delamination using interface elements," *Int J Numer Methods Eng*, vol. 63, no. 13, pp. 1824–1848, Aug. 2005, doi: 10.1002/nme.1338.

[13] I. Simon, L. Banks-Sills, and V. Fourman, "Mode I delamination propagation and R-ratio effects in woven composite DCB specimens for a multi-directional layup," *Int J Fatigue*, vol. 96, pp. 237–251, Mar. 2017, doi: 10.1016/J.IJFATIGUE.2016.12.005.

[14] T. M. Roberts and M. Talebzadeh, "Acoustic emission monitoring of fatigue crack propagation," *J Constr Steel Res*, vol. 59, no. 6, pp. 695–712, Jun. 2003, doi: 10.1016/S0143-974X(02)00064-0.

[15] H. Ewalds, F. van Doorn, and W. Sloof, "Influence of Environment and Specimen Thickness on Fatigue Crack Growth Data Correlation by Means of Elber-Type Equations," in *Corrosion Fatigue: Mechanics, Metallurgy, Electrochemistry, and Engineering*, ASTM International100 Barr Harbor Drive, PO Box C700, West Conshohocken, PA 19428-2959, 1983, pp. 115–134. doi: 10.1520/STP44809S.

[16] M. J. Donough, "Load Ratio Effects in the Fatigue Crack Propagation of Composite Laminates and Bonded Joints," 2014.

[17] G. Androuin, L. Michel, I. Maillet, and X. Gong, "Characterization of fatigue delamination growth under mode I and II: Effects of load ratio and load history," *Eng Fract Mech*, vol. 203, pp. 172–185, Nov. 2018, doi: 10.1016/j.engfracmech.2018.06.030.

[18] S. Matsuda, M. Hojo, and S. Ochiai, "Mesoscopic Fracture Mechanism of Mode II Delamination Fatigue Crack Propagation in Interlayer-Toughened CFRP.," *JSME International Journal Series A*, vol. 40, no. 4, pp. 423–429, 1997, doi: 10.1299/jsmea.40.423.

[19] G. Matsubara, H. Ono, and K. Tanaka, "Mode II fatigue crack growth from delamination in unidirectional tape and satin-woven fabric laminates of high strength GFRP," *Int J Fatigue*, vol. 28, no. 10, pp. 1177–1186, Oct. 2006, doi: 10.1016/J.IJFATIGUE.2006.02.006.

[20] G. Allegri, M. I. Jones, M. R. Wisnom, and S. R. Hallett, "A new semi-empirical model for stress ratio effect on mode II fatigue delamination growth," *Compos Part A Appl Sci Manuf*, vol. 42, no. 7, pp. 733–740, Jul. 2011, doi: 10.1016/J.COMPOSITESA.2011.02.013.

[21] C. Bathias and A. Laksimi, "Delamination Threshold and Loading Effect in Fiber Glass Epoxy Composite," in *Delamination and Debonding of Materials*, ASTM International100 Barr Harbor Drive, PO Box C700, West Conshohocken, PA 19428-2959, 1985, pp. 217–237. doi: 10.1520/STP36307S.

[22] R. ; R. ; B. R. Khan, "EFFECT OF STRESS RATIO ON DELAMINATION GROWTH BEHAVIOR IN UNIDIRECTIONAL CARBON/EPOXY UNDER MODE I FATIGUE LOADING ," 2009.

[23] C. A. R. Rans, "Formulating an effective strain energy release rate for a linear elastic fracture mechanics description of delamination growth," 2009.

[24] C. Rans, R. Alderliesten, and R. Benedictus, "Misinterpreting the results: How similitude can improve our understanding of fatigue delamination growth," *Compos Sci Technol*, vol. 71, no. 2, pp. 230–238, Jan. 2011, doi: 10.1016/J.COMPSCITECH.2010.11.010.

[25] A. Russell and K. Street, "The Effect of Matrix Toughness on Delamination: Static and Fatigue Fracture Under Mode II Shear Loading of Graphite Fiber Composites," in *Toughened Composites*, 100 Barr Harbor Drive, PO Box C700, West Conshohocken, PA 19428-2959: ASTM International, 1987, pp. 275-275–20. doi: 10.1520/STP24383S.

[26] K. Tanaka and H. Tanaka, "Stress-Ratio Effect on Mode II Propagation of Interlaminar Fatigue Cracks in Graphite/Epoxy Composites," in *Composite Materials: Fatigue and Fracture (Sixth Volume)*, 100 Barr Harbor Drive, PO Box C700, West Conshohocken, PA 19428-2959: ASTM International, pp. 126-126–17. doi: 10.1520/STP19925S.

[27] J. Andersons, "Empirical model for stress ratio effect on fatigue delamination growth rate in composite laminates," *Int J Fatigue*, vol. 26, no. 6, pp. 597–604, Jun. 2004, doi: 10.1016/j.ijfatigue.2003.10.016.

[28] R. Jones, S. Pitt, A. J. Bunner, and D. Hui, "Application of the Hartman–Schijve equation to represent Mode I and Mode II fatigue delamination growth in composites," *Compos Struct*, vol. 94, no. 4, pp. 1343–1351, Mar. 2012, doi: 10.1016/j.compstruct.2011.11.030.

[29] R. Jones, A. J. Kinloch, and W. Hu, "Cyclic-fatigue crack growth in composite and adhesively-bonded structures: The FAA slow crack growth approach to certification and the problem of similitude," *Int J Fatigue*, vol. 88, pp. 10–18, Jul. 2016, doi: 10.1016/J.IJFATIGUE.2016.03.008.

[30] R. Jones, W. Hu, and A. J. Kinloch, "A convenient way to represent fatigue crack growth in structural adhesives," *Fatigue Fract Eng Mater Struct*, vol. 38, no. 4, pp. 379–391, Apr. 2015, doi: 10.1111/ffe.12241.

[31] R. Jones, S. Stelzer, and A. J. Brunner, "Mode I, II and Mixed Mode I/II delamination growth in composites," *Compos Struct*, vol. 110, no. 1, pp. 317–324, Apr. 2014, doi: 10.1016/J.COMPSTRUCT.2013.12.009.

[32] A. Hartman and J. Schijve, "The effects of environment and load frequency on the crack propagation law for macro fatigue crack growth in aluminium alloys,"

Eng Fract Mech, vol. 1, no. 4, pp. 615–631, Apr. 1970, doi: 10.1016/0013-7944(70)90003-2.

[33] L. Yao, R. C. Alderliesten, M. Zhao, and R. Benedictus, "Discussion on the use of the strain energy release rate for fatigue delamination characterization," *Compos Part A Appl Sci Manuf*, vol. 66, pp. 65–72, Nov. 2014, doi: 10.1016/J.COMPOSITESA.2014.06.018.

[34] L. Amaral, L. Yao, R. Alderliesten, and R. Benedictus, "The relation between the strain energy release in fatigue and quasi-static crack growth," *Eng Fract Mech*, vol. 145, pp. 86–97, Aug. 2015, doi: 10.1016/J.ENGFRACMECH.2015.07.018.

[35] W. Elber, "The Significance of Fatigue Crack Closure," in *Damage Tolerance in Aircraft Structures*, ASTM International100 Barr Harbor Drive, PO Box C700, West Conshohocken, PA 19428-2959, 1971, pp. 230–242. doi: 10.1520/STP26680S.

[36] M. Janssen, J. Zuidema, and R. Wanhill, *Fracture Mechanics*. CRC Press, 2004. doi: 10.1201/9781482265583.

[37] R. Khan, R. Alderliesten, L. Yao, and R. Benedictus, "Crack closure and fibre bridging during delamination growth in carbon fibre/epoxy laminates under mode I fatigue loading," *Compos Part A Appl Sci Manuf*, vol. 67, pp. 201–211, Dec. 2014, doi: 10.1016/j.compositesa.2014.08.028.

[38] J. Deng, J. Zhou, T. Wu, Z. Liu, and Z. Wu, "Review and Assessment of Fatigue Delamination Damage of Laminated Composite Structures.," *Materials (Basel)*, vol. 16, no. 24, Dec. 2023, doi: 10.3390/ma16247677.

[39] A. Pirondi, G. Giuliese, F. Moroni, A. Bernasconi, and A. Jamil, "Comparative Study of Cohesive Zone and Virtual Crack Closure Techniques for Three-Dimensional Fatigue Debonding," *J Adhes*, vol. 90, no. 5–6, pp. 457–481, Jun. 2014, doi: 10.1080/00218464.2013.859616.

[40] L. Carreras *et al.*, "A benchmark test for validating 3D simulation methods for delamination growth under quasi-static and fatigue loading," *Compos Struct*, vol. 210, pp. 932–941, Feb. 2019, doi: 10.1016/J.COMPSTRUCT.2018.12.008.

[41] C. Bisagni and C. G. Dávila, "Experimental investigation of the postbuckling response and collapse of a single-stringer specimen," *Compos Struct*, vol. 108, no. 1, pp. 493–503, Feb. 2014, doi: 10.1016/J.COMPSTRUCT.2013.09.018.

[42] R. Olsson, J. C. Thesken, F. Brandt, N. Jönsson, and S. Nilsson, "Investigations of delamination criticality and the transferability of growth criteria," *Compos Struct*, vol. 36, no. 3–4, pp. 221–247, Nov. 1996, doi: 10.1016/S0263-8223(96)00079-7.

[43] D. Wilkins, J. Eisenmann, R. Camin, W. Margolis, and R. Benson, "Characterizing Delamination Growth in Graphite-Epoxy," in *Damage in Composite Materials: Basic Mechanisms, Accumulation, Tolerance, and*

Characterization, ASTM International100 Barr Harbor Drive, PO Box C700, West Conshohocken, PA 19428-2959, 1982, pp. 168–183. doi: 10.1520/STP34326S.

[44] R. Martin and G. Murri, "Characterization of Mode I and Mode II Delamination Growth and Thresholds in AS4/PEEK Composites," in *Composite Materials: Testing and Design (Ninth Volume)*, ASTM International100 Barr Harbor Drive, PO Box C700, West Conshohocken, PA 19428-2959, 1990, pp. 251–270. doi: 10.1520/STP24115S.

[45] W. Johnson, J. Masters, T. O'Brien, J. Reeder, and J. Crews, "Redesign of the Mixed-Mode Bending Delamination Test to Reduce Nonlinear Effects," *Journal of Composites Technology and Research*, vol. 14, no. 1, p. 12, 1992, doi: 10.1520/CTR10078J.

[46] A. Turon, J. Costa, P. P. Camanho, and C. G. Dávila, "Simulation of delamination in composites under high-cycle fatigue," *Compos Part A Appl Sci Manuf*, vol. 38, no. 11, pp. 2270–2282, Nov. 2007, doi: 10.1016/J.COMPOSITESA.2006.11.009.

A Appendix A

A.1. Fatigue calculations within the SSF algorithm

Since fatigue calculations are carried out by the Python master code, whichever propagation law can be implemented with also the possibility of taking into account the influence of the mode mixity and of the load ratio on the delamination. The general formulation of the propagation rate is:

$$\frac{da}{dN} = f(G, MM, R, material) \qquad \text{Eq. 59}$$

where a is the crack length, N the number of cycles and f is a function of the SERR G, of the mode mixity MM, of the load ratio R and of the material.

By assuming that the propagation rate is constant during each fatigue iteration, the number of cycles that would cause the debonding of a node in the i^{th} fatigue iteration can be calculated as:

$$N_i = \frac{l_{i-1}}{\left.\frac{da}{dN}\right|_i} \qquad \text{Eq. 60}$$

where l_{i-1} can be considered as the length of the node still attached to the master surface at the end of the $(i-1)^{th}$ fatigue iteration. Actually, a node can be either bonded or debonded but, to take into account the consumption of life of a node due to the damage cumulated in the previous loading cycles, it is assumed that a part of the "bonded length" of the node, proportional to the cumulated damage, is released. As a result, the effective bonded length at the end of the i^{th} fatigue iteration, l_i, by definition is:

$$l_i = e_l\left(1 - dmg_{cum_i}\right) \qquad \text{Eq. 61}$$

where e_l is the initial bonded length, that coincides with the mesh size, while dmg_{cum_i} is the damage cumulated at the end of the i^{th} fatigue iteration.

The damage, or consumption of life, a node is subjected to during the i^{th} fatigue iteration, dmg_i, can be calculated with the Miner-Palmgren rule:

$$dmg_i = \frac{N_{\min_i}}{N_i} \qquad \text{Eq. 62}$$

where N_i is the remaining life of the node under analysis, calculated according to Eq. 60, while N_{min_i} is the number of cycles of the i^{th} fatigue iteration, calculated as the minimum of the remaining lifes evaluated for each bonded node.

Consequently, after the first and second fatigue iterations, the effective bonded lengths of each bonded node can be calculated as:

$$\begin{aligned} l_1 &= e_l\left(1 - \frac{N_{\min_1}}{N_1}\right) = e_l(1 - dmg_1) \qquad (a) \\ l_2 &= l_1\left(1 - \frac{N_{\min_2}}{N_2}\right) = l_1(1 - dmg_2) \qquad (b) \end{aligned} \qquad \text{Eq. 63}$$

Now, if Eq. 63a is inserted into Eq. 63b, the following equation is obtained:

$$l_2 = e_l(1 - dmg_1)(1 - dmg_2) \qquad \text{Eq. 64}$$

More in general, the effective bonded length at the end of the i^{th} fatigue iteration,l_i, is:

$$l_i = e_l \prod_{k=1}^{i}(1 - dmg_k) \qquad \text{Eq. 65}$$

Therefore, if both Eq. 61 and Eq. 65 are considered, the formulation of the cumulative damage at the end of the i^{th} iteration, dmg_{cum_i}, is obtained as follows:

$$\begin{aligned} dmg_{cum,i} &= 1 - \prod_{k=1}^{i}(1 - dmg_k) \\ &= 1 - \prod_{k=1}^{i-1}(1 - dmg_k)\,(1 - dmg_i) \\ &= 1 - \left(1 - dmg_{cum_{i-1}}\right)(1 - dmg_i) \end{aligned} \qquad \text{Eq. 66}$$

Finally, by adding the definition of the damage after the i^{th} fatigue iteration (Eq. 62), the cumulative damage after the same iteration of each bonded node can be written as:

$$dmg_{cum_i} = 1 - \left(1 - dmg_{cum_{i-1}}\right)\left(1 - \frac{N_{\min_i}}{N_i}\right) \qquad \text{Eq. 67}$$

Now, two important considerations can be made:

- To initialize the calculation of the cumulative damage, the value of the initial cumulative damage, dmg_{cum_0}, is set to zero for each bonded node.
- Static iterations don't affect the value of the cumulative damage so that, more in general, it is possible to write:

$$dmg_{cum_i} = \begin{cases} 1 - \left(1 - dmg_{cum_{i-1}}\right)\left(1 - \frac{N_{min_i}}{N_i}\right) & \text{if the } i^{th} \text{ iteration is a fatigue one} \\ dmg_{cum_{i-1}} & \text{if the } i^{th} \text{ iteration is a static one} \end{cases} \quad \text{Eq. 68}$$

A.2. Adjustment of the compliance by means of a spring

In the second case study, the quasi-static simulation performed on the specimen FTG-5-05 has shown that its compliance was much lower than the one of the experimentally tested laminate (Fig. 51). As a consequence, to make them equal, a spring was added between the upper arm of the numerical specimen and the point of application of the displacement. The result is a system that could be schematized as a series of two springs (Fig. 50).

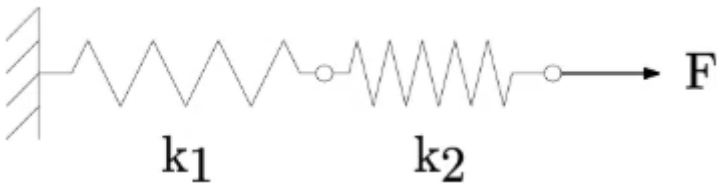

Fig. 50: Springs in series.

The relation between stiffness k and compliance C is:

$$C = \frac{1}{k} \quad \text{Eq. 69}$$

while the equivalent compliance C_{eq} of a system made of n springs in series can be calculated as:

$$C_{eq} = \sum_{i=1}^{n} C_i \quad \text{Eq. 70}$$

where C_i is the compliance of the i^{th} spring.

As can be seen in Fig. 51, by adding a spring of stiffness $k = 12\ N/mm$ the experimental and numerical load - displacement curves have the same slope.

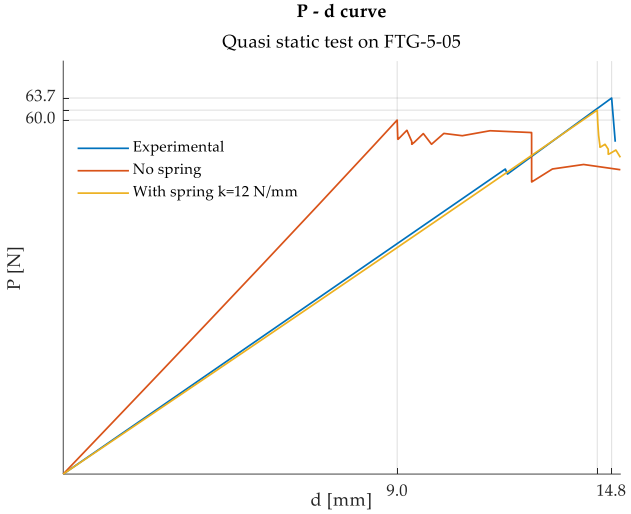

Fig. 51: Load – displacement curve adjustment.

However, an observation should be made. As the propagation advances, the compliance of the numerical specimen, $C_{spec}^{(num)}$, increases, while the one of the spring, C_{spring}, remains constant and, consequently, the equivalent compliance of the system, C_{eq}, calculated according to Eq. 70, increases too.

Under the assumption of linear behavior, a spring of compliance C under the load P exhibits the displacement δ that can be calculated as:

$$\delta = CP \qquad \text{Eq. 71}$$

In case of springs in series, each spring is subject to the same load and the displacement of the system is the sum of the displacements of the springs. Therefore, in the case under analysis, the following relationships holds:

$$d = \delta_{spec}^{(num)} + \delta_{spring} = \left(C_{spec}^{(num)} + C_{spring}\right)P = C_{eq}P \qquad \text{Eq. 72}$$

where d is the displacement of the system.

Since C_{eq} is increasing and d is constant (displacement control conditions), the load P decreases (Eq. 72). Besides, being C_{spring} constant, also δ_{spring} decreases (Eq. 71). As a consequence, δ_{spec} increases (Fig. 52):

$$\delta_{spec}^{(num)} = d - \delta_{spring} \qquad \text{Eq. 73}$$

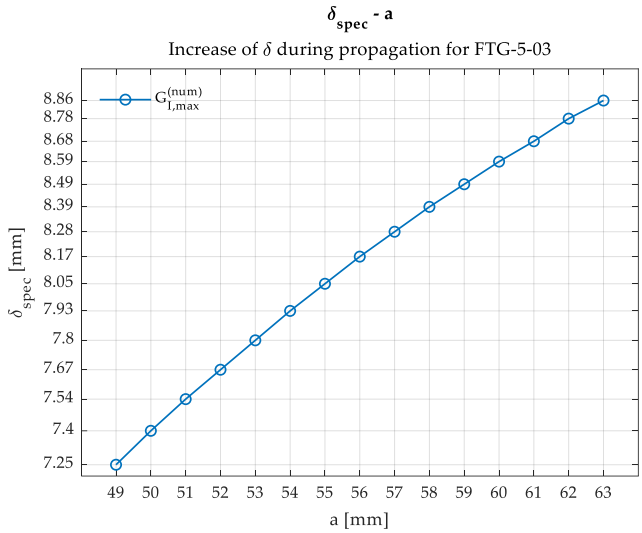

Fig. 52: Increase of the opening displacement of the specimens during delamination.

This phenomenon doesn't happen in experimental case because the loading machine, that acts as a spring in series to the specimen, is much stiffer than the laminate so that its compliance, $C_{spec}^{(\exp)}$, is negligible:

$$d = \left(C_{spec}^{(\exp)} + C_{machine}\right) P \simeq C_{spec}^{(\exp)} P = \delta_{spec}^{(exp)} \qquad \text{Eq. 74}$$

Consequently, during propagation, the laminate was effectively subject to a constant applied displacement.

This is a proof that, even if the compliance of the numerical specimen was adjusted at the beginning of the simulation, the previously highlighted alterations on the loading conditions could have affected the reliability of the results.

A.3. Compliance method to calculate the SERR distribution on the delamination front

In the second case study, to estimate the mean value of the SERR distribution on the delamination front by means of the compliance method, the formulation introduced in section 1.1.3 is used:

$$G = \frac{P^2}{2b}\frac{\partial C}{\partial a} \qquad \text{Eq. 8}$$

where P is the applied load, b the specimen width, C the compliance and a the delamination length.

It is assumed that the relationship between C and a is exponential [13]:

$$C = A_1 a^{A_2} \quad \text{Eq. 75}$$

where A1 and A2 are fitting parameters.

By applying the logarithmic function to both members of Eq. 75, it becomes:

$$\log(C) = \log(A_1) + A_2 \log(a) \quad \text{Eq. 76}$$

Through a linear fit of the logarithms of a and C, being this latter parameter calculated as the ratio between the numerical crack opening displacement $\delta_{spec}^{(num)}$ and the numerical applied load P, the parameters A_1 and A_2 are determined for each specimen. Consequently, an analytical expression for the SERR is identified:

$$G = \frac{A_1 A_2 P^2}{2b} a^{A_2 - 1} \quad \text{Eq. 77}$$

As presented in section 3.2, the SERRs calculated through Eq. 77 were compared with the ones obtained through the average of the numerical mode I maximum SERR distribution.

List of Figures

List of Tables

List of symbols

Variable	Description	Measurement unit
G	strain energy release rate	N/m
G_c	fracture toughness	N/m
G_{max}	maximum G in a loading cycle	N/m
G_{min}	minimum G in a loading cycle	N/m
ΔG	G range in a loading cycle	N/m
ΔG_{eff}	G effective range in a loading cycle	N/m
$G^{(th)}$	threshold G	N/m
$G^{(max)}$	maximum G of the distribution	N/m
K	stress intensity factor	$Pa*m^{1/2}$
R	load ratio	-
P	load	N
d	applied displacement	m
δ	opening displacement of the laminate	m
N	number of cycles	cycles
a	delamination length	m
C	compliance	m/N
k	stiffness	N/m